Raman Investigations of Phase Transition and Gas Adsorption in Metal Organic Frameworks and Tailoring Plasmons in Nano Architectures for Surface Enhanced Raman Spectroscopy

A Thesis

Submitted For the Degree of

DOCTOR OF PHILOSOPHY

in the Faculty of Science

by

GAYATRI KUMARI

CHEMISTRY AND PHYSICS OF MATERIALS UNIT
JAWAHARLAL NEHRU CENTRE FOR ADVANCED SCIENTIFIC RESEARCH
Bangalore – 560 064, India

AUGUST 2015

To my parents

DECLARATION

I hereby declare that the matter embodied in the thesis entitled " **Raman Investigations of Phase Transition and Gas Adsorption in Metal Organic Frameworks and Tailoring Plasmons in Nano Architectures for Surface Enhanced Raman Spectroscopy**" is the result of investigations carried out by me at the Chemistry and Physics of Materials Unit, Jawaharlal Nehru Centre for Advanced Scientific Research, Bangalore, India under the supervision of Prof. Chandrabhas Narayana and that it has not been submitted elsewhere for the award of any degree or diploma.

In keeping with the general practice in reporting scientific observations, due acknowledgement has been made whenever the work described is based on the findings of other investigators. Any omission that might have occurred by oversight or error of judgement is regretted.

GAYATRI KUMARI

CERTIFICATE

I hereby certify that the matter embodied in this thesis entitled " **Raman Investigations of Phase Transition and Gas Adsorption in Metal Organic Frameworks and Tailoring Plasmons in Nano Architectures for Surface Enhanced Raman Spectroscopy**" has been carried out by Ms. GAYATRI KUMARI at the Chemistry and Physics of Materials Unit, Jawaharlal Nehru Centre for Advanced Scientific Research, Bangalore, India under my supervision and that it has not been submitted elsewhere for the award of any degree or diploma.

Prof. Chandrabhas Narayana
(Research Supervisor)

Acknowledgements

I take this opportunity to express my gratitude to all the people who have motivated, inspired and supported me throughout my Ph.D.

First and foremost I extend my gratitude to my research supervisor Prof. Chandrabhas Narayana for giving me enormous freedom to pursue research in the topic of my interest. I whole heartedly thank him for being receptive to my ideas, supporting me in all my scientific endeavours and having faith in me. His enthusiasm and excitement towards science is always inspiring. I thank u Sir.

I would like to acknowledge Prof. C. N. R. Rao for his inspiring talks and the motivating stories about the great architects of science.

I am grateful to be part of this institution where I heard and met several great scientist whose enthusiasm and zeal for science have always motivated me.

I express my warm thanks to Prof. Balasubramanian and Prof. Tapas Maji for all the wonderful collaborations. I am thankful to them for teaching me important aspects of research.

I would also like to acknowledge all my collaborators, Prof. S. Rajaram, Prof. S. M. Shivaprasad, Dr. Sandeep, Dr. Prakash, Dr. Jayaram, Dr. Ritesh, Dr. N.R. Patil , Arjun, Satya, Dr. P. V. Satyam, Dr. Jay Ghatak.

I thank all the teachers in JNC, Prof. S. Balasubramanian, Prof. K. S. Narayan, Prof. N. Chandrabhas, Prof. G. U. Kulkarni, Prof. A. Sundaresan, Prof. M. Eswaramoorthy, Prof. T. K. Maji, Prof. S. M. Shivaprasad, Prof. S. K. Pati,

Prof. S. Narasimhan, Prof. U. V. Waghmare, Dr. N. S. Vidhyadhiraja, Prof. S. J. George, Prof. T. Govindaraju, Dr. R. Datta for their courseworks and guidance.

I would like to thank Integrated Ph.D. coordinators Prof. G. U. Kulkarni, Prof. S. Balasubramanian, Prof. T. K. Maji, Prof. N. Chandrabhas for their guidance.

I thank all the technical staffs, specially Usha mam and Sunil. I would also like to thank all the admin staff and support staff of JNC.

I was lucky to have wonderfull labmates in Dr. Gopal, Dr. Partha, Dr. Srinu, Dr. Soumik, Dhanya, Rajaji, Shantanu, Priyank, Sharvani, Jyothi, Dr. Diptikant, Dr. Santosh, Dr. Sorb and all the summer and project students. I cherish all the discussions and lab meetings (where I learnt more physics than I did in classes).

I would like to thank all my friends in JNC for making my stay so memorable. I thank my batchmates Chidambar, Arpan, Sharma, Rana, Varun, Sudeshna, Dileep, Pandu and all Intphd seniors and juniors. A few others need special mention, Sharmila, Nitesh, Urmi, Piyush, Ritu, Vini, Mohit, Amrit, Pavan, Ankit, Ritesh, Jayaram, Darshana, Dibyajyoti, Anindita, Chandan, Ram, Ankush, Loukya, Meha, Priyanka, Summayya, Dipti, Bhawani.

I would also like to acknowledge DST, India for the travel grant to attend ICORS2014 in Germany.

I would not have pursued Ph.D. had my teachers at Miranda House, Delhi not persuaded me. I am indebted to them. I would specially like to thank Tandon mam, Sheikh mam and Bani mam for arousing my interes in Chemistry.

All this would not have been possible without the support of my parents and family who have always encouraged me all my endeavours.

Preface

Raman scattering captures vibrational modes of molecules and materials. Minute structural changes induced by external stimuli such as temperature or pressure are reflected as shifts in the vibrational modes frequency and/or increase or decrease in intensity This thesis utilizes Raman spectroscopy technique to investigate and understand phase transitions and gas adsorption in metal organic frameworks which forms the basis of first part of the thesis. Second part of the thesis deals with surface enhanced Raman spectroscopy (SERS) and synthesis of metal nano architectures for SERS.

Chapter 1 provides thorough introduction to Raman scattering technique and surface enhanced Raman spectroscopy followed by a brief introduction on plasmonics and metal organic frameworks. Effect of thermodynamical parameters such as temperature and pressure on materials is also covered briefly in the introduction. The experimental set up including the working of custom-built Raman spectrometer used for all the Raman studies performed in the thesis is detailed in Chapter 2. Details of Linkam stage employed for temperature dependent studies and membrane type diamond anvil cell for pressure studies is also provided in this chapter.

The work chapters are divided into two parts. Part A comprises of Raman investigations on metal organic frameworks and consists of three chapters, Chapter 3, Chapter 4 and Chapter 5. Chapter 3 presents temperature dependent gas (nitrogen, methane and carbon dioxide) adsorption studies on zeolitic imidazolate

framework ZIF-8. In this chapter, we have shown that gate opening due to swinging of methylimidazole ring at low temperatures results in increased adsorption of guest molecules. Raman signature of the guest molecules further confirms encapsulation of gases in the pores of ZIF-8. In Chapter 4, we have investigated unusually high CO_2 adsorption at room temperature in comparison to that at low temperature in fluoro-functionalised MOF $[Zn(SiF_6)(pyz)_2{\cdot}2MeOH]_n$ by Raman spectroscopy. Chapter 5 gives a comprehensive Raman study of temperature, pressure and guest induced phase transition in interpenetrated MOF-508. In this chapter, we have discussed how conformational change in bipyridine ligand induces dynamics in the framework. All the three chapters also report the band assignments of MOFs studied.

Part B is based on surface enhanced Raman spectroscopy technique and consists of 2 chapters, Chapter 6 and Chapter 7. Chapter 6 deals with investigations on the distance dependence of SERS. It is known that SERS intensity decays with distance, but is the distance dependence also a function of nanoparticle size? We found that sphere of influence of SERS is dependent on the size of metal nanoparticle and increases as its size is increased. This study was performed using thin silica coating on silver nanoparticles of different sizes. Chapter 7 deals with the synthesis of silver-silica-gold sandwich nanoparticles for SERS. Signal amplification in sandwich nanoparticles occur due to mixing of light waves from multiple reflections from the silver core and gold islands resulting into enhanced SERS. This conclusion was arrived at based on comparison of SERS intensity of thiophenol on silver-silica-gold sandwich nanoparticles and silica-gold island shell nanoparticles without the silver core.

The last section presents an overview of the thesis and future prospects of the present work.

Contents

Chapter 1

Introduction

Light is an electromagnetic wave possessing dual nature of particle and wave. The duality of light was also advocated by the two ancient Indian schools, the *Samkhya* and the *Vaisheshika*. While the former conjectured light to be continous (wave like), the later surmised that light rays are jet of high velocity particles (particle nature).

The study of nature and properties of light and light matter interactions is called **optics**, derived from Greek word *optikos* meaning vision or sight. One of the first optical elements, *Nimrud lens*, can be dated back to 700 BC indicating that the curiosity over light prevailed then as well. Most of the development in the branch of optics happened in the later half of second millennium through the pioneering works of eminent philosophers like Kepler, Descartes, Newton, Huygen, Planck, Einstein, de Broglie, Maxwell and others whose discoveries eventually lead to the development of electromagnetic theory of light and quantum optics.

1.1 Raman scattering

Light interacts with matter in many ways. It gets reflected (through which we perceive the colour, size and texture of the object), absorbed, transmitted and

scattered. Out of a million photons incident on an object, a thousand are elastically scattered which is known as Rayleigh scattering after its discoverer Lord Rayleigh, while one in a million is inelastically scattered which is called as Raman scattering. Although, Raman scattering was theoretically predicted by Austrian physicist Adolf Smekal in 1922, it was not realised until 1928 when Sir C. V. Raman and K. S. Krishnan (and Grigory Landsberg and Leonid Mandelstam independently) discovered it and called it as "*A new type of secondary radiation* [1]." The first experiments were performed using Sun as the light source, telescope objective and lens to converge the ligt and eye as detector. Later mercury arc was used as the light source and spectrophotometric detection was possible due to the development of Czerny-Turner monochromator in 1930 but it was not until the discovery of laser in 1960 and CCD detector in 1969 that Raman spectroscopy saw its growth.

1.1.1 Classical theory

When an electromagnetic wave falls on a molecule, its electric field component brings about charge separation in the molecule giving rise to a dipole moment. Let **E** be the incident electric field given, then the induced dipole moment **P** can be given by the relation,

$$P = \alpha \cdot E, \tag{1.1}$$

where α is a second rank polarizability tensor of the molecule, and P and E are three dimensional vectors. The polarizability tensor is generally a function of nuclear coordinates and vibrational frequencies of molecule and can be represented as

$$\begin{bmatrix} \alpha_{xx} & \alpha_{xy} & \alpha_{xz} \\ \alpha_{yx} & \alpha_{yy} & \alpha_{yz} \\ \alpha_{zx} & \alpha_{zy} & \alpha_{zz} \end{bmatrix}$$

Let the molecule be under the influence of an oscillating electric field. If the frequency of oscillation is ν_0, the electric field is given as

$$E = E_0 \cos 2\pi\nu_0 t \tag{1.2}$$

The resultant induced dipole will vary with time as

$$P = \alpha \cdot E = \alpha E_0 \cos 2\pi\nu_0 t \tag{1.3}$$

and acts as a secondary source of electromagnetic radiation of frequency same as that of incident light. This scattering represents the elastic scattering and is known as Rayleigh scattering.

A molecule of N atoms have 3N degrees of freedom comprised of the translational, rotational and vibrational, where the latter two can alter the polarizability of the molecule. Let q_v be the normal coordinate of vibration whose coordinate as a function of time is given as

$$q_v = q_v^0 \cos 2\pi\nu_v t \tag{1.4}$$

where ν_v gives the frequency of q_v^{th} vibration. The polarizability in terms of q_v can be expressed as

$$\alpha = \alpha_0 + \left(\frac{\partial\alpha}{\partial q_v}\right)_0 q_v + \cdots \tag{1.5}$$

where α_0 is the polarizability at the equilibrium position. Generally, the terms involving higher powers of q are ignored. This approximation is known as electrical harmonic approximation which assumes that molecular vibrations involve small displacements and hence, the polarizability proportional to first power of q_v holds valid [2].

Substituting q_v from equation 1.4 in equation 1.5, we get

$$P = \alpha_0 E_0 \cos 2\pi\nu_0 t + \left(\frac{1}{2}\right) E_0 q_v^0 \left(\frac{\partial\alpha}{\partial q_v}\right)_0 [\cos 2\pi(\nu_0 + \nu_v)t + \cos 2\pi(\nu_0 - \nu_v)t] \quad (1.6)$$

The first term of equation 1.6 describes the Raleigh scattering, frequency of which is equal to ν_0. The second and the third term describes the inelastic scattering, known as Raman scattering wherein the frequency of oscillating dipole is either more $(\nu_0 + \nu_v)$ (anti-Stokes line) or less $(\nu_0 - \nu_v)$ (Stokes line) than the incident light frequency. From equation 1.6, it can be seen that a vibration will be Raman active only if the change in polarizability is non-zero during the vibration, *i.e.* $\left(\frac{\partial\alpha}{\partial q_v}\right)_0 \neq 0$.

Classical theory predicts the frequency dependence of vibrational Raman scattering and selection rules quite accurately. However, it cannot precisely give the characteristic vibrational transitions associated with molecular vibrations, the difference in the intensity of Stokes Raman and anti-Stokes Raman observed, the resonance Raman effect and dependence of α' on the incident radiation frequency and polarization. In order to explain all the features of Raman spectrum, quantum mechanics need to be invoked.

1.1.2 Quantum theory

In this approach, the molecule is treated quantum mechanically while the electromagnetic field is treated classically to avoid meticulous calculations. The quantized energy levels of molecules are obtained as solutions to the time-independent Schrödinger equation. During Raman scattering, two transitions happen instantaneously, *i.e.* excitation of an electron from state $|i\rangle$ to $|r\rangle$ and annihilation of an electron from state $|r\rangle$ to $|f\rangle$ accompanied by release of a photon of same energy (Rayleigh scattering), or greater energy(anti-Stokes) or lesser energy (Stokes) (Figure 1.1). Here, $|r\rangle$ is an intermediate state often referred to as virtual state as it

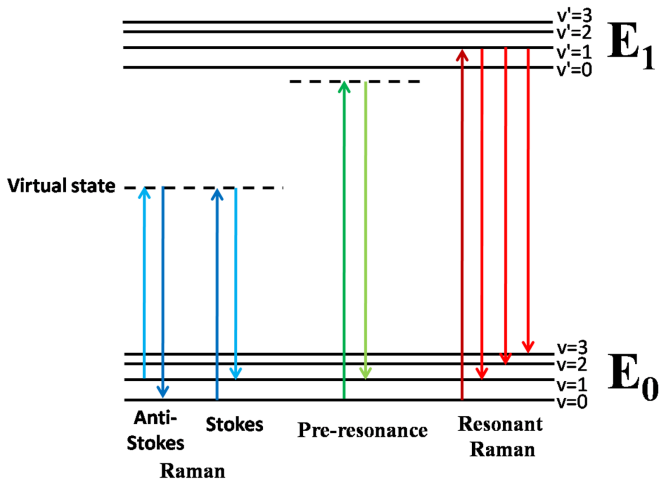

Figure 1.1: Energy level diagram showing anti-Stokes and Stokes Raman scattering, pre-resonance Raman scattering and resonance Raman scattering.

is not a solution to the Schrödinger equations. Quantum mechanically, the phenomenon of scattering is explained through transition probabilities from an initial state $|i\rangle$ to a final state $|f\rangle$ under a perturbation, namely, electromagnetic radiation in this scenario. For a given transition, an element of the Raman polarisability can be shown as [3]:

$$\alpha_{kl} = \frac{1}{\hbar} \sum_{r \neq i,f} \left\{ \frac{\langle f|p_k|r\rangle\langle r|p_l|i\rangle}{\omega_r - \omega_i - \omega_L - i\Gamma_r} + \frac{\langle f|p_l|r\rangle\langle r|p_k|i\rangle}{\omega_r - \omega_f + \omega_L + i\Gamma_r} \right\} \tag{1.7}$$

where the summation is over all possible states $|r\rangle$ having energy $\hbar\omega_r$ and width $2\hbar\Gamma_r$ (except the initial and final state), p_k and p_l are dipole moment operators. It must be noted that the states $|i\rangle$, $|f\rangle$ and $|r\rangle$ are vibronic (mixed electronic/vibrational) states of the molecule, ω_L is the angular frequency of the incident laser. It follows from equation 1.7, that for any vibrational transition $|i\rangle$ to $|f\rangle$ to be Raman active, atleast one component of transition polarisability tensor must be non-zero, thus defining the selection rule for Raman scattering. It must be mentioned here that the intensity of any transition is nowhere considered in defining selection rule. So it is possible that an allowed transition is not observed experimentally due to its

feeble intensity.

Raman modes are characterized by (a) the frequency which yields the peak position, (b) depolarization ratio (ratio of intensity in the perpendicular and parallel directions) which tells about the symmetry of molecule and (c) scattering cross section which qualitatively characterizes the intensity. Here, the scattering cross section for a normal mode m for excitation frequency ω_L is given as [3]

$$\frac{d\sigma_m}{d\Omega} = \frac{\hbar\omega_R^4}{1440\pi^2 \left(\epsilon_0\right)^2 c^4 \omega_k} \left(1 + n_k^B(T)\right) L_M R_k \tag{1.8}$$

where $\omega_R = \omega_0 - \omega_k$, L_M is local field correction and $n_k^B(T)$ is Bose factor. R_k is Raman activity given by

$$R_k = 45\bar{\alpha}_k'^2 + 7\bar{\gamma}_k'^2 \tag{1.9}$$

where $\bar{\alpha}_k'$ and $\bar{\gamma}_k'$ are the isotropic and anisotropic invariants of Raman tensor.

The overall intensity of the scattered light (4π solid angle) averaged over all the orientations of the molecule is [4]

$$I_{if} = \frac{2^7\pi^5}{9c^4} I_0 \left(\nu_0 + \nu_{if}\right)^4 \sum_{k,l} \left|\left(\alpha_{kl}\right)_{if}\right|^2 \tag{1.10}$$

where I_0 and ν_0 are the intensity and frequency of the incident light, c is the velocity of light and the summation is over k=x, y, z and l=x, y, z belonging to the molecule normal coordinate. It is evident from equation 1.10 that the intensity of scattered light is proportional to the frequency of incident light. As the incident laser frequency approaches electronic transition frequency, Raman signal enhancement by a factor of 5 to 10× occurs. This is called pre-resonance Raman. Pre-resonance Raman is useful for systems like fluorescent molecules where higher Raman signal intensity could be achieved without interference from fluorescent background. The phenomenon of resonance Raman scattering occurs when ω_L is exactly tuned to

match the real electronic transition and as a consequence, the denominator of first term in polarizability tensor (equation 1.7) diminishes. Under this condition, first term increases enormously and the intensities of Raman bands are enhanced by three to five orders of magnitude [5]. In this scenario, Γ_r (which is proportional to the lifetime of excited state) keeps the first term in polarizability tensor intact, which would otherwise be infinite under resonance Raman condition.

For an assembly of N molecules, the intensity of scattered radiation also depends on the occupation of vibronic state m. The probability of occupation of vibrational levels is given by the Bose-Einstein statistics. Even though, most molecule will occupy the lowest vibrational level at a given temperature, there will be few molecules in the higher vibrational states also. The occupancy of higher levels increases as temperature is increased and can be quantified by the ratio of Stokes and anti-Stokes intensity,

$$\frac{I_{Stokes}}{I_{anti-Stokes}} = \frac{\left(\tilde{\nu}_0 - \tilde{\nu}_m\right)^4}{\left(\tilde{\nu}_0 + \tilde{\nu}_m\right)^4} exp\left\{hc_0\tilde{\nu}_m/kT\right\} \tag{1.11}$$

where ν_m is vibrational wavenumber.

1.1.3 Temperature and pressure effects

Thermodynamical parameters like temperature and pressure have profound effects on physical properties of materials. Reducing temperature results in more ordered form, stiffened bonds and lower lattice volumes. At high temperatures, owing to increased thermal vibrations and phonon interactions, the anharmonic component of bonding force becomes more dominant. This reduces the force constant and results into thermal expansion. Temperature dependence of Raman spectra are observed as broadened peak width, reduced peak intensity and softened Raman modes. Further, increasing temperature populates the higher vibrational states and leads to enhanced intensity of anti-stokes Raman scattering or appearance of hot bands.

Pressure is cleaner and stronger source of perturbation as it only results in volume change. Increasing pressure forces the lattice to a more compact form resulting into hardening of modes and increase in band widths. Effect of pressure in Raman can be observed as 1) frequency shift, 2) change in line shape due to change in life time of the vibron. In addition, the symmetry of the system could itself change on applying the pressure thus altering the Raman spectrum. High pressure can be generated by exerting force on a smaller area. This is the principle behind diamond anvil cell (DAC) employed for pressurizing materials and one can achieve pressures up to megabars (100 GPa) regime using DACs.

1.2 Surface enhanced Raman scattering

Despite being characteristic and specific of a molecule, the application of Raman spectroscopy was limited owing to its extremely small scattering cross section (10^{-30} cm^2). The sensitivity was also low due to which it could not be used for characterization of very low concentrations of molecules. This limitation was overcome in 1974 when the first observation of enhanced Raman signal of monolayer of pyridine adsorbed on the surface of roughened silver electrode was observed [6]. This enhancement was later termed as surface enhanced Raman spectroscopy.
The amplification of Raman signal intensity of a molecule present in an ambience of high electric field density existing on the surface of metal nanostructures is known as surface enhanced Raman scattering (SERS). In 1974, Fleischmann *et al.* observed enhanced Raman signal of pyridine molecule adsorbed on silver electrode and attributed it to increased surface area and hence increased number of adsorbed molecules [6]. This was later challenged by van Duyne and Jeanmaire; and Albrecht and Creighton in 1977 who independently recognized that the increased intensity could not be only due to large surface area [7, 8]. Since then, many mechanisms were proposed to explain the enormous increase in Raman signal intensity and can

be categorized into two classes: a) electromagnetic enhancement and b) chemical enhancement. In order to understand electromagnetic enhancement mechanism, a brief introduction on plasmonics and surface plasmon resonance is necessary.

1.2.1 Optical properties of metals and surface plasmons

Metals are an interesting class of materials exhibiting a wide variety of optical properties. Noble metals like silver and gold stand out from other metals owing to their frequency dependent dielectric response. Experimentally, the optical functions of bulk samples or metallic films can be determined by reflectance or transmittance measurements. Figure 1.2 shows the real and imaginary part of complex dielectric constant as a function of photon energy [9]. This experimental dielectric response deviates from Drude free electron model at higher energy and is dominated by contribution from interband transitions. From Figure 1.2, it can be seen that the real part of dielectric constant, ϵ_1 of Ag and Au is negative and large in magnitude making them the best plasmonic materials known so far in the visible region.

Surface plasmons are collective longitudinal oscillations of free conduction electrons near metal dielectric interface strongly coupled to electromagnetic wave. Surface plasmons can be excited by electromagnetic field which induces charge separation at the nanoparticle surface due to the displacement of negative charges or electrons and holes. This generates a linear restoring force which determines the finite eigen frequency of the system, which is the plasmon resonance frequency. One can calculate the resulting polarization of the sphere due to the external field. The static polarizability of the sphere is given as [10]

$$\alpha = 4\pi\epsilon_0 R^3 \frac{\epsilon - \epsilon_m}{\epsilon + 2\epsilon_m} \tag{1.12}$$

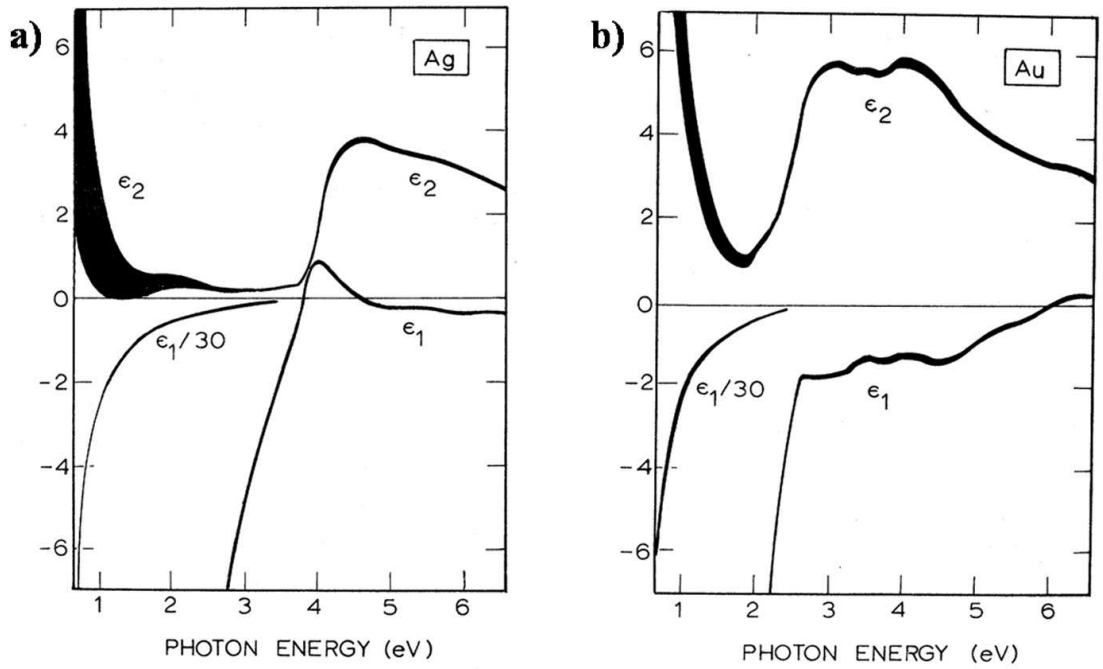

Figure 1.2: Real part ϵ_1 and imaginary part ϵ_2 of dielectric constant of a) silver and b) gold as a function of photon energy (adapted from reference [10]).

where $\epsilon = \epsilon_1 + i\epsilon_2$ is the frequency dependent complex dielectric constant of the metal and ϵ_m is the dielectric constant of the surrounding medium. For $\epsilon_2 << 1$, the resonance frequency can be derived from the relation

$$\epsilon_1 = -2\epsilon_m \tag{1.13}$$

Further, for $\epsilon_m = 1$ (*i.e.*, when surrounding medium is air or vacuum), the resonance frequency is [10]

$$\omega_1 = \sqrt{\frac{e^2}{m_e 4\pi\epsilon_0 r_S^3}} \tag{1.14}$$

where N is the total number of conduction electrons, e is the charge of an electron, m_e is mass of free electron, ϵ_0 is vacuum permittivity and r_S is the Wigner Seitz radius. It must be noted here that these plasmon oscillation exists due to excitation from electromagnetic field and will decay (if not sustained by external sources of energy) because of various loss mechanisms like collisions *etc.*

1.2.2 Electromagnetic enhancement

Electromagnetic enhancements occur due to the interaction of incident laser field and Raman scattered field with the localised surface plasmon resonances of the metallic surface. Molecule residing in the vicinity of the metal nanoparticles experiences enormous local field when the localized surface plasmon resonances are excited. The enhanced local field can be calculated within electrostatic approximation for spherical particles much smaller than the wavelength of light as the electric field is constant and uniform around the metal sphere [11, 12]. For molecule placed at distance d from a nanoparticle of radius a and dielectric function $\epsilon(\omega)$ surrounded by a non-absorbing infinite medium of dielectric constant ϵ_M, the local field will be enhanced by a factor

$$\frac{E_{Loc}(\nu)}{E_{Inc}} = \frac{\epsilon(\omega) - \epsilon_M}{\epsilon(\omega) + 2\epsilon_M} \left(\frac{a}{a+d}\right)^3 \tag{1.15}$$

where, E_{Inc} is the incident field, E_{Loc} is the local field constituting of the incident field and dipole field due to the metal sphere. The enhancement will be highest at the plasmon resonance condition when $\mathrm{Re}\epsilon(\omega) = -2\epsilon_M$ and $\mathrm{Im}(\epsilon)$ is small. This condition is satisfied by the noble metals (copper, silver and gold) and alkali metals in the visible region which makes them suitable candidate for SERS substrate. The energy radiated by the dipole in free space will be enhanced by a factor of

$$M_{Loc}(\nu) = \frac{|E_{Loc}(\nu)|^2}{|E_{Inc}|^2} \tag{1.16}$$

and is called the *local field intensity enhancement factor*. Since the molecules reside in proximity to metal nanoparticle, not only the incident field but the Raman scattered field E_{Scat} is also amplified. The net electromagnetic enhancement can be

expressed as

$$G_{em}(\nu) \approx \frac{|E_{Loc}(\nu)|^2}{|E_{Inc}|^2} \frac{|E_{Scat}(\nu)|^2}{|E_{Inc}|^2} \tag{1.17}$$

If the Stokes shift is small, both the incident field and the dipole field occur at the same wavelength and the intensity scales as $|E|^4$. This is generally referred to as E^4 approximation. It is known that the dipole field decays as d^{-3}, so from the E^4 approximation, the enhancement would decay as d^{-12}, which describes the distance dependence of SERS. A monolayer coverage around the sphere leads to d^2 increase in molecules and thus a net d^{-10} dependence of electromagnetic enhancement is observed.

1.2.3 Chemical enhancement

Chemical enhancement arises from the modification of electronic structure or polarizability of analyte due to formation of adsorbate-metal complex [13]. The modified polarizability can be more resonant with the excitation source than the pristine molecular polarizability resulting into increased Raman intensity. This enhancement may result from either physisorption, chemisorption, photon driven charge transfer from metal to molecule or vice versa (Figure 1.3). Since the symmetry point group of adsorbed molecule could be different from the parent molecule, the selection rule will change and forbidden mode in Raman can be allowed in SERS. Further, resonance Raman effect is also assumed to contribute to chemical enhancement mechanism.

In addition to the two enhancement mechanism discussed above, there are many other factors that influence SERS enhancement such as excitation wavelength, polarization and angle of incidence; SERS substrate and its orientation with respect to the incident beam; concentration and orientation of analyte on SERS substrate. It is not an easy task to account for all these parameters but SERS enhancement factor provides a good estimate of them.

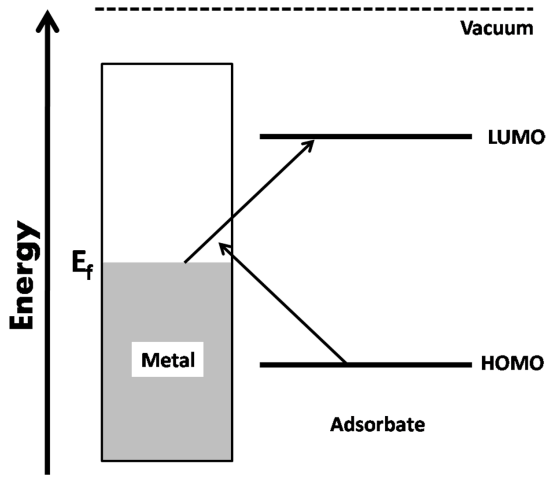

Figure 1.3: Schematic representation of band energy of the metal nanostructure and the HOMO-LUMO gap of adsorbate during a charge transfer mechanism. (Redrawn from reference [14])

1.2.4 Enhancement factor

Determination of SERS enhancement factor accurately is vital in assessing the capability of SERS substrate and its usability in various applications. Since, the distribtution of analyte molecules on SERS substrate is not uniform and regions of large enhancements or "hot spots" are highly localized, there is nothing as unique enhancement factor for a substrate. So it becomes necessary to define average enhancement factor of a substrate. There are two ways to calculate enhancement factor: a) Analytical Enhancement Factor (AEF) and b) SERS substrate enhancement factor (SSEF).

(a) **Analytical enhancement factor**

Let c_{RS} and I_{RS} be the concentration of analyte and signal intensity in Raman experiment, and c_{SERS} and I_{SERS} are the concentration and signal intensity in SERS

experiment. Then, analytical enhancement factor under identical experimental conditions (laser power, wavelength, accumulation time, *etc.*) is defined as [3]

$$AEF = \frac{I_{SERS}/c_{SERS}}{I_{RS}/c_{RS}} \tag{1.18}$$

AEF depends on many factors such as adsorption properties of analyte, its concentration, method of preparation of SERS sample *etc.* It gives a simple way to calculate SERS enhancement and can be very useful for practical applications.

(b) **SERS substrate enhancement factor(SSEF)**

SERS is surface phenomenon and only the adsorbed molecules (or the first few monolayers) contribute to the signal which was ignored while defining AEF. SSEF takes this into consideration and gives enhancement factor as [3]

$$SSEF = \frac{I_{SERS}/N_{Surf}}{I_{RS}/N_{Vol}} \tag{1.19}$$

where $N_{Vol} = c_{RS}V$ is the average number of molecules in the scattering volume V in Raman experiment while N_{Surf} is the average number of adsorbed molecules in the same volume in SERS experiment. Here, the surface coverage must be less than one monolayer to get more accurate results using equation 1.19 as SERS is a distant dependent phenomenon and the intensity decreases as one goes away from the surface of substrate which is what happens for molecules on second or higher monolayer.

1.3 Metal organic frameworks

Metal organic frameworks (MOF) are crystalline hybrid solids built from organic linkers coordinated to metal atoms forming a distinct framework structure

(Figure 1.4). Though, the first coordination polymer was reported in 1960, extensive work on MOFs started appearing only after 1990. Availability of a wide range of organic ligands and metal ions offers possibility of synthesizing large number of MOFs. They are mostly porous in nature but may be non-porous as well attributed to the structure of ligand and its arrangement in the framework. Pore size tunability and structural versatility makes them prospective material for adsorption or separation of gases , segregation of hydrocarbons, catalysis, magnetism and optical properties.

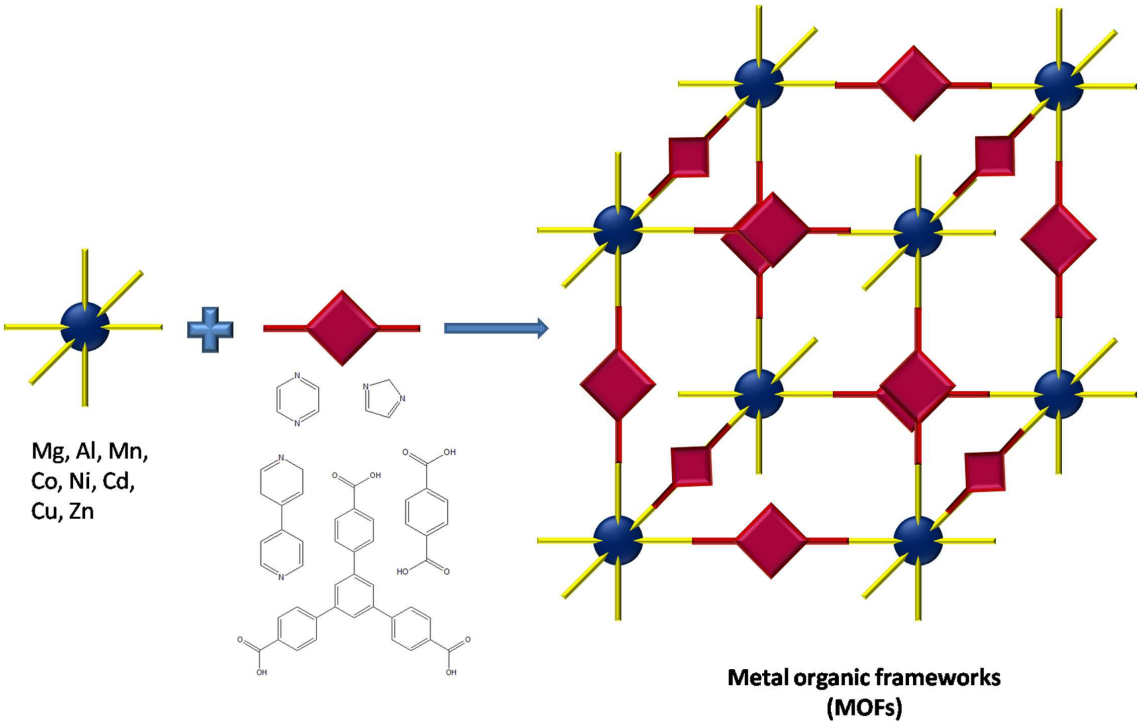

Figure 1.4: Schematic showing formation of Metal organic frameworks (MOFs) from metal atom and ligand molecule.

MOFs are categorized into three generations [15]:

(a) **First generation**: Frameworks are stable and intact as long as guest molecules are present but collapse irreversibly on removal of guest molecules.

(b) **Second generation**: Stable and robust framework showing permanent porosity even in the absence of guest molecules belongs to the second generation of MOFs.

(c) **Third generation**: Dynamic and flexible framework belongs to the third generation of MOFs. These frameworks respond to external stimuli like temperature, pressure, electric field, guests *etc.* by expanding, shrinking, tilting, and are characterized by drastic volume changes while retaining the topology.

In this thesis, I am going to focus on second and third generation of MOFs.

There are many ways by which flexibility and dynamicity arises in MOFs such as change in conformation or orientation of ligands, reversible change in coordination number of metal atoms due to removal or adsorption of solvent/guest molecules. In most studies, structural characterization is carried out by X-ray crystallography. But it is often difficult to carry out in-situ temperature, pressure or gas adsorption based X-ray diffraction measurements. In this thesis, I have used Raman spectroscopy to probe temperature or pressure induced structural transitions and gas adsorption in MOFs in systems where X-ray could not be used. The advantage of Raman measurements lies in the fact that it is local probe and can detect localized structural changes. In Chapters 3, 4 and 5 of the present thesis, I have tried to understand structural transitions and gas adsorption in MOF-508 and ZIF-8 with temperature and pressure and also answer questions pertaining to unusual gas adsorption in fluoro-functionalised MOF, $Zn(SiF_6)(pyz)_2.2MeOH$.

1.4 What is the extent of the sphere of influence in SERS?

We often say that SERS is a surface phenomenon and as we go further away from the surface the signal intensity decreases. For small molecules whose dimensions are about a few Angstroms, we observe all the allowed modes. But, what if the molecules are larger than 1 nm, such as protein or macromolecules, then do we get SERS spectrum of full protein or only the modes facing the nanoparticle are

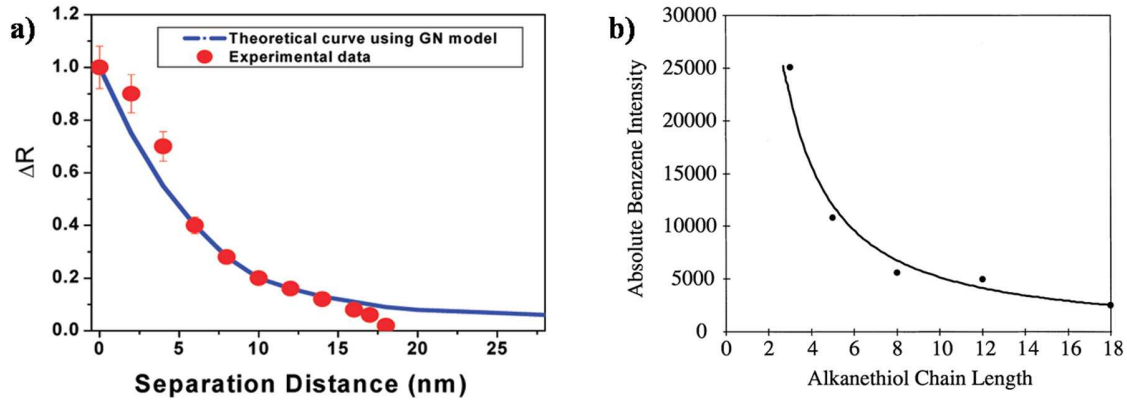

Figure 1.5: a) Change in SERS enhancement as the distance between oval gold nanoparticles and R6G is varied using dsDNA, b) Decay in SERS intensity of benzene with increasing chain length of alkanethiol attached to roughened silver foil. (Adapted from references [16, 17])

enhanced? In such instances, any structural change occuring away from the surface deep inside the protein is not captured and hence we do not get complete information. So, how do we obtain the full structural information of protein? Second, what happens when silver nanoparticles cannot be used in its native form as they are not bio-compatible and needs to be coated with thin silica shell or PEG for bio-molecular studies. One solution is to use gold nanoparticles but they yield lower enhancement factor in comparison to silver. In order to make silver universally acceptable for SERS, it must be coated with a protective layer. But what should be the optimal thickness of coating so that SERS is still observed?

In the previous section, we saw that the SERS enhancement factor decreases with distance as d^{-10}. So far, the reports on distance dependent SERS mostly concentrates on varying the distance from the nanoparticle surface by introducing spacers such as DNA, methylene, silica or alumina coating *etc.* (Figure 1.5) while keeping the particle size constant and it is found that the SERS intensity decays exponentially with distance [16, 17]. But what is the distance at which the signal becomes feeble? Is this distance same for different nanoparticle sizes or is it particle size dependent? Previously, in showing the relationship between enhancement factor and

distance, we unintentinally ignored the dependence on radius r of nanoparticle. But the radius of nanoparticle has a very important role to play and from the relation $\left(\frac{r}{r+d}\right)^{10}$, it can be said that SERS signal decay is slower for larger nanoparticles. So, what is the effective sphere of influence for nanoparticles of different sizes. This question is dealt with in Chapter 6 where silver nanoparticles of different sizes have been synthesized and the distance from the nanoparticle surface is varied incrementally by varying the silica shell thickness. Rhodamine 6G signal is used to quantify SERS intensity for each nanoparticles at different distances. Further, finite difference time domain calculations are performed on each of the nanoparticles to get the electric field distribution around them which supports the experimental result.

1.5 New nanostructure for SERS

Metal nanoparticles show interesting properties due to the presence localized surface plasmon resonance (LSPR) frequency. The electron oscillations decay either as phonons or by emitting electromagnetic wave of same energy which is used for various applications like surface plasmon resonance technique, surface enhanced Raman spectroscopy, local heating, biosensing *etc.* The SPR frequency can be tuned by changing the geometry of the nanoparticle and is sensitive to the dielectric constant of the material constituting the nanoparticle as well as of the surrounding matrix. A wide variety of nanostructures such as nanocubes, nanostars, prisms, rings, rods, hybrid nanostructures, platonic solid structures and many more are available in literature for various applications. Silver, gold and copper are the best materials to make SERS substrate attributed to their dielectric response function. Silver is the best SERS enhancer with enhancement factor values of the order of $10^8 - 10^{10}$, but it cannot be used for bio-sensing or detection due to its in-compatibility. Gold is bio-compatible but has lesser SERS enhancement effect in comparison to silver. Many other nanostructures like nanorods, nanostars, spikes show enormous Raman

intensity of the analyte due to lightning rod effect or the antenna effect which occurs due to concentration of electric fields at ends of nanorods or tip of spike. But, growth of anisotropic metal nanostructures requires shape directing agents such as CTAB (cetyltrimethylammoniumbromide) which is a surfactant, and there are two disadvantages of such nanostructures: 1) bilayer CTAB protective layer is difficult to replace by proteins or other molecules, 2) CTAB complexes with protein and may induce conformational change which is not desirable. Lian C. T. Shoute *et al.* showed increase in the SERS enhancement factor of analyte adsorbed on a planar sandwich substrate of silicon-silica-silver attributed to constructive interference of incident and refracted light from the substrate [18]. Based on his work, we have engineered new colloidal nanoarchitecture constituting of silver core, silica shell and gold islands showing higher SERS enhancement factor which forms the theme of Chapter 7.

Bibliography

[1] C. V. Raman and K. S. Krishnan, *A new type of secondary radiation*, Nature **121**, 501 (1928).

[2] D. A. Long, in *The Raman Effect* (John Wiley & Sons, Ltd, West Sussex, 2002), pp. 31–48.

[3] E. C. Le Ru and P. Etchegoin, *Principles of Surface-Enhanced Raman Spectroscopy: and related plasmonic effects* (Elsevier, Amsterdam;Boston, 2008).

[4] A. C. Albrecht, *On the theory of Raman intensities*, The Journal of Chemical Physics **34**, 1476 (1961).

[5] J. R. Ferraro, K. Nakamoto, and C. W. Brown, *Introductory raman spectroscopy* (Academic press, Boston, 2003).

[6] M. Fleischmann, P. Hendra, and A. McQuillan, *Raman spectra of pyridine adsorbed at a silver electrode*, Chemical Physics Letters **26**, 163 (1974).

[7] D. L. Jeanmaire and R. P. Van Duyne, *Surface Raman spectroelectrochemistry: Part I. Heterocyclic, aromatic, and aliphatic amines adsorbed on the anodized silver electrode*, Journal of Electroanalytical Chemistry and Interfacial Electrochemistry **84**, 1 (1977).

[8] M. G. Albrecht and J. A. Creighton, *Anomalously intense Raman spectra of pyridine at a silver electrode*, Journal of the American Chemical Society **99**, 5215 (1977).

[9] P. B. Johnson and R.-W. Christy, *Optical constants of the noble metals*, Physical Review B **6**, 4370 (1972).

[10] U. Kreibig and M. Vollmer, *Optical properties of metal clusters* (Springer-Verlag, Berlin Heidelberg, 1995).

[11] G. C. Schatz, M. A. Young, and R. P. Van Duyne, in *Surface-enhanced Raman scattering* (Springer, Berlin Heidelberg, 2006), pp. 19–46.

[12] P. G. Etchegoin and E. C. Le Ru, in *Surface Enhanced Raman Spectroscopy: Analytical, Biophysical and Life Science Applications* (Wiley-VCH Verlag GmbH & Co. KGaA, Weinheim, 2011), pp. 1–37.

[13] A. Campion, J. Ivanecky III, C. Child, and M. Foster, *On the mechanism of chemical enhancement in surface-enhanced Raman scattering*, Journal of the American Chemical Society **117**, 11807 (1995).

[14] R. Aroca, *Surface-enhanced vibrational spectroscopy* (John Wiley & Sons, West Sussex, 2006).

[15] U. Schubert and N. Hüsing, *Synthesis of inorganic materials* (John Wiley & Sons, Weinheim, 2012).

[16] A. K. Singh *et al.*, *Development of a Long-Range Surface-Enhanced Raman Spectroscopy Ruler*, Journal of the American Chemical Society **134**, 8662 (2012).

[17] B. Kennedy, S. Spaeth, M. Dickey, and K. Carron, *Determination of the distance dependence and experimental effects for modified SERS substrates based on self-assembled monolayers formed using alkanethiols*, The Journal of Physical Chemistry B **103**, 3640 (1999).

[18] L. C. Shoute *et al.*, *Optical interference effects in the design of substrates for surface-enhanced Raman spectroscopy*, Applied spectroscopy **63**, 133 (2009).

[19] P. L. Stiles, J. A. Dieringer, N. C. Shah, and R. P. Van Duyne, *Surface-Enhanced Raman Spectroscopy*, Annual Review of Analytical Chemistry **1**, 601 (2008), pMID: 20636091.

Chapter 2

Experimental Techniques

Raman scattering is a weak process and to have been detected by Sir C. V. Raman in 1928 using sunlight as source and eye as detector is miraculous. Over the years, and with the development in the science and the technology, major changes in the excitation sources used (from mercury lamps to lasers) and the detectors employed (from photographic plates to charge coupled devices) were observed. Eventually, commercial Raman set ups with triple monochromator which was highly efficient in removing stray light and had high resolving power due to the holographic grating used were made available. However, commercial Raman instruments are expensive and do not leave scope for modifications required for different kinds of experiments. In addition these spectrometers are sold as black boxes and the researcher is unable to understand and maintain such a system. This limitation is overcome by using a custom-built Raman spectrometer and is discussed in the following section.

2.1 Design of Raman spectrometer

Figure 2.1 shows the design of the custom-built micro-Raman spectrometer [1]. It involves the excitation source (633 nm He-Ne laser or 532 nm Nd-YAG laser) which passes through the plasma line filter, PF and neutral density filter, NDF. PF

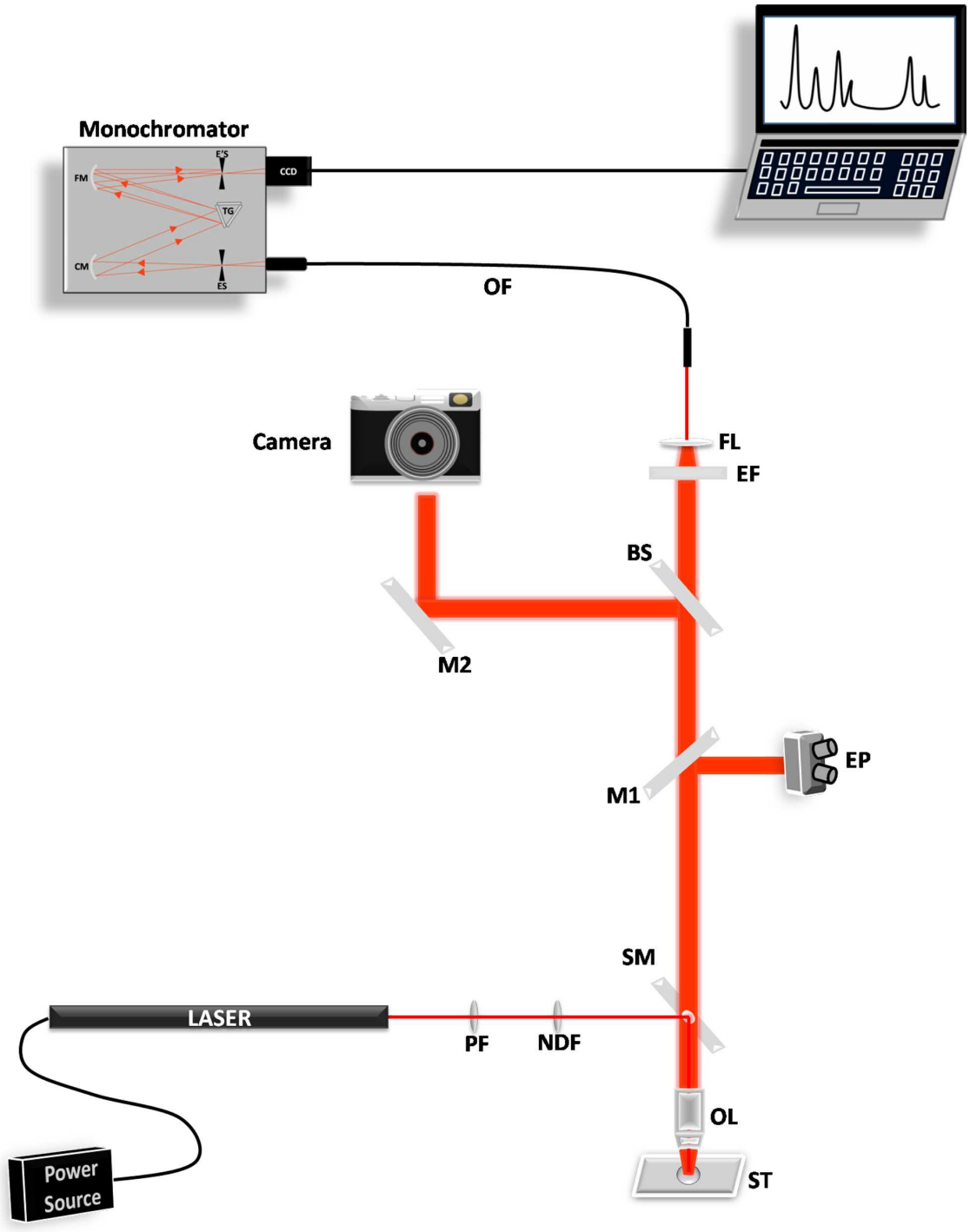

Figure 2.1: Design of custom-built micro-Raman spectrometer [1]. PF-plasma line filter; NDF-neutral density filter; OL-objective lens; ST-sample stage; SM-special mirror; M1,M2-mirrors; EP-eye piece; BS-beam splitter; EF-edge filter; FL-focussing lens; OF-optical fibre. Monochromator: ES-entrance slit; CM-collimating mirror; FM-focussing mirror; E'S-exit slit, TG-triple grating; CCD-charge coupled device detector.

filters the plasma lines generated in a gas laser while NDF reduces the power of transmitted beam which is needed while working with organic samples or biological samples in order to prevent laser induced chemical change or degradation of the sample. The laser then incidents on a special mirror at 45 degrees inside an epi-fluorescent microscope and is reflected towards the sample through the objective. For majority of the experiments, an infinity corrected 50X objective(NIKON, L Plan 50X, 0.45 NA, WD 17 mm) was used. The back-scattered light collected through the same objective is made to pass through the edge filter which blocks the Rayleigh line. This light is then focused onto the optical fiber, other end of which is f-number matched to the entrance mirror of the Czerny-Turner type monochromator (iHR320, Horiba Jobin Yvon) fitted with a charge coupled device (Andor, DU401A-BR-DD). The monochromator has an entrance slit whose width can be controlled using Labspec software which is interfaced with the spectrometer. The collimated light from the collimating mirror is then focussed onto the on-axis triple grating turret which disperses the light onto the focussing lens from where it is focussed onto the CCD. The triple grating turret supports three different groove density: holographic 1800 grooves per mm providing the highest resolution, 1200 grooves per mm and 600 grooves per mm. Peltier cooled CCD comprised of two dimensional array (1024 $\times$ 127) pixels having a pixel size of 26 $\times$ 26 microns is employed to collect the signal.

I have used the custom-built Raman spectrometer for all the Raman and surface enhanced Raman studies reported in this thesis.

2.2 Temperature dependent measurements

Temperature dependent Raman measurements were carried out in a Linkam THMS 600 heating-cooling stage equipped with temperature controller and liquid nitrogen pump (TMS94). The temperature could be tune to vary from -196 $^{\circ}C$ to

600 $^{\circ}C$ with an accuracy of 0.1 $^{\circ}C$ achievable at different ramp rate, highest being 150 $^{\circ}C$ per minute. For all the present studies, a constant ramp rate of 10 $^{\circ}C$ per minute was maintained. In order to prevent condensation of moisture during low temperature measurements, recycled hot nitrogen is blown on the viewing window surface.

The Linkam stage has two quick-fit gas ports (Figure 2.2) which serves as inlet

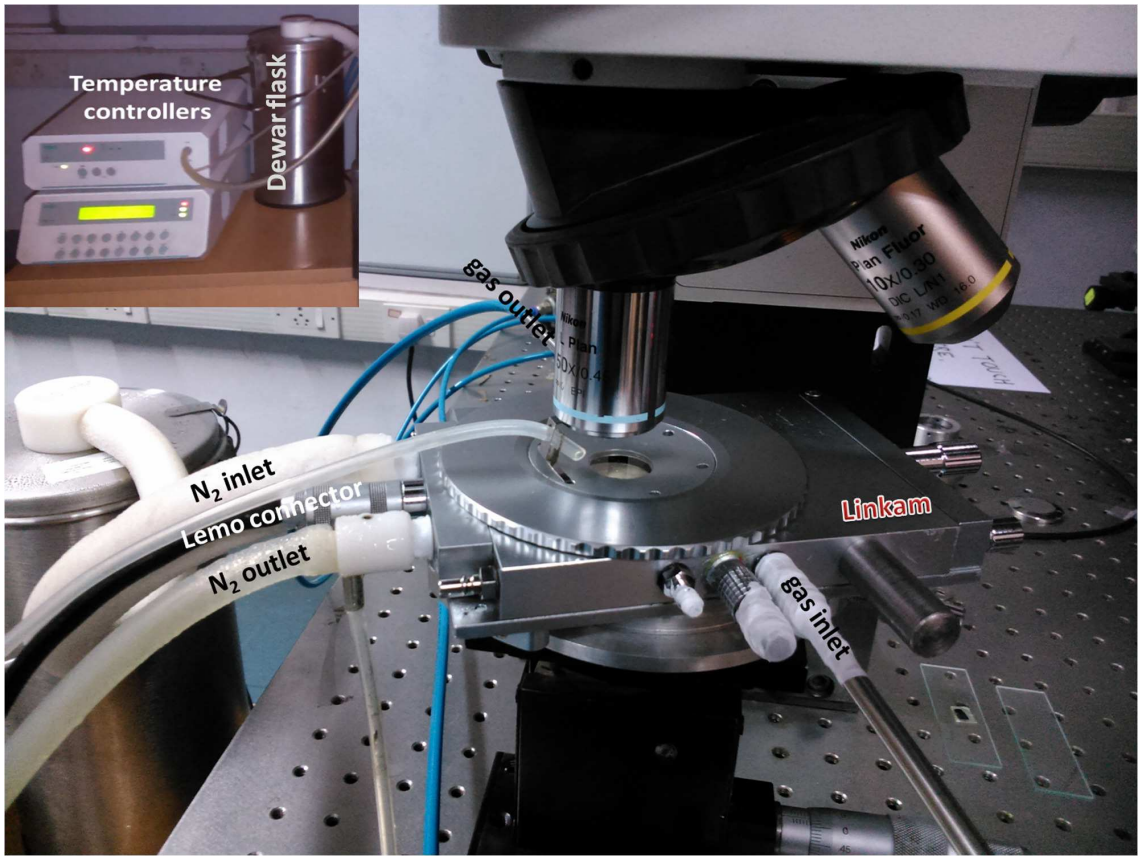

Figure 2.2: Linkam stage employed for temperature dependent and gas adsorption Raman studies of MOFs. Inset shows the temperature controllers and Dewar flask for containing liquid nitrogen.

and outlet for purging gases in order to change the atmosphere of the chamber. We have investigated adsorption of three gases namely nitrogen, methane and carbon dioxide in metal organic frameworks using Linkam stage.

2.3 High pressure studies

Force applied normal to the surface generates pressure. To accommodate the force, atoms move nearer to each other which can lead to reduction in volume, or the unit cell may tilt, contract or re-orient. This may result into new properties in the materials which could be harnessed for different applications such as that of topological insulators. Alternatively, it may also be needed to know that during deformation or when force is applied what is the change occuring at the atomic level. We have tried to understand this structural deformation by Raman spectroscopy. The pressure is applied by placing the sample in a diamond anvil cell whose details are dealt with in the following section.

2.3.1 Diamond Anvil Cell (DAC)

Diamond is the hardest material formed naturally under extreme conditions of temperature and pressure in earth's mantle. Thus, it is widely used for cutting and polishing tools in industries. Hence it is the ideal material to use for transmitting pressures on to the sample. The High pressure experiments mostly rely on diamond anvil cells for applying pressure attributed to its hardness and transparency for most of the electromagnetic radiation such as γ rays, X-rays, UV-Visible and IR range. Pressure is applied by the compressing the sample between the culets of the opposing diamonds. Pressures as high as 300 GPa (3,000,000 bars) can be achieved using DACs. Figure 2.3 shows the picture of the DAC.

2.3.2 Membrane type Diamond Anvil Cell (MDAC)

For high pressure Raman studies presented in the thesis, membrane type diamond anvil cell (MDAC) shown in Figure 2.3 was used whose main components are steel membrane, diamond stuck to upper and lower rocker, gasket, guidance dowel

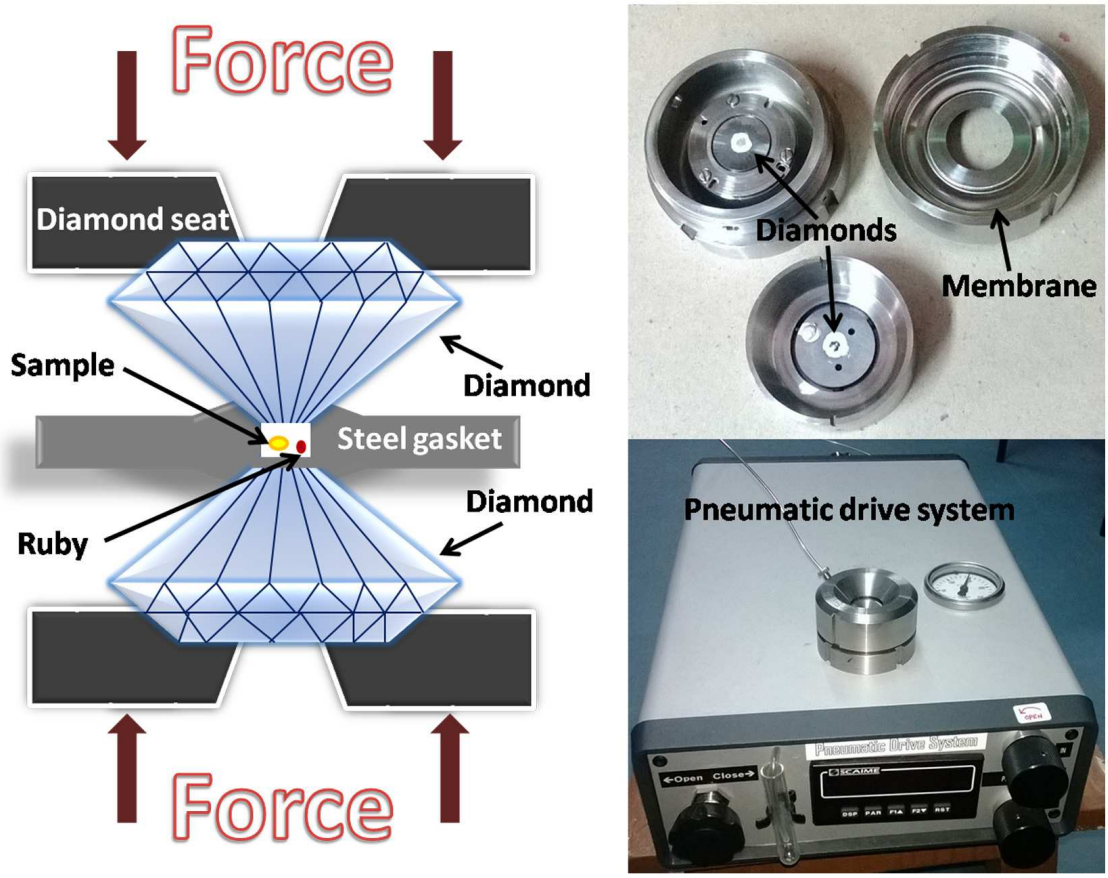

Figure 2.3: Diamond anvil cell (Left). Picture of membrane type diamond anvil cell (top right) and the pneumatic drive system (bottom right).

to hold and align the piston inside cylinder. In our MDAC cell, the guidance dowel is replaced with guide screw and notch which can lock the piston over cylinder. A pneumatic drive system (PDS) controls the pressure inside the MDAC by varying the pressure in its membrane. The pressure inside the PDS can be varied from 0-150 bars by He gas flow. When the He gas flows into the stainless steel membrane, it expands and exerts force onto the MDAC piston thus generating pressure inside the cell. This uniaxial pressure is converted into a uniform hydrostatic pressure via a pressure transmitting medium such as Argon, Helium, ethanol-methanol mixture or NaCl.

The main factors that affects the pressure in the MDAC cell are: a) type of anvil, b) hardness of cell material, c) alignment of anvil, d) gasket material and hole size, e) pressure transmitting medium and are discussed below.

Diamond

Selecting a suitable diamond is very important in fabricating a DAC. Brilliant-cut, gem quality diamonds are used as anvils. Type II diamonds are the purest form and transparent to all electromagnetic radiation, but they are expensive.Type I diamonds contain nitrogen impurities and are commonly employed in DACs. To attain high pressures in the megabar regime, diamonds with small culet size are needed. The maximum attainable pressure (P_{max}) is related to the culet diameter d by the following formula [2],

$$P_{max} = \frac{12.5}{d(mm)^2} \tag{2.1}$$

The diameter of the table (base) of diamond determines the force applied to the backing plates and hence the maximum pressure. The culet size must be much smaller than the table for generating high pressure. Further the shape of diamond anvil also decides the maximum attainable pressure.

Backing plates: Backing plates, that is the material that provides support to the diamond is another important factor which puts a limit on the maximum pressure. The applied stress on the backing plates must be lesser than its plastic deformation limit as exceeding this would result in loss of alignment and may lead to breakage of diamonds. Tungsten carbide and boron carbide are preferred material for mounting diamond. The backing plates have tapered holes whose diameter should be greater than the culet diameter but lesser than a third of the diameter of diamond table . Larger holes weaken the backing plates and hence cannot sustain high stress. Finally, the diamond is mounted on the hole such that the culet is at the centre of the tapered hole of the backing plate so that the laser beam can pass through the tapered holes into the diamond and illuminate the sample.

Diamond alignment: Alignment of the two diamond culets in the DAC is very critical for high pressure measurements. The culets must be perfectly parallel and laterally aligned both in x and y direction to prevent gasket deformation and rupture of diamonds at high pressures. The alignment is achieved by adjusting the screws on the piston wall and on top of the cylinder. When the diamonds are not aligned, an interference fringe pattern is seen which disappears after perfect alignment.

Gasket: Gasket plays two important roles: a) it serves as a holder for sample and pressure transmitting medium and b) it supports the diamond culet. An impression of diamond culet is made in the gasket using DAC which is known as indentation. Pre-indentation hardens the gasket and prevents rupturing of diamonds. A hole whose diameter is a third of that of culet size is drilled at the centre of the indentation [3]. We have used stainless steel gasket (T301) having a initial thickness of 250 μm for our experiment.

Pressure medium: The sample must be immersed in a fluid to attain hydrostatic pressure [4]. This fluid acts as pressure transmitting medium. It must noted that the medium should not dissolve or react with the sample. Typical fluids used for

high pressure measurements are inert gases like He or Ar, ethanol-methanol mixture (4:1), water, silicone oil, hydrocarbon mixture, NaCl [4, 5] *etc.* Since the sample used was unstable in water or ethanol-methanol mixture, we have used pure NaCl crystals (Sigma-Aldrich) for our experiment. On application of pressure, NaCl crystallizes into transparent solid and remains hydrostatic till 7 GPa.

Pressure measurement: Ruby ($Al_2O_3 : Cr^{3+}$) fluorescence technique is widely used to gauge pressure in high pressure work using DACs [6]. Ruby has strong R-line luminescence which is composed of two sharp lines, R1 and R2. The origin of these lines are attributed to the crystal field splitting of d-orbitals of Cr^{3+} in an octahedral geometry. R1 and R2 occur at 694.2 nm and 692.8 nm respectively. These lines show notable red shift with pressure [7] while the separation between them remains constant. R1 line shows linear dependence with pressure upto 20 GPa at ambient temperature and is generally used for pressure calibration under static high pressure [8]. Pressure is measured using the relation [9],

$$P(GPa) = \frac{1904}{B}\left[\left(1 + \frac{\Delta\lambda}{\lambda_0}\right)^B - 1\right] \tag{2.2}$$

where $\Delta\lambda = \lambda_P - \lambda_0$ is the difference in the wavelength at pressure P and ambient pressure. B=7.665 and 5 for quasi-hydrostatic and non-hydrostatic conditions respectively. Under non-hydrostatic conditions, the R1 and R2 lines broaden and overlap and there is large uncertainty in pressure measurement. Ruby crystals were loaded along with the sample for in-situ pressure measurement during Raman studies of MOF.

Bibliography

[1] G. V. P. Kumar and C. Narayana, *Adapting a fluorescence microscope to perform surface enhanced*, Current science **93**, 778 (2007).

[2] D. J. Dunstan and I. L. Spain, *Technology of diamond anvil high-pressure cells: I. Principles, design and construction*, Journal of Physics E: Scientific Instruments **22**, 913 (1989).

[3] D. J. Dunstan, *Theory of the gasket in diamond anvil high-pressure cells*, Review of Scientific Instruments **60**, 3789 (1989).

[4] Y. Shu-Jie, C. Liang-Chen, and J. Chang-Qing, *Hydrostaticity of pressure media in diamond anvil cells*, Chinese Physics Letters **26**, 096202 (2009).

[5] G. Piermarini, S. Block, and J. Barnett, *Hydrostatic limits in liquids and solids to 100 kbar*, Journal of Applied Physics **44**, 5377 (1973).

[6] J. Barnett, S. Block, and G. Piermarini, *An Optical Fluorescence System for Quantitative Pressure Measurement in the Diamond-Anvil Cell*, Review of Scientific Instruments **44**, 1 (1973).

[7] R. A. Forman, G. J. Piermarini, J. D. Barnett, and S. Block, *Pressure measurement made by the utilization of ruby sharp-line luminescence*, Science **176**, 284 (1972).

[8] K. Syassen, *Ruby under pressure*, High Pressure Research **28**, 75 (2008).

[9] H. Mao, P. Bell, J. t. Shaner, and D. Steinberg, *Specific volume measurements of Cu, Mo, Pd, and Ag and calibration of the ruby R1 fluorescence pressure gauge from 0.06 to 1 Mbar*, Journal of Applied Physics **49**, 3276 (1978).

Part I

Metal Organic Frameworks

Chapter 3

Temperature Induced Structural Transformations and Gas Adsorption in the Zeolitic Imidazolate Framework ZIF-8: A Raman Study

3.1 Introduction

Zeolitic imidazolate frameworks (ZIFs) are structurally analogous to zeolites wherein the metal atoms are connected via the nitrogen atom of imidazolate or their derivatives giving rise to a rigid framework with characteristic well-defined

Reprinted(adapted) with permission from "Temperature Induced Structural Transformations and Gas Adsorption in the Zeolitic Imidazolate Framework ZIF-8: A Raman Study" *J. Phys. Chem. A* **2013**, *117*, 11006-11012. Copyright 2013, American Chemical Society. `http://pubs.acs.org/doi/abs/10.1021/jp407792a`

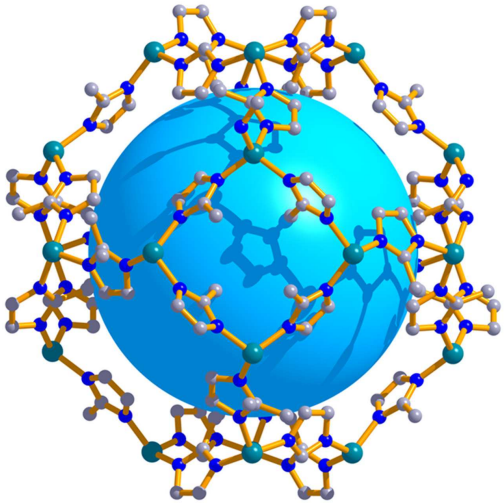

Figure 3.1: Three dimensional view of ZIF-8. H atoms have been removed for clarity. C, gray; N, royal blue; Zn, teal

pores and window sizes. Substantial gas adsorption as a result of sequential filling of the pores has been attributed to polarizability, guest induced flexibility or structural re-organisation to fit gases of various sizes and shapes. The pore size tunability can be achieved by changing the functionality on the imidazole linker as demonstrated by Banerjee *et al.* [1]. Recently, ZIFs have attracted great interest in various applications like gas separation and purification [2–6], catalysis [7, 8], sensing *etc.* [9, 10] because of their high surface area attributed to large micro pore volume, chemical inertness toward alkaline water and various organic solvents and higher stability [11]. There are numerous reports on the synthesis methods for micro and nano ZIFs [12–16]. Higher surface area of nano ZIFs as a consequence of increased pore accessibility makes them very promising materials for gas adsorption and catalysis.

ZIF-8 is constituted of Zn(II) metal ions bridged by methyl-imidazole linker (Figure 3.1). It has a sodalite structure and crystallizes in a cubic lattice with space group $I\bar{4}3m$. Owing to its high stability (it can sustain pressure up to 1.6 GPa [17]) and

flexibility, ZIF-8 is the most pursued material among all the ZIFs known so far. The narrow window size of 3.4 Åinterconnecting the cavities of size 11.4 Åmakes ZIF-8 a prospective material for gas storage, purification and separation of smaller hydrocarbons [2, 5, 18]. Although, ZIF-8 is known to adsorb smaller gas molecules such as hydrogen, nitrogen, methane, carbon dioxide [18], it is surprising to observe that it can uptake gas molecules like methane (3.8 Å) and nitrogen (3.6 Å) having kinetic diameter larger than the ZIF-8 window size [18–20]. This unusual gas adsorption behavior is speculated to be due to the swinging of the imidazolate moiety resulting in an increase of the channel size [21, 22]. In order to get a microscopic picture and thereby understand the structural changes, we have employed Raman spectroscopic tool to probe ZIF-8.

Raman spectroscopy is a powerful technique which gives the vibrational modes associated with the molecule or material. Minute changes in the structure induced by host−guest interactions or by external stimuli such as temperature or pressure can be captured and is reflected as a change in the vibrational modes frequency or intensity [23]. Recently, Raman spectroscopy has been used to provide evidence for gas adsorption in MOFs indicated by their Raman lines [23–26]. However, very few reports focus on the structural changes that occur in ZIFs during gas adsorption via Raman spectroscopic studies. Even though X-ray and NMR have been used extensively to study ZIF-8 [27], these techniques do not provide ample information about the molecular interactions in the crystal. X-ray diffraction is limited by its inability to give precise hydrogen atom positions while in-situ NMR studies on solid samples to capture the molecular dynamics is difficult. This prompted us to conduct Raman meausurements on ZIF-8. In this study, first we have shown that nano ZIF-8 (nZIF-8) shows higher adsorption of N_2, CO_2 , and CH_4 gases when compared with micro ZIF-8 (mZIF-8). Second, we have investigated temperature induced molecular

level changes in mZIF-8 through Raman spectroscopy and hence provided a plausible reason for adsorption of bigger gas molecules (N_2, CO_2, CH_4) through narrow channels.

3.2 Experimental Details

All the reagents and solvents employed were commercially available and used as supplied without further purification. Zinc nitrate tetrahydrate and 2-methyl imidazole were purchased from Sigma-Aldrich. Crystals of mZIF-8 were prepared according to a previously reported procedure [11]. A mixture of Zinc nitrate tetrahydrate (0.210 g, 0.8 mmol), 2-methyl imidazole (0.060 g, 0.7 mmol), and 18 mL N,N-dimethylformamide (DMF) was put in a 23 mL Teflon bomb. The reaction mixture was stirred for 1 h. The Teflon bomb was then subsequently placed in a steel autoclave and heated at 140 °C under autogenous pressure for 72 h and then cooled to ambient temperature. Light yellow block shaped crystals of mZIF-8 were isolated by decanting the supernatant liquid and washed thoroughly several times with DMF. (Yield 69 %). Anal. Calcd. for $C_{11}H_{23}ZnN_5O_4$: C, 35.75; H, 6.58; N, 19.74 %. Found: C, 36.09; H, 7; N, 19.49 %.

Nanoscale ZIF-8 was synthesized according to the literature report by Cravillon *et al.* [28]. Typically, 366 mg of $Zn(NO_3)_2{\cdot}6H_2O$ and 811 mg of 2-methylimidazole were put in two separate beakers containing 25 mL methanol each. Both the clear solutions were mixed and stirred until the two components were mixed properly. After 24 h, a gel like solid was recovered by centrifugation and washed with methanol three times.

The resultant mZIF-8 was characterized by different techniques. Powder X-ray diffraction (PXRD) pattern was recorded on a Bruker D8 Discover instrument using Cu−Kα radiation. The morphology of ZIF-8 were examined with a transmission electron microscope (TEM; JEOL JEM-3010 with an accelerating voltage of 300

KV). The gases (nitrogen, methane, carbon dioxide, and argon) for adsorption studies were obtained from Chemixgases, India, and were 99.99 % pure.Adsorption of N_2 (77 K), CO_2 (195 K), and CH_4 (195 K) was carried out using QUANTACHROME AUTOSORB-1C analyzer. Raman spectra were recorded using a custom built Raman spectrometer with a HeNe red laser (632.8 nm) and 1800 lines/mm grating [29]. Laser power was 8 mW at the sample. Temperature dependent Raman studies were carried out in a Linkam THMS 600 heating-cooling stage. Typical accumulation time was 30 s for all the Raman studies. For gas adsorption Raman studies, activated powder ZIF-8 was mounted on the Linkam stage, and heated to 80 °C and then cooled to room temperature (RT) after which the gases were purged. Temperature was monitored through the temperature controller attached to the Linkam stage. The gas pressure was regulated by the regulator fixed at the inlet and was mostly kept constant around 1 atm. The Raman spectra obtained were smoothened using 5 point FFT, and background was removed by baseline correction.

3.3 Results and Discussions

Micro and nano ZIF-8 synthesized were characterized with PXRD as shown in Figure 3.2 corresponding to the structure in Figure 3.1. Surface area and pore volume were determined using nitrogen adsorption-desorption isotherm at 77 K with typical type-I behaviour exhibited for micro-porous materials. The Brunauer-Emmett-Teller (BET) surface area for mZIF-8 was found to be 520 m^2/g with a pore volume of 0.31 cm^3/g, while it was found to be 1120 m^2/g with significant pore volume of 0.956 cm^3/g for nZIF-8. Optical image of mZIF-8 and TEM image of nZIF-8 is presented in Figure 3.3a and 3.3b respectively.

Figure 3.4 shows the adsorption profiles of nitrogen, carbon dioxide and methane in mZIF-8 and nZIF-8. From the adsorption profiles, it is evident that the gas uptake by nZIF-8 is higher than mZIF-8 for all the gases. The guest molecules can either

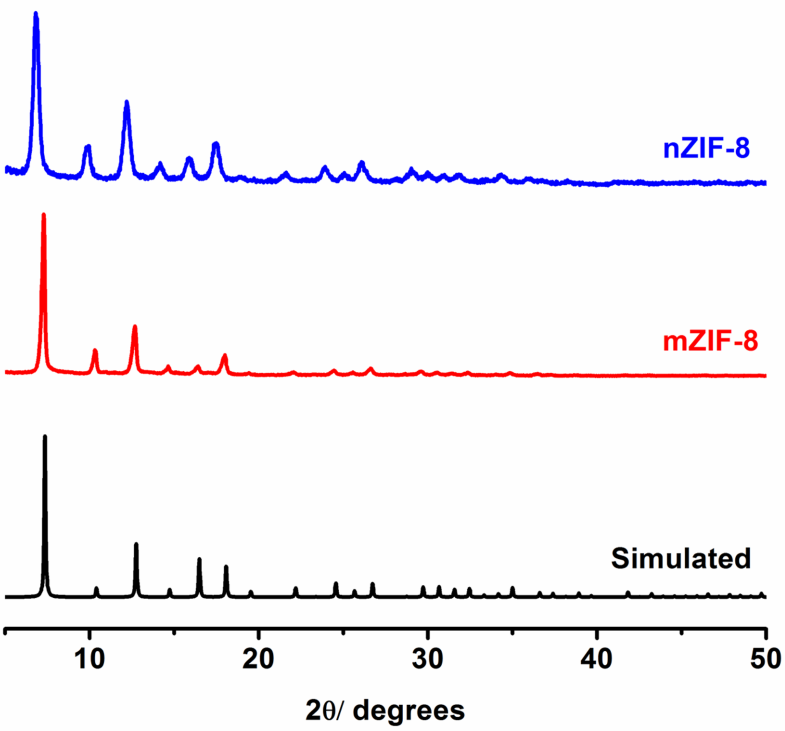

Figure 3.2: PXRD pattern of nZIF-8, mZIF-8 and simulated curve of ZIF-8.

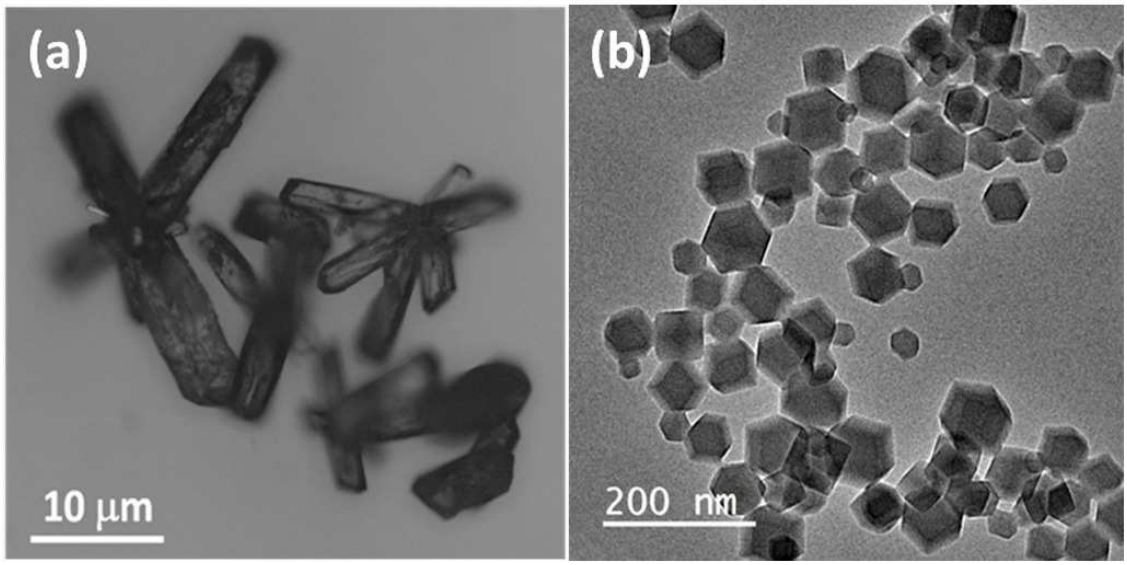

Figure 3.3: (a) Optical image of mZIF-8, (b) TEM image of nZIF-8.

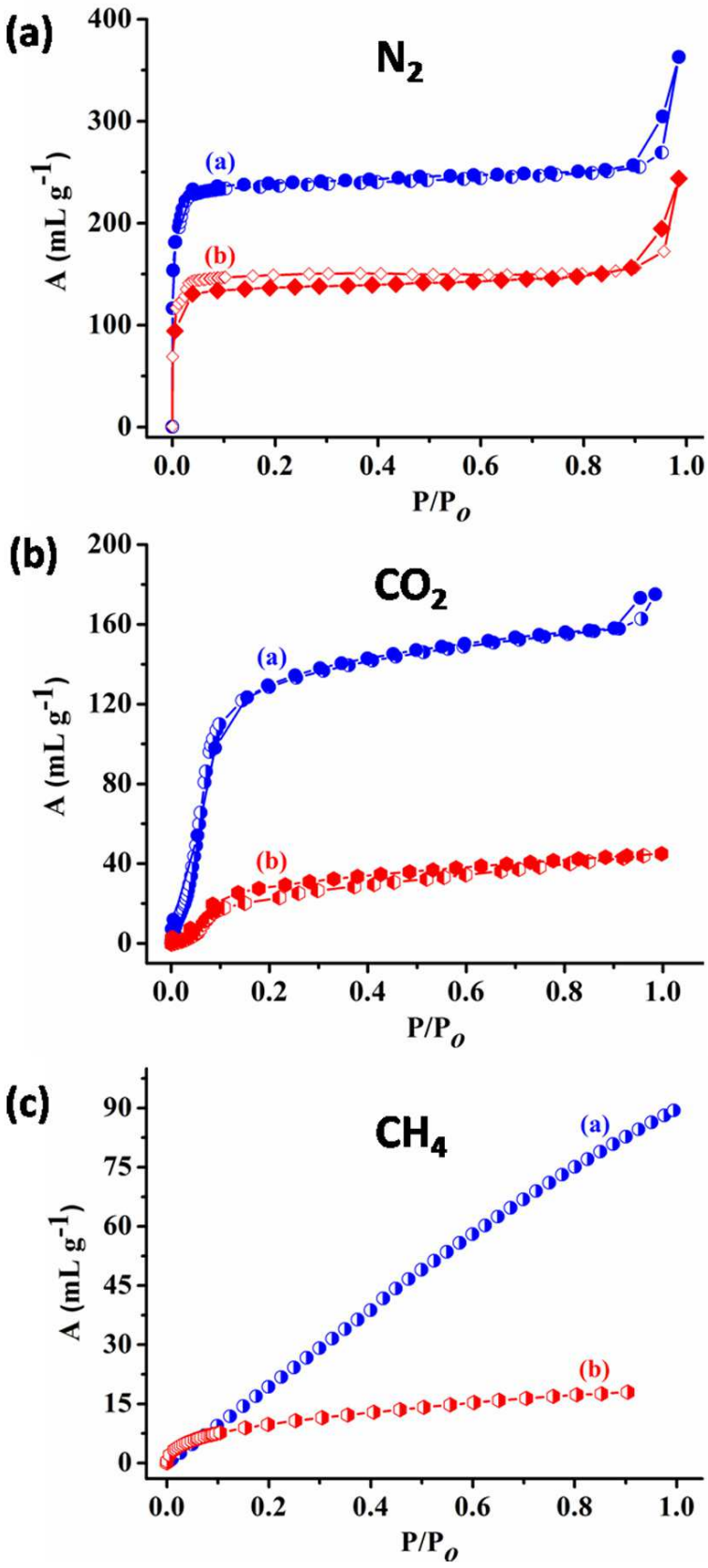

Figure 3.4: Adsorption-desorption profiles of (a) N_2 at 77 K, (b) CO_2 at 195 K, and (c) CH_4 at 195 K. The red curve represents mZIF-8, and the blue curve represents nZIF-8 in all the figures.

adsorb on the surface or in the pores of any material. The adsorption in mZIF-8 is mainly driven by diffusion into the pores. nZIF-8 has higher accessible area due to the smaller crystallite size giving rise to lower diffuion barrier and more accessible pores. Further, it is also noticed that nitrogen and carbon dioxide uptake in both mZIF-8 and nZIF-8 is more in comparison to methane. This can be attributed to: (a) development of weak dipole in the gas molecules facilitating interaction with the ZIF-8 framework and, (b) and linear geometry of N_2 and CO_2 molecules through the the cylindrical channels while blocking the tetrahedral methane molecules resulting in lesser uptake. In the following section, we will show that as the temperature reduces, the uptake increases making it possible to capture signals from encaged gas molecules.

3.3.1 Temperature dependent Raman study of ZIF-8 in nitrogen atmosphere

Room temperature Raman spectrum of mZIF-8 shown in Figure 3.5 is dominated by intense bands of methyl group and imidazole ring vibrations. Band assignments were carried out by referring to earlier reports on Raman bands of imidazole and methyl moiety and is summarized in the Table 3.1 [30–32]. Strong bands corresponding to Zn−N stretching, imidazole ring puckering, C5−N stretching and methyl bending vibrations were observed at 168 cm^{-1}, 686 cm^{-1}, 1146 cm^{-1}, and 1458 cm^{-1} respectively. Previous X-ray crystallography study assert that N_2 inside mZIF-8 induces change in unit cell parameters indicating a phase different than the RT phase [20]. To get an insight into the phase change resulting from change in temperature, we have recorded the temperature dependent Raman spectra of mZIF-8 in an atmosphere of nitrogen. As the temperature is reduced from RT (293 K) to 83 K, most of the Raman modes harden suggesting stiffened bonds and increased bond strength which could result from lattice compression at low temperatures. There is

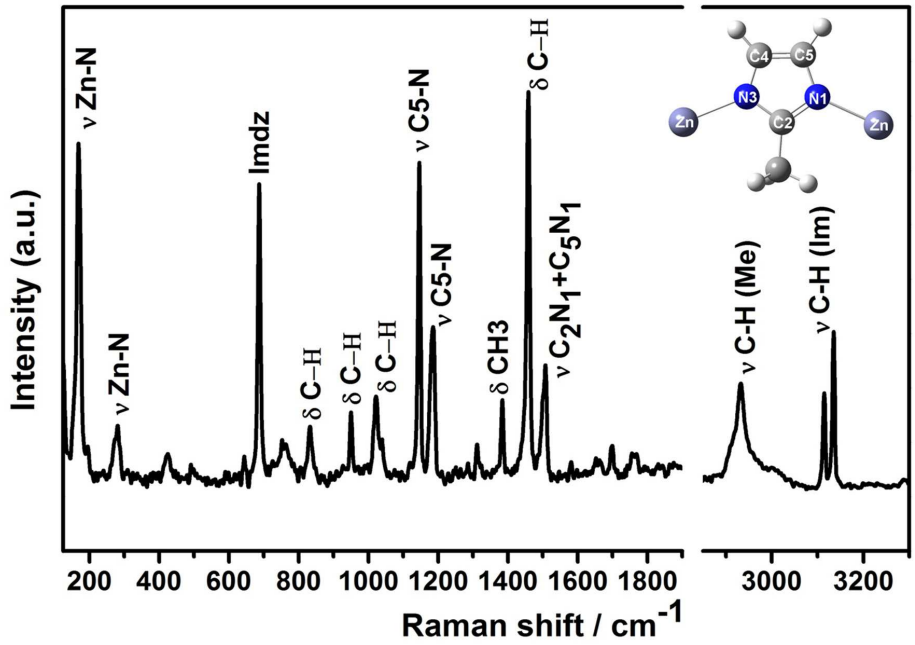

Figure 3.5: RT Raman spectrum of mZIF-8. Inset shows the atom nomenclature used for the imidazole ring, where N is shown in blue, Zn in purple, C in gray, and H in white

no anomaly in full width at half-maximum (fwhm) suggesting that the crystalline phase is retained throughout the temperature range. All the modes remained intact up to 83 K implying that the phase change observed in the X-ray studies [20] is because of the volume change and change in orientation of methyl-imidazole ring leading to expansion of pore volume and not due to structural transition. Imidazole ring mode in mZIF-8 has been known to show flexibility and swing effect with temperature [21, 22]. From the Raman spectra we observe that, as opposed to the normal behaviour, imidazole ring puckering mode starts softening around 200 K and then hardens beyond 150 K as shown in Figure 3.6a. Interestingly, the Zn-N stretching mode also exhibited similar trend with temperature. This behaviour can be explained as follows. As the temperature decreases, the ZIF-8 lattice starts compressing resulting into decrease in bond lengths and hence hardening of frequency. At lower temperatures, lattice compression would be hindered due to steric repulsion

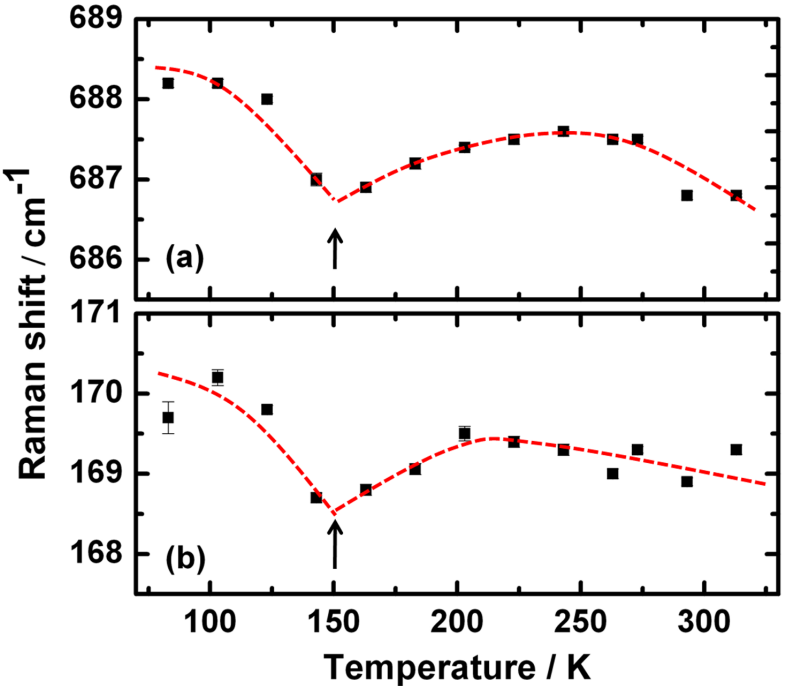

Figure 3.6: Temperature dependence of (a) Imidazole ring puckering and (b) Zn-N stretching in mZIF-8. Red dotted line is guide to the eye.

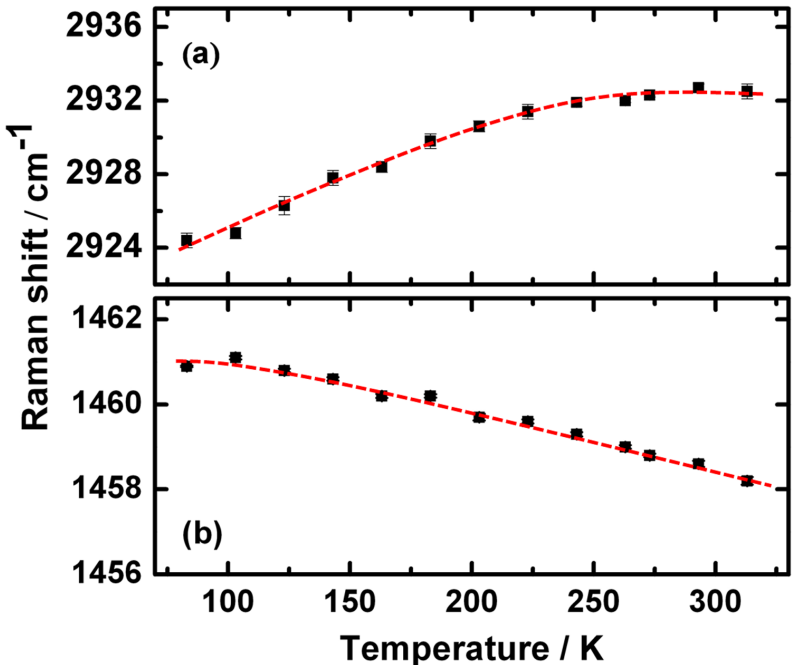

Figure 3.7: Temperature dependence of (a) C-H stretching and (b) C-H bending modes of the methyl group in mZIF-8. Red dotted line is guide to the eye

Frequency (cm^{-1})	Band assignment
168	ν Zn-N
273	ν Zn-N
686	Imdz ring puckering, H oop bend
755	C=N oop bend, δ N-H
833	C-H oop bend (C4-C5)
950	C-H oop bend (C2-H)
1021	C-H oop bend
1146	ν C5-N
1180	ν C-N+N-H wag
1187	ν C-N
1311	ring expansion+N-H wag
1384	δ CH_3
1458	C-H wag
1499	C2N3+C4N3+ν C5N1+N-H wag
1508	ν C4-C5
2915	ν_{sym} C-H (methyl)
2931	ν_{asym} C-H (methyl)
3110	ν C-H (ar)
3131	ν C-H (ar)

* ν-stretch; δ-bend; oop-out of plane; ar-aromatic; sym-symmetric; asym-asymmetric, Imdz-imidazole.

Table 3.1: Raman band assignment of mZIF-8 [30–32].

between the methyl groups on opposite imidazole groups facing each other inside the window. As a consequence, the methyl imidazole moieties swing away from each other opening the channel for guest uptake. This would ease the Zn-N and imidazole strain thus softening their vibrational modes. Beyond 150 K, hardening of these modes are observed due to further compression of mZIF-8 lattice along with the guest molecules. Another implication of ring opening is the increase in the interspace separation between the methyl groups facing each other thereby reducing the steric hindrance consequently leading to softening of C-H stretching frequencies from 2931 cm^{-1} at room temperature to 2924 cm^{-1} at 83 K as shown in Figure 3.7a. Besides, softening of stretching frequencies are accompanied by hardening of bending modes, which is also observed in the C-H bending frequency at 1458 cm^{-1}

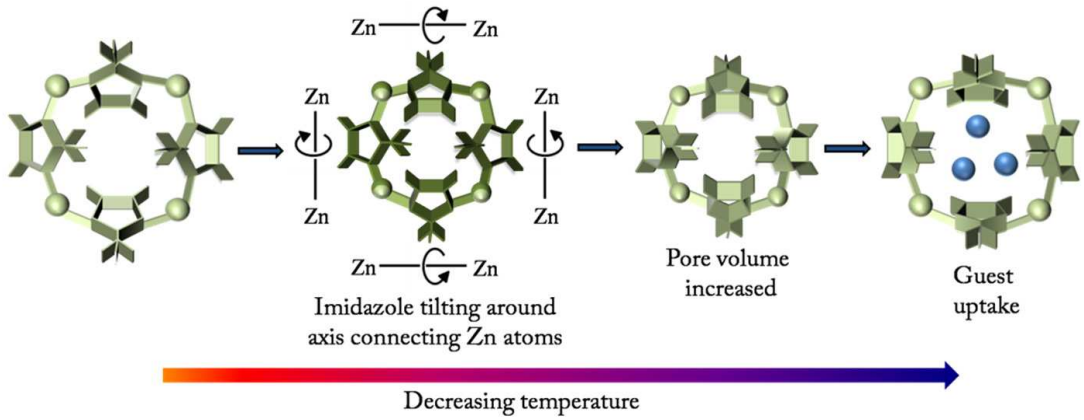

Scheme 3.1: Orientational change of methyl imidazole ring with temperature.

(see Figure 3.7b). The orientational change of the ligand followed by increased guest uptake at low temperatures has been depicted in Scheme 3.1.

Low temperature Raman spectra of mZIF-8 showed the appearance of new peak at 2323 cm^{-1} at 123 K which gained intensity as the temperature was further lowered (Figure 3.8). This peak has been assigned to N-N stretching frequency of encaged nitrogen molecules in pores of mZIF-8. The reduced stretching frequency of trapped nitrogen molecules in comparison to free nitrogen having stretching mode at 2331 cm^{-1}) suggest lower N-N bond strength as a result of its interaction with mZIF-8 framework. Gradual enhancement of adsorbed nitrogen signal intensity with decreasing temperature signifies successive filling of pores (Figure 3.8b). A recent report demonstrate similar results on nitrogen adsorption in ZIF-8 [20].

3.3.2 Raman study of methane adsorption in ZIF-8

For the first time we have studied methane adsorption in mZIF-8 by Raman spectroscopy. Other reports on Raman investigation of methane adsorption in metal organic frameworks (MOFs) include reports by Hamon *et al.* and Sibero-Perez *et al.* who have shown adsorption of methane and other gases in MOFs [33, 34].

Methane has three strong bands in the 100-4000 cm^{-1} regime occuring at 1533, 2917 and 3019 cm^{-1} [35, 36]. Out of these, 2917 cm^{-1} is the most intense mode

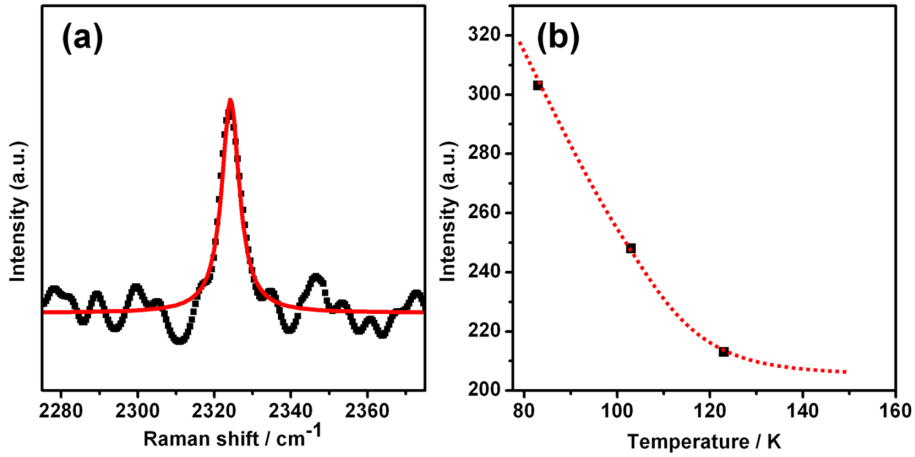

Figure 3.8: (a) Raman spectra showing adsorbed nitrogen peak at 2323 cm^{-1} at 123 K. Red line is the Lorentzian fit to the peak. (b) Nitrogen peak intensity as a function of temperature. Red dotted line is the guide to eye.

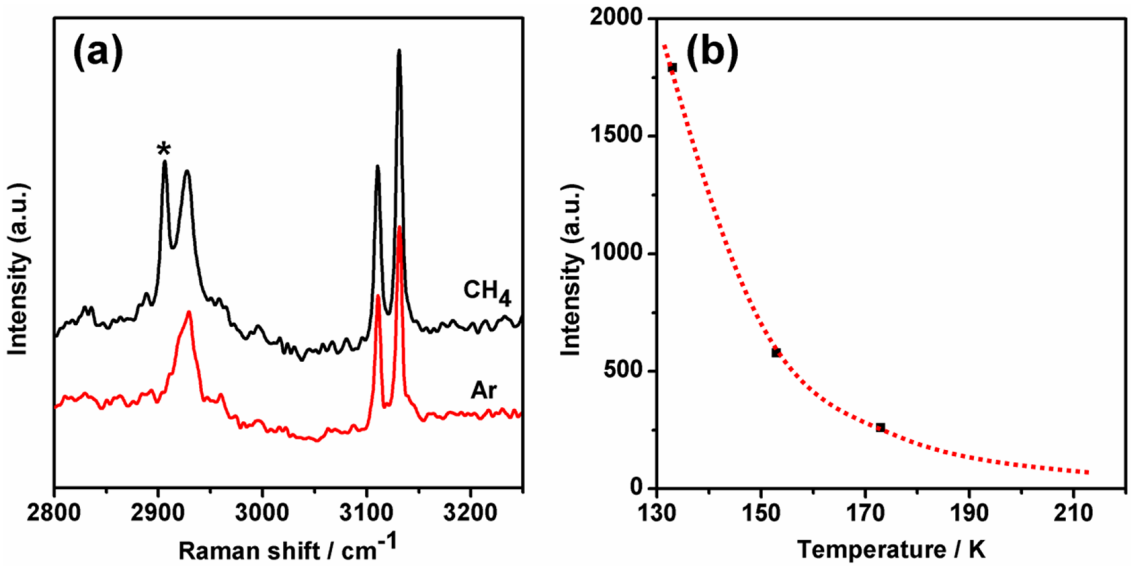

Figure 3.9: (a) Raman spectra of adsorbed CH_4 in mZIF-8 at 153 K (CH_4, black curve), and Raman spectra of mZIF-8 in argon atmosphere (Ar, red curve) at 153 K. The peak at 2904 cm^{-1} marked with a star corresponds to that of adsorbed methane. (b) Methane peak intensity as a function of temperature. Red dotted line is guide to the eye.

corresponding to symmetric C-H stretch. In our Raman studies, we indeed observe a new mode at 2904 cm^{-1} appearing in the methyl peak already present in mZIF-8 spectrum as shown in Figure 3.9a. This mode was assigned to C-H symmetric stretch based on the gaseous methane mode. Methane is a better Raman scatterer than nitrogen [37] and hence we do see its existence even at a temperature as high as 173 K. To validate our results and assert that the new peak indeed belongs to the adsorbed methane gas and does not result from any methyl interactions at low temperature, we carried out the experiment in argon atmosphere. Here, the Raman spectrum of mZIF-8 does not show any new peak in the C-H stretching region (Figure 3.9) reasserting the fact that the 2904 cm^{-1} peak belongs to adsorbed methane in mZIF-8. This peak intensity reduced as the temperature was increased from 133 K to room temperature implying gradual release of methane guest molecules from the host (Figure 3.9b).

Adsorption of methane does not induce any structural transition in mZIF-8 suggesting physisorption. Interestingly, no guest molecular peak appears at room temperature while they arise at low temperature. There are two possible reasons: 1) High kinetic energy of gases at room temperature limits adsorption of gases in the pores and hence cannot be detected by Raman studies. Lesser thermal energy of gases at low temperatures favors high adsorption and close packing of guest molecules, 2) Ring opening as a result of swinging of methyl-imidazole ring widens the channel allowing more guest molecules into the pore. Although, the former plays significant role for adsorption of gases in porous materials, we believe that swinging of methyl-imidazole ring is the prime reason for increased guest uptake in mZIF-8 below 150 K.

Methane interaction sites in ZIF-8 have been predicted previously by neutron diffraction experiments and simulation studies [21, 38]. There are four interaction sites [21]. Site I which is known as “IM” site refers to the position above C4=C5 bond

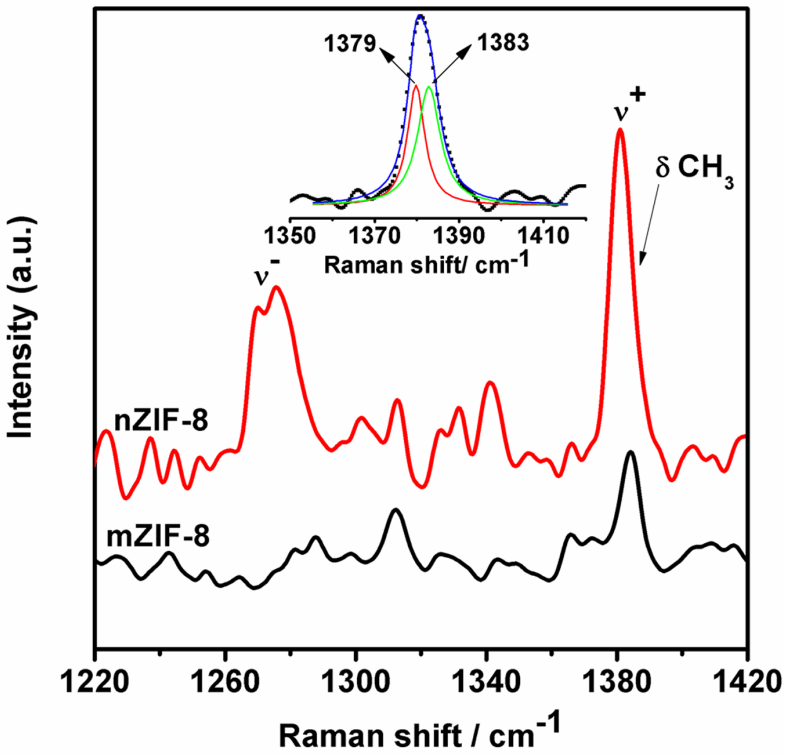

Figure 3.10: Fermi resonance (ν^- and ν^+) modes of adsorbed carbon dioxide in nZIF-8 at 203 K (red curve). Absence of CO_2 modes in mZIF-8 at 203 K (black curve). Inset shows the deconvoluted peaks at 1379 cm^{-1} (CO_2) and 1383 cm^{-1} (δ CH_3). The arrow pointing at the red curve at 1383 cm^{-1} shows the position of methyl bending mode.

in the plane perpendicular to that of the imidazole ring. Site II is the center of the channel formed by the 6 ZnN_4 tetrahedron with three methyl groups pointing outside and other three methyl groups pointing inside. Further loading occurs at site III and site IV wherein the former is at the center of the "nanocage" (term coined by previous authors) formed by site I and site II while the later is localized in the middle of the 4-ring pore at the center of the cube face [21, 38]. From the intensity versus temperature plot shown in Figure 3.9b, it is understood that there is sequential loading of methane gas in mZIF-8 as the intensity gradually increases with decreasing temperature.

3.3.3 Raman Study of Carbon Dioxide Adsorption in ZIF-8

We further conducted Raman measurements of carbond dioxide adsorption in mZIF-8 similar to previous previous experiments. Surprisingly, we did not get any peak of CO_2 at room temperature or at 195 K (Figure 3.10, black curve). Experiment was repeated to confirm the observed results. Earlier studies on CO_2 adsorption in MOFs reveal two peaks at 1276 cm^{-1} and 1380 cm^{-1}. From adsorption studies, we know that nZIF-8 has higher CO_2 uptake than mZIF-8. So, we proceeded to do Raman measurements of CO_2 adsorption in nZIF-8 at room temperature and at 203 K (experiments were performed above the sublimation point, 195 K, to prevent condensation of CO_2) and we indeed saw a new peak at around 1270 cm^{-1}. Red curve in Figure 3.10 shows the Fermi resonance peak of CO_2 at 1270 and 1276 cm^{-1}. The splitting in ν^- could be due to the difference in interaction energies of CO_2 on the surface and in the pores of nZIF-8. Since the ν^+ mode of CO_2 coincides with the methyl bending frequency, we deconvoluted the peak at 1380 cm^{-1} to find the ν^+ at 1379 cm^{-1}. The downshift indicates weakened bond strength due to interaction of CO_2 with the nZIF-8 framework.

3.4 Conclusions

We have investigated molecular level changes in ZIF-8 under various conditions of temperature and gas adsorption through Raman spectroscopy and subsequently addressed the issue of adsorption of smaller gas molecules through the larger channels. ZIF-8 exhibits framework flexibility due to swinging of methyl-imidazole ring resulting in weakening of the Zn-N mode which is observed as softening of Zn-N mode in the Raman spectra. Beyond 150 K lattice compression occurs leading to swinging of methyl-imidazole ring to evade the problem of steric repulsion between the methyl groups. This leads to opening of channels hence favoring nitrogen and

methane gas uptake at low temperatures which was confirmed by the presence of their Raman modes at 2323 cm^{-1} and 2904 cm^{-1} repectively. Although, carbon dioxide has kinetic diameter similar to nitrogen and methane, low uptake results from narrow channel size at 195 K in mZIF-8. Presence of Fermi resonance modes of CO_2 at 1379 cm^{-1} and 1270 cm^{-1} in nZIF-8 is due to larger surface area of nanoscale framework and readily accessible pores in nanometer size crystals of nZIF-8.

Bibliography

[1] R. Banerjee *et al.*, *Control of pore size and functionality in isoreticular zeolitic imidazolate frameworks and their carbon dioxide selective capture properties*, Journal of the American Chemical Society **131**, 3875 (2009).

[2] N. Chang, Z.-Y. Gu, and X.-P. Yan, *Zeolitic imidazolate framework-8 nanocrystal coated capillary for molecular sieving of branched alkanes from linear alkanes along with high-resolution chromatographic separation of linear alkanes*, Journal of the American Chemical Society **132**, 13645 (2010).

[3] A. Huang *et al.*, *A highly permeable and selective zeolitic imidazolate framework ZIF-95 membrane for H_2/CO_2 separation*, Chemical Communications **48**, 10981 (2012).

[4] Y. Pan and Z. Lai, *Sharp separation of C2/C3 hydrocarbon mixtures by zeolitic imidazolate framework-8 (ZIF-8) membranes synthesized in aqueous solutions*, Chem. Commun. **47**, 10275 (2011).

[5] K. Li *et al.*, *Zeolitic imidazolate frameworks for kinetic separation of propane and propene*, Journal of the American Chemical Society **131**, 10368 (2009).

[6] H. Bux, C. Chmelik, R. Krishna, and J. Caro, *Ethene/ethane separation by*

the MOF membrane ZIF-8: molecular correlation of permeation, adsorption, diffusion, Journal of Membrane Science **369**, 284 (2011).

[7] J. Zakzeski, A. Debczak, P. C. Bruijnincx, and B. M. Weckhuysen, *Catalytic oxidation of aromatic oxygenates by the heterogeneous catalyst Co-ZIF-9*, Applied Catalysis A: General **394**, 79 (2011).

[8] C. M. Miralda *et al.*, *Zeolitic imidazole framework-8 catalysts in the conversion of CO_2 to chloropropene carbonate*, ACS Catalysis **2**, 180 (2011).

[9] Y. Hwang *et al.*, *Zeolitic imidazolate framework-coupled resonators for enhanced gas detection*, Journal of Micromechanics and Microengineering **23**, 125027 (2013).

[10] P. Xu, X. Li, H. Yu, and T. Xu, *Advanced Nanoporous Materials for Micro-Gravimetric Sensing to Trace-Level Bio/Chemical Molecules*, Sensors **14**, 19023 (2014).

[11] K. S. Park *et al.*, *Exceptional chemical and thermal stability of zeolitic imidazolate frameworks*, Proceedings of the National Academy of Sciences **103**, 10186 (2006).

[12] B. P. Biswal, T. Panda, and R. Banerjee, *Solution mediated phase transformation (RHO to SOD) in porous Co-imidazolate based zeolitic frameworks with high water stability*, Chemical Communications **48**, 11868 (2012).

[13] T. Panda *et al.*, *Amino functionalized zeolitic tetrazolate framework (ZTF) with high capacity for storage of carbon dioxide*, Chemical Communications **47**, 2011 (2011).

[14] R. Banerjee *et al.*, *High-throughput synthesis of zeolitic imidazolate frameworks and application to CO_2 capture*, Science **319**, 939 (2008).

[15] T. D. Bennett *et al.*, *Facile mechanosynthesis of amorphous zeolitic imidazolate frameworks*, Journal of the American Chemical Society **133**, 14546 (2011).

[16] J. Cravillon *et al.*, *Controlling zeolitic imidazolate framework nano-and microcrystal formation: Insight into crystal growth by time-resolved in situ static light scattering*, Chemistry of Materials **23**, 2130 (2011).

[17] Y. Hu *et al.*, *In situ high pressure study of ZIF-8 by FTIR spectroscopy*, Chem. Commun. **47**, 12694 (2011).

[18] J. Pérez-Pellitero *et al.*, *Adsorption of CO_2, CH_4, and N_2 on zeolitic imidazolate frameworks: experiments and simulations*, Chemistry-A European Journal **16**, 1560 (2010).

[19] D. Fairen-Jimenez *et al.*, *Opening the gate: framework flexibility in ZIF-8 explored by experiments and simulations*, Journal of the American Chemical Society **133**, 8900 (2011).

[20] J.-P. Zhang, A.-X. Zhu, and X.-M. Chen, *Single-crystal X-ray diffraction and Raman spectroscopy studies of isobaric N_2 adsorption in SOD-type metal–organic zeolites*, Chemical Communications **48**, 11395 (2012).

[21] D. Fairen-Jimenez *et al.*, *Flexibility and swing effect on the adsorption of energy-related gases on ZIF-8: combined experimental and simulation study*, Dalton Transactions **41**, 10752 (2012).

[22] C. O. Ania *et al.*, *Understanding gas-induced structural deformation of ZIF-8*, The Journal of Physical Chemistry Letters **3**, 1159 (2012).

[23] P. Kanoo *et al.*, *Unusual room temperature CO_2 uptake in a fluoro-functionalized MOF: insight from Raman spectroscopy and theoretical studies*, Chemical Communications **48**, 8487 (2012).

[24] J. Seo *et al.*, *Soft secondary building unit: dynamic bond rearrangement on multinuclear core of porous coordination polymers in gas media*, Journal of the American Chemical Society **133**, 9005 (2011).

[25] N. Nijem *et al.*, *Understanding the preferential adsorption of CO_2 over N_2 in a flexible metal–organic framework*, Journal of the American Chemical Society **133**, 12849 (2011).

[26] K. Jayaramulu *et al.*, *Honeycomb Porous Framework of Zinc (II): Effective Host for Palladium Nanoparticles for Efficient Three-Component (A3) Coupling and Selective Gas Storage*, ChemPlusChem **77**, 743 (2012).

[27] W. Morris *et al.*, *NMR and X-ray study revealing the rigidity of zeolitic imidazolate frameworks*, The Journal of Physical Chemistry C **116**, 13307 (2012).

[28] J. Cravillon *et al.*, *Rapid room-temperature synthesis and characterization of nanocrystals of a prototypical zeolitic imidazolate framework*, Chemistry of Materials **21**, 1410 (2009).

[29] G. P. Kumar and C. Narayana, *Adapting a fluorescence microscope to perform surface enhanced*, Current science **93**, 778 (2007).

[30] L. M. Markham, L. C. Mayne, B. S. Hudson, and M. Z. Zgierski, *Resonance Raman studies of imidazole, imidazolium, and their derivatives: the effect of deuterium substitution*, The Journal of Physical Chemistry **97**, 10319 (1993).

[31] D. A. Carter and J. E. Pemberton, *Raman spectroscopy and vibrational assignments of 1-and 2-methylimidazole*, Journal of Raman spectroscopy **28**, 939 (1997).

[32] C.-J. Mao *et al.*, *Synthesis of zinc 1-(2-pyridylazo)-2-naphthol ($Zn(PAN)_2$) nanobelts with nonlinear optical property*, CrystEngComm **14**, 6823 (2012).

[33] L. Hamon *et al.*, *Co-adsorption and Separation of CO_2-CH_4 Mixtures in the Highly Flexible MIL-53(Cr) MOF*, Journal of the American Chemical Society **131**, 17490 (2009).

[34] D. Y. Siberio-Pérez, A. G. Wong-Foy, O. M. Yaghi, and A. J. Matzger, *Raman spectroscopic investigation of CH_4 and N_2 adsorption in metal-organic frameworks*, Chemistry of materials **19**, 3681 (2007).

[35] T. Shimanouchi, Technical report, DTIC Document (unpublished).

[36] R. Dickinson, R. Dillon, and F. Rasetti, *Raman spectra of polyatomic gases*, Physical Review **34**, 582 (1929).

[37] S. J. Hart and R. A. Lamontagne, Technical report, DTIC Document (unpublished).

[38] H. Wu, W. Zhou, and T. Yildirim, *Methane sorption in nanoporous metal-organic frameworks and first-order phase transition of confined methane*, The Journal of Physical Chemistry C **113**, 3029 (2009).

Chapter 4

Temperature Induced Structure Evolution and Carbon Dixode Capture by Fluoro-functionalized MOF

4.1 Introduction

The alarming increase in the atmospheric carbon dioxide levels due to emissions from the petrochemical industries, burning of fossil fuels, automobile exhausts in the last few decades is a matter of great concern today. Development of effective systems for carbon dioxide capture and sequestration is an important field of research. The various ways to capture carbon dioxide from gaseous mixture include

"Unusual room temperature CO_2 uptake in a fluoro-functionalized MOF: insight from Raman spectroscopy and theoretical studies" *Chem. Commun.* **2012**, *48*, 8487-8489 - Reproduced by permission of The Royal Society of Chemistry. http://pubs.rsc.org/en/content/articlelanding/2012/CC/C2CC34276F

cryogenic distillation, adsorption by solvent or solid sorbents and membrane purification [1, 2]. Due to cost limitation or in-efficiency in adsorbing carbon dioxide present in low concentration (which is the case for industrial emissions), cryogenic distillation or membrane purification is not possible. Aqueous amines are potential sorbents and are used as standard to gauge the potential of new materials. Whether a sorbent is a prospective material (or not) for carbon dioxide capture is decided on the basis of its adsorption capacity, adsorption-desorption kinetics, enthalpy of adsorption, selectivity, operating conditions, stability and regenerability [2, 3].

Recently, metal organic frameworks (MOFs) have emerged as prospective materials for carbon dioxide capture due to their structural flexibility and tunability, and large potency for gas adsorption. The ability to maneuver the framework structure using various molecular strut to obtain a desired characteristics makes them a fascinating class of materials for gas adsorption. Most MOFs have inherent porosity and the pore size may vary from few Angstrom to a few nanometers. Separation of small molecules like carbon dioxide from flue gas or any gaseous mixture necessitates the presence of ultra-micropores which permits only small gases. Functionalizing such pores with strongly polarizing sites aid the binding process due to enhanced interaction attributed to the larger polarizability and quadrupole moment of carbon dioxide. This facilitates increased adsorption of gas molecules onto the framework even at low pressures. $[\{Zn(SiF)_6(pyz)_2\} \cdot 2MeOH]_n$ is one such MOF containing highly polar group SiF_6^{2-} [4].

Generally, the gas uptake by any material reduces as the temperature increases due to larger kinetic energy of gases or weakened adsorbate-adsorbent interactions. Quite unusual to the normal behaviour, it was found that carbon dioxide adsorption in $[\{Zn(SiF)_6(pyz)_2\} \cdot 2MeOH]_n$ was higher at room temperature (298 K) than at 195 K. Raman spectroscopy can provide signatures of structural or molecular changes in a material resulting from the gas adsorption or temperature/pressure variation and

so, to understand the preferential adsorption at room temperature, we performed Raman spectroscopic measurements which would provide an insight into the mechanistic aspects of unusual CO_2 adsorption behaviour at various temperatures.

4.2 Experimental details

All the reagents and solvents employed were commercially available and used without further purification. $ZnSiF_6{\cdot}xH_2O$ and pyrazine were obtained from Sigma Aldrich Chemical Co. $[\{Zn(SiF)_6(pyz)_2\} \cdot 2MeOH]_n$ were synthesized using the previously reported procedure [4]. Powder X-ray diffraction patterns were recorded on a Bruker D8 Discover intrument using Cu-Kα radiation. Raman measurements were carried out on custom-built Raman spectrometer using HeNe laser of wavelength 632.8 nm. Linkam THMS 600 heating-cooling stage was used for all the temperature depdendent Raman measurements. Typical accumulation time was 30 s for each spectrum. The spectra reported here are smoothed using 5 point FFT, and baseline corrected. Gases used for all the gas adsorption measurements were of scientific grade with 99.999% purity.

4.3 Results and discussions

$[\{Zn(SiF)_6(pyz)_2\}{\cdot}2MeOH]_n$ was synthesized by previously reported procedure [4] and characterzied by PXRD studies. It has a α-Po types structure where 2D $\{Zn(pyz)_2\}_n$ are stacked by axially coordinating SiF_6^{2-} ligands as shown in Figure 4.1a. The framework has 1D channels (4.5×4.5 Å^2) lined with pendant fluorine atoms facing the pore. Non-coordinated Fluorine atoms can be the site for electrostatic interactions leading to atypical adsorption properties as shown by other fluorofunctionalized coordination polymers [5, 6]. Interestingly, $[\{Zn(SiF)_6(pyz)_2\}{\cdot}2MeOH]_n$

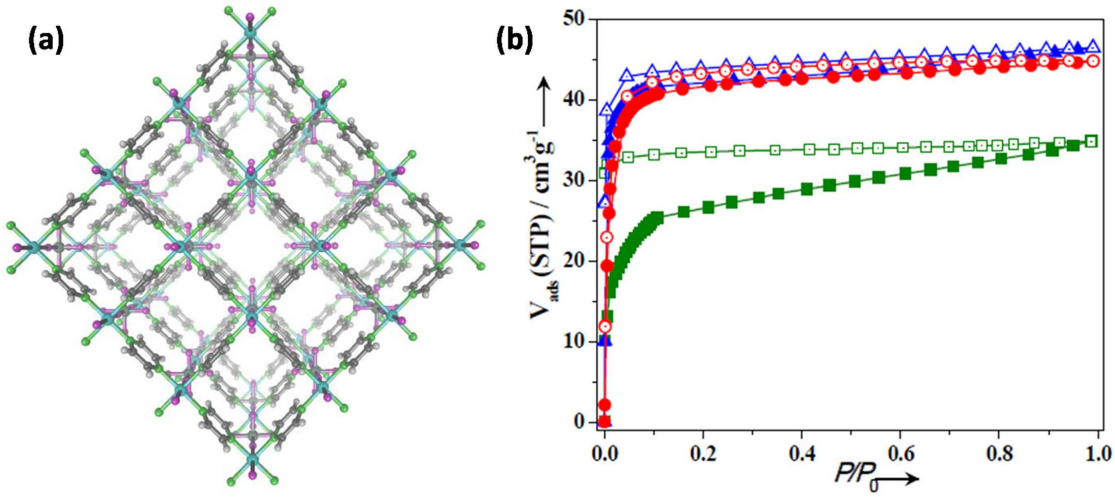

Figure 4.1: (a) 3D view of $[\{Zn(SiF)_6(pyz)_2\}\cdot 2MeOH]_n$ showing 1D channel along c-direction, (b) CO_2 adsorption-desorption isotherms at 195 K (green), 273 K (red), 298 K (blue). Adsorption and desorption is indicated by close symbol and open symbol respectively. $P_\circ$ is the saturated vapour pressure of CO_2

shows unusally high CO_2 adsorption at 298 K in comparison to that at 195 K (Figure 4.1b). To understand this exceptional behaviour, we performed Raman studies which gives molecular level information.

Figure 4.2 presents the room temperature Raman spectrum of as-synthesized $[\{Zn(SiF)_6(pyz)_2\}\cdot 2MeOH]_n$. The Raman spectrum features distinct pyrazine modes, Si-F modes and lattice vibrations. Table 4.1 summarizes the band assignment of the framework [7–11]. The frequencies below 300 cm^{-1} have been assigned to the lattice modes, the Zn-F and Zn-N stretching frequencies. The mode at 1236 cm^{-1} is assigned to the pyrazine hydrogen bend. The 1525 cm^{-1} peak is due to pyrazine ring CC stretch and the 1620 and 1700 cm^{-1} are sum tones.

On CO_2 adsorption at room temperature, there is no structural transition as is evident from the Raman spectrum, whilst two new modes appear at 1276 cm^{-1} and 1380 cm^{-1} as shown in Figure 4.3. These modes arise due to coupling of fundamental symmetric stretch with the first overtone of bending mode of adsorbed CO_2 (Fermi resonance) [12]. These values are downshifted with respect to that reported

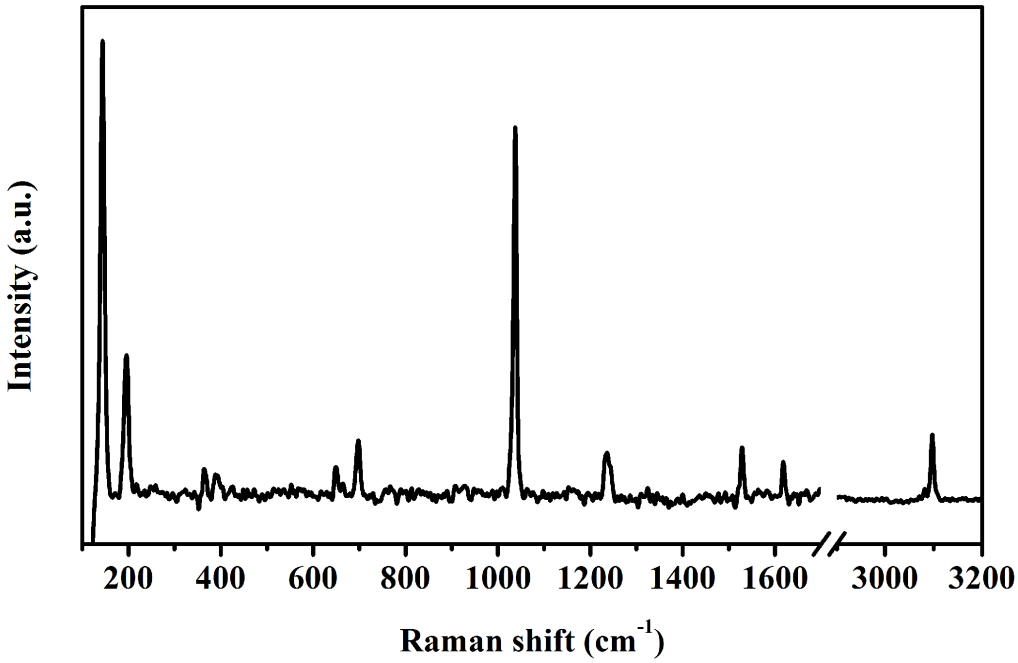

Figure 4.2: Room temperature Raman spectrum of as-synthesized $[\{Zn(SiF)_6(pyz)_2\}\cdot 2MeOH]_n$.

Frequency (cm^{-1})	Assignment
145	lattice vibration, δ N-Zn-N
197	lattice vibration, δ F-Zn-N
649	pyz ring ν_4
663	Si-F
707	ν Si-F_6, ν_{10} pyz
757	pyz H bend ν_{10a}, Zn-F
1025	$\nu_{pyz-ring}$
1036	$\nu_{pyz-ring}$
1236	ν_{9a} pyz H bend
1525	$\nu_{pyz-ring}$
1529	$\nu_{pyz-ring}$
1620	pyz (609+1015)
3071	ν C-H
3081	ν C-H
3096	ν C-H

* δ-in plane deformation; ν-stretch; pyz-pyrazine.

Table 4.1: Raman band assignment of $[\{Zn(SiF)_6(pyz)_2\}\cdot 2MeOH]_n$ [7–11].

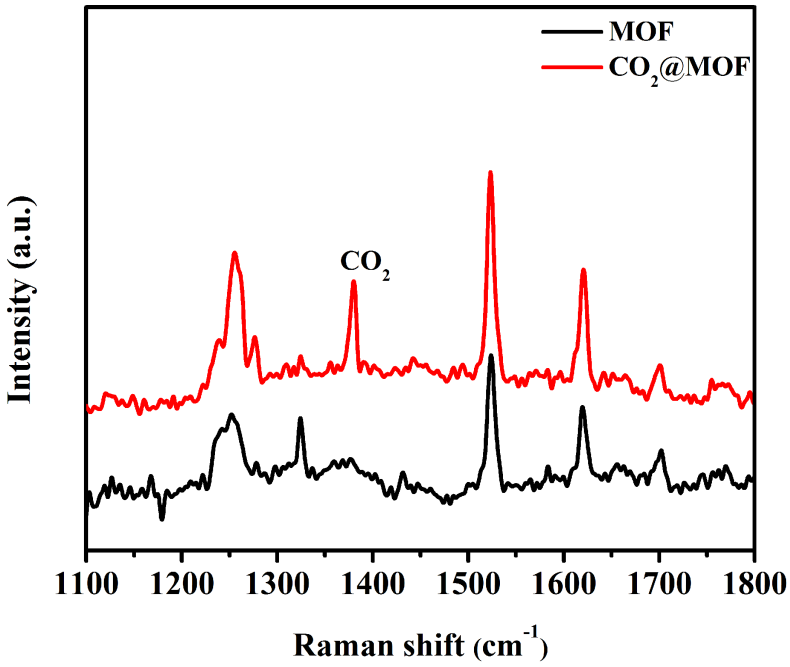

Figure 4.3: Raman spectra of MOF and CO_2 adsorbed in MOF (CO_2@MOF). 1380 cm^{-1} peak corresponds to adsorbed CO_2.

for gaseous CO_2 and can be attributed to its interaction with the framework. No CO_2 modes were observed on purging the gas into Linkan stage at -70 °C indicating no or fewer CO_2 molecules adsorbed in the framework.

To understand the unusual gas adsorption, temperature dependent Raman spectra of framework was recorded and presented in Figure 4.4. Heating as-synthsized framework to 50 °C reveals two new modes at 3117 and 3134 cm^{-1}. As the temperature is reduced, these modes intensify further. In MOFs, pyrazine rings are known to show rotational degree of freedom [13, 14] and such local flexibility would change the symmetry of the modes. At room temperature, pyrazine rings have sufficient energy to swing open for the adsorption of CO_2 guest molecules. Figure 4.5 depicts the orientation of pyrazine ring with respect to framework axis in its native form and with CO_2 adsorbed. In this position, the pyrazine ring is planar to the framework axis implying greater symmertry and also the degeneracy of the C-H modes, hence we observe only two modes. In absence of guest molecules, pyrazine ring swings and

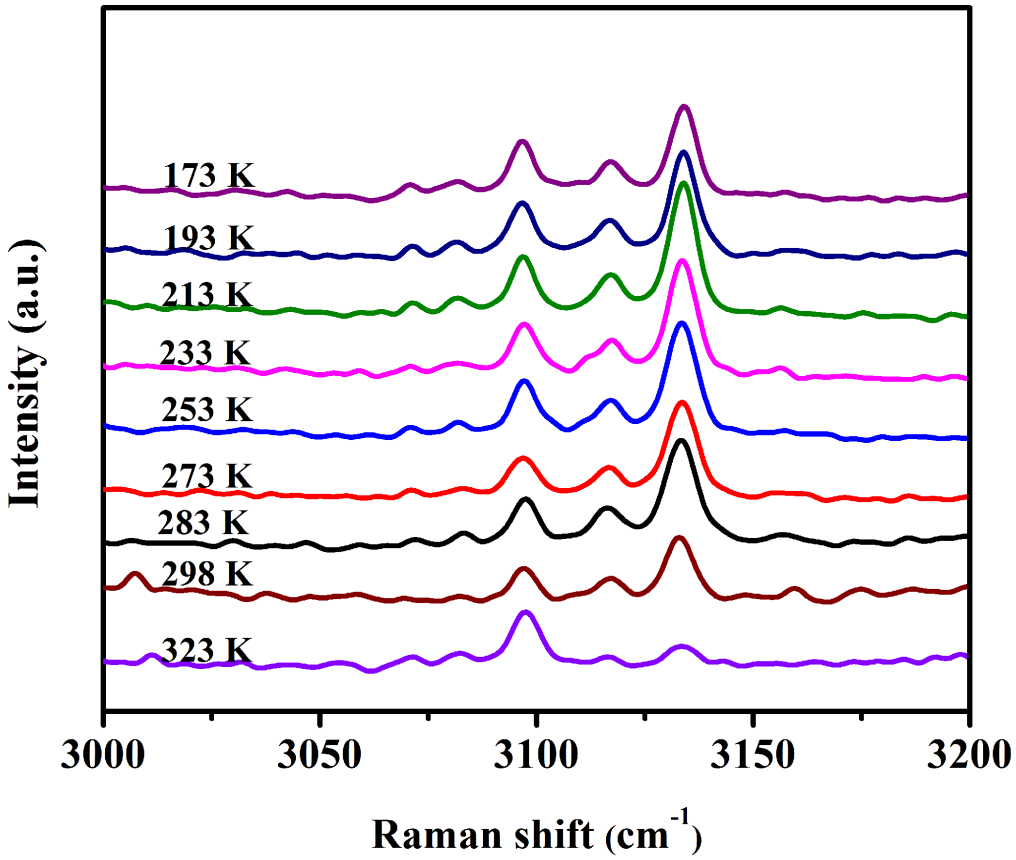

Figure 4.4: Temperature dependent Raman spectra of MOF showing evolution of C-H stretching frequencies.

is at an angle to the framework axis. At low temperature, this pyrazine ring tilt is almost frozen in space thus obstructing the channel window and accounting for lower diffusivity of CO_2 in MOF at 195 K.

To further probe the structural transition in this framework, temperature of guest CO_2 adsorbed MOF was reduced from RT to -70 °C (Figure 4.6). It was found that the high frequency new modes observed previously, occur at 3123 and 3134 cm^{-1} in the present studies but are weak in intensity. In addition, there is an upshift of 4-5 cm^{-1} in few C–H stretching frequencies of pyrazine suggesting stiffening in the modes. We conjecture that in presence of CO_2, the pyrazine ring cannot tilt thus accounting for the low intensity of higher C-H stretching frequencies. This

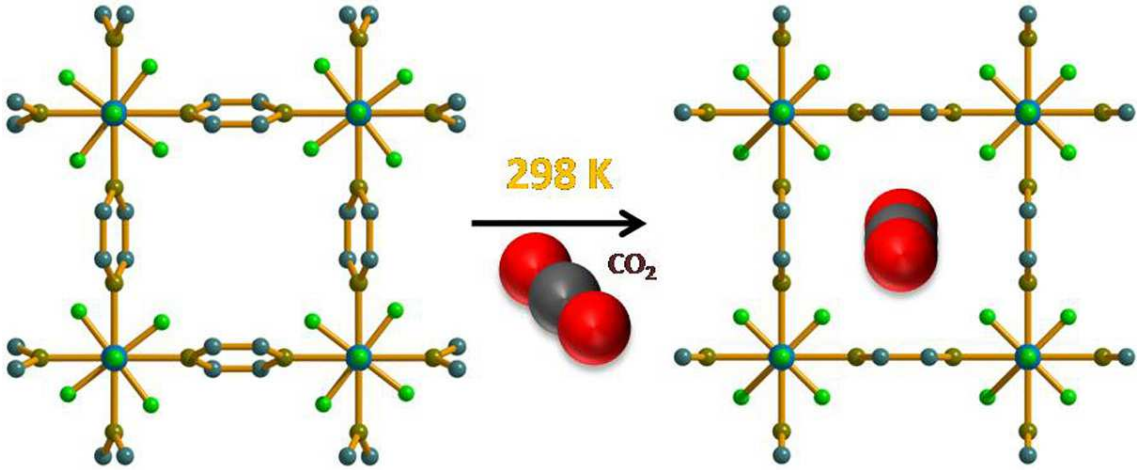

Figure 4.5: Depiction of pyrazine ring tilt in desolvated framework and after CO_2 uptake.

hypothesis is further supported by density functional theory calculation and molecular dynamics simulations which reveals a canting angle of 17.2° between the plane formed by tilted pyrazine ring and the (200) plane of the framework [15]. The tilting of pyrazine ring reduces the accessible surface area and is responsible for reduced CO_2 uptake at 195 K.

4.4 Conclusion

Herein, we report an exceptional CO_2 adsorption phenomenon in fluoro-functionalized $[\{Zn(SiF)_6(pyz)_2\}\cdot 2MeOH]_n$ framework. This framework shows high CO_2 uptake at 298 K than at 195 K which is attributed to the flexibility of pyrazine ring as observed by Raman measurements. The tilted pyrazine rings impede CO_2 uptake at 195 K by blocking the channel. Simulation results further conform to the experimental observation and suggest electrostatic interaction between CO_2 and fluorine atoms in the framework. This study would encourage research on new MOFs with higher room temperature CO_2 uptake for application in gas separation and storage at industrial scale.

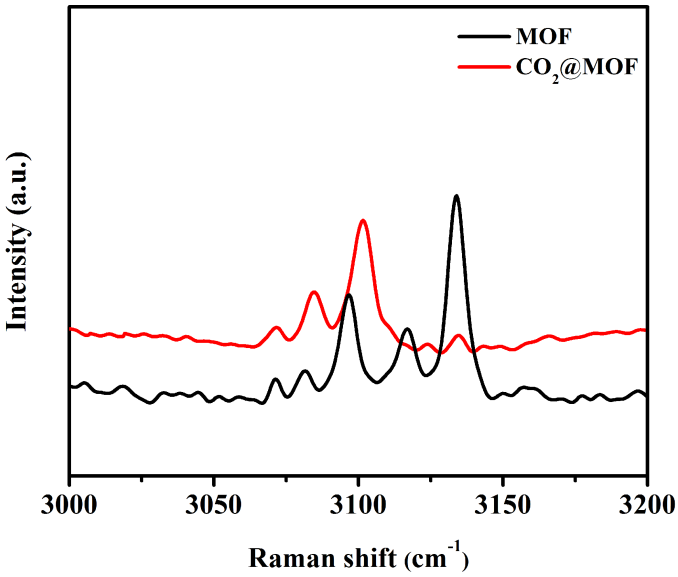

Figure 4.6: C-H stretching frequencies in MOF and CO_2@MOF at 195 K.

Bibliography

[1] D. Aaron and C. Tsouris, *Separation of CO_2 from Flue Gas: A Review*, Separation Science and Technology **40**, 321 (2005).

[2] S. Choi, J. H. Drese, and C. W. Jones, *Adsorbent materials for carbon dioxide capture from large anthropogenic point sources*, ChemSusChem **2**, 796 (2009).

[3] K. Sumida *et al.*, *Carbon dioxide capture in metal–organic frameworks*, Chemical reviews **112**, 724 (2012).

[4] K. Uemura *et al.*, *Syntheses, crystal structures and adsorption properties of ultramicroporous coordination polymers constructed from hexafluorosilicate ions and pyrazine*, European Journal of Inorganic Chemistry **2009**, 2329 (2009).

[5] S. D. Burd *et al.*, *Highly selective carbon dioxide uptake by [Cu(bpy-n)$_2$(SiF$_6$)](bpy-1=4,4'-Bipyridine; bpy-2=1, 2-Bis(4-pyridyl)ethene)*, Journal of the American Chemical Society **134**, 3663 (2012).

[6] J. Liu *et al.*, *Progress in adsorption-based CO_2 capture by metal–organic frameworks*, Chemical Society Reviews **41**, 2308 (2012).

[7] Y. Saito, M. Cordes, and K. Nakamoto, *Metal isotope effect on metal-ligand vibrations—VIII: Far-infrared and Raman spectra of zinc halide complexes of pyridine*, Spectrochimica Acta Part A: Molecular Spectroscopy **28**, 1459 (1972).

[8] R. Lord, A. Marston, and F. A. Miller, *Infra-red and Raman spectra ot the diazines*, Spectrochimica Acta **9**, 113 (1957).

[9] G. M. Begun and A. C. Rutenberg, *Vibrational frequencies and force constants of some Group IVa and Group Va hexafluoride ions*, Inorganic Chemistry **6**, 2212 (1967).

[10] G. Sbrana, V. Schettino, and R. Righini, *Phase transition in crystalline pyrazine. Infrared and Raman spectra*, The Journal of Chemical Physics **59**, 2441 (1973).

[11] S. Califano, G. Adembri, and G. Sbrana, *Vapour and crystal spectra in polarized light of pyrazine-d_0, cis pyrazine-d_2 and pyrazine-d_4*, Spectrochimica Acta **20**, 385 (1964).

[12] R. Dickinson, R. Dillon, and F. Rasetti, *Raman spectra of polyatomic gases*, Physical Review **34**, 582 (1929).

[13] D. Tanaka *et al.*, *Porous Coordination Polymer with π Lewis Acidic Pore Surfaces,$\{[Cu_3(CN)_3\{hat(CN)_3$ $-(OEt)_3\}]\cdot 3THF\}_n$*, Angewandte Chemie **118**, 4744 (2006).

[14] S. Horike *et al.*, *Dynamic motion of building blocks in porous coordination polymers*, Angewandte Chemie International Edition **45**, 7226 (2006).

[15] P. Kanoo *et al.*, *Unusual room temperature CO_2 uptake in a fluoro-functionalized MOF: insight from Raman spectroscopy and theoretical studies*, Chemical Communications **48**, 8487 (2012).

Chapter 5

Understanding Guest and Pressure Induced Porosity through Structural Transition in Flexible Interpenetrated MOF by Raman Spectroscopy

5.1 Introduction

Synthesis of wide variety of metal organic frameworks (MOFs) having different linkers and metal atoms giving rise to diverse functionality such as gas storage [1, 2], separation [3, 4], catalysis [5, 6] have gained paramount importance in past few years. Framework flexibility, dynamicity and pore size tunability make MOFs suitable material for applications in gas storage or separation, conductivity, magnetism, fluorescence [6–15]. However, many of such frameworks collapse on removal of solvent molecules due to lack of stabilizing interactions. Recent discoveries of highly

stable and flexible frameworks have brought us to the *third generation* of MOFs [16–19]. These frameworks show dynamic structural behavior such as deformation of nets, rotation of aromatic rings or sliding of interpenetrated nets in response to external stimuli resulting into stepwise or gated adsorption profiles. Framework dynamicity can be introduced by cleavage/formation of metal-ligand bond and rotation or deformation of ligand moiety [20, 21]. External stimuli such as temperature, pressure or desolvation can also induce dynamics in the framework [22–24]. It is known that the adsorption properties are enhanced (or suppressed at times) by the external stimulus but there is limited information on how it happens. Further, structural determination becomes difficult from XRD when the framework loses its single-crystallinity after such transformations. Thus, there is a need to understand the molecular changes associated with the transformations that can further assist us in designing MOFs for enhanced properties.

Raman spectroscopy is an analytical technique which probes the vibrational modes of the molecule. Secondly, it does not require any sample preparation. Therefore, it can be used to understand the molecular interactions in MOFs. So far it has not been extensively used to study coordination polymers and hence there is immense scope to explore and obtain information about the structural, geometrical and molecular changes in MOFs from Raman spectroscopic studies [25]. It must be emphasized here that unlike most absorption processes, Raman spectroscopy which is a scattering technique is influenced by charges and spin. Hence, interpretation require users to be proficient in Raman spectroscopy. In some of the earlier reports, structural transitions and guest-host interactions in MOFs have been probed by vibrational spectroscopy [26–28]. Nijem *et al.* investigated framework flexibility and interaction of CO_2 with the framework using IR and Raman spectroscopy [29, 30]. Siberio-Pérez *et al.* have probed methane and nitrogen adsorption in MOFs through Raman spectroscopy [31]. In this chapter, we attempt to understand the

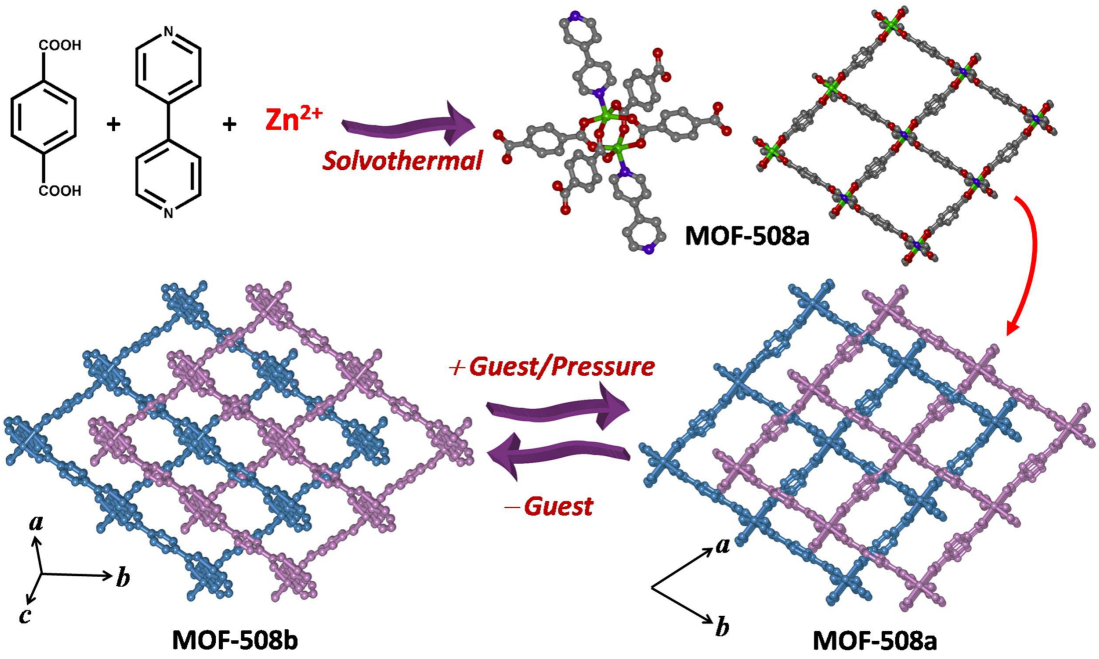

Scheme 5.1: Schematic representation of secondary building unit and the 2D framework of interpenetrating MOF-508 in its native form, MOF-508a and de-solvated form, MOF-508b.

phase transition in MOF-508 by Raman spectroscopy wherein molecular signatures of the structural transitions are revealed by changes in the vibrational features.

MOF-508a was first reported by Ma *et al.* in 2005 [32]. It can be represented by formula $[Zn(BDC)(BPY)_{0.5}{\cdot}DMF(H_2O)_{0.5}]$, where BDC is 1,4-benzene dicarboxylic acid and BPY is 4,4′-bipyridine (Scheme 5.1). It is an interpenetrating framework which can slide on inclusion or removal of guest molecule without any bond cleavage. There is a reduction in the volume by 16.7 % on going from an open porous form (guest adsorbed, MOF-508a) to a closed non-porous form (guest free, MOF-508b having formula $[Zn(BDC)(BPY)_{0.5}]$ [33]. There is no report or experimental proof about the nature of interactions that exist or hold together the two interpenetrating frameworks, although C-H$\cdots\pi$ and $\pi\cdots\pi$ interactions are expected to be the possible interactions stabilizing this framework [34]. Our endeavour here is to understand the interactions stabilising MOF-508 framework by Raman spectroscopy

and thereby monitor the changes occurring in its spectrum influenced by external stimuli (temperature/pressure or gas adsorption) and to infer its relationship with the structural changes.

5.2 Experimental details

All the reagents and solvents employed were commercially precured and used as supplied without further purification. $Zn(NO_3)_2{\cdot}6H_2O$, 4,4′-bipyridine and 1,4-benzene dicarboxylic acid were purchased from Sigma-Aldrich. MOF-508a was prepared by the method reported by Chen *et al.* [33]. 0.3529 g of $Zn(NO_3)_2{\cdot}6H_2O$ was added to a N, N- dimethylformamide (DMF)/ethanol mixture (5 mL:5 mL) in an autoclave teflon container and stirred for 5 min. Then, 0.0196 g of 1,4-benzene dicarboxylic acid and 0.0092 g of 4,4′-bipyridine was added and stirred for 10 min. The container was tightly packed and kept at 95 °C for 24 h. Colourless block shaped crystals were collected and washed at least five times each with DMF and hexane and dried in air.

MOF-508a was characterised by powder X-ray diffraction (PXRD) recorded on a Bruker D8 Discover instrument using Cu-K_α radiation(40 kV, 30 mA). Thermogravimetric analysis (TGA) was performed using Mettler Toledo TGA 850 instrument in nitrogen atmosphere in the temperature range of 30 - 700 °C at a heating rate of 10 °C per min. Nitrogen and carbon dioxide adsorption isotherm was measured using Quantachrome Quadrasorb - SI analyzer.

Raman spectroscopic studies were recorded using a custom built Raman spectrometer with 1800 lines/ mm grating [35]. Typically, 532 nm Nd-YAG solid state laser and 632.8 nm HeNe gas lasers were used for the experiments, with a power of about 8 mW on the sample. Temperature dependent Raman studies were performed using a Linkam THMS 600 heating-cooling stage. MOF-508a was loaded on the Linkam stage and heated to 120 °C (at a rate of 10 °C per minute) to remove the solvent

molecules and activate the sample. The sample was cooled to RT. Further, at RT, CO_2 gas was purged following which the temperature was further lowered. All the gases used for adsorption and Raman studies were obtained from Chemixgases, India and had 99.999 % purity.

Pressure dependent Raman studies were conducted using a membrane type diamond anvil cell (MDAC) equipped with pneumatic drive system (PDS150 from BETSA, France) to manage the Helium gas pressure inside the membrane and thereby control the mechanical force on the diamond anvils. The diamond culet size was 400 microns. A pre-indented (up to 70 micron) stainless steel (T301) gasket with a hole of diameter 140 microns was used inside the cell to hold the sample. Pre-heated fine powder of NaCl is used as a pressure transmitting medium. Here, guest free form of MOF-508b crystals were loaded inside the gasket hole along with NaCl and a few ruby chips for pressure calibration. Pressure inside the cell is determined by ruby fluorescence technique [36].

5.3 Results and Discussions

The structure of MOF-508a was confirmed by powder X-ray diffraction (Figure 5.1) confirming the structure shown in Scheme 5.1 wherein BDC is ligated to Zn atoms forming the ab plane which are connected to each other through the BPY linker forming a 3D interpenetrated framework. TGA curve in Figure 5.2 shows that MOF-508a loses solvent molecules in the temperature regime 20-120 °C to form the second phase, MOF-508b [33]. Although, the connectivity is retained in the desolvated framework MOF-508b, the crystal is distorted due to deformation in the $Zn_2(COO)_4$ paddle wheel secondary building units and the BPY ligand [33].

N_2 and CO_2 adsorption isotherms measured at 77 K and 195 K respectively presented in Figure 5.3 shows type I Langmuir isotherm [32, 33]. The adsorption isotherms show step adsorption depicting guest induced dynamics in the framework. During

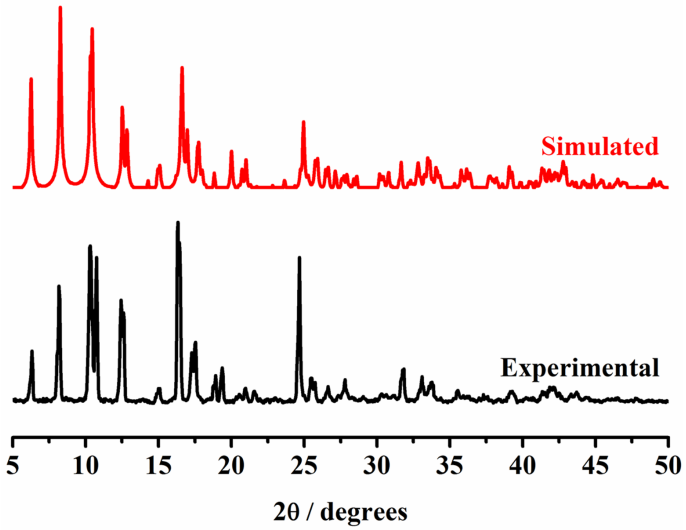

Figure 5.1: Powder X-ray diffraction pattern (black curve) and simulated pattern (red curve) of MOF-508a.

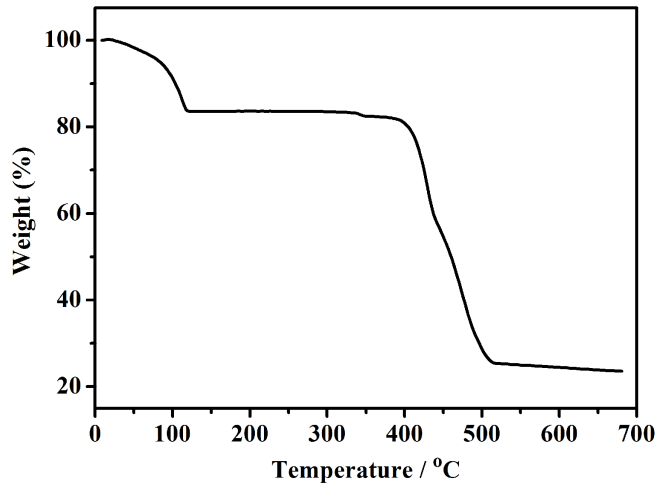

Figure 5.2: Thermogravimetric analysis of MOF-508a in nitrogen atmosphere.

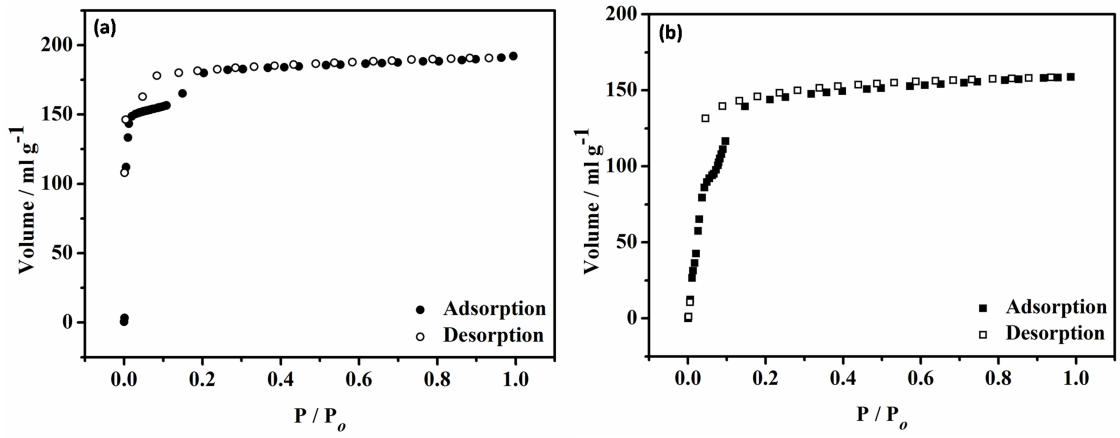

Figure 5.3: (a) Nitrogen and (b) carbon dixoide adsorption-desorption isotherm for MOF-508 at 77 K and 195 K respectively.

desorption, the guest molecules are retained in the MOF as revealed by the hysteresis in the isotherm. This guest induced dynamics has been investigated in detail in the following section by Raman spectroscopy.

5.3.1 Raman studies

The room temperature Raman spectrum of MOF-508a is presented in Figure 5.4 with the detailed band assignment in Table 5.1. The Raman spectrum has intense signatures of BDC and BPY in the fingerprint region. Surprisingly, all the C-H stretching frequencies of BPY and BDC are enveloped by a broad peak at 3077 cm^{-1} due to intermixing of the modes. On Lorentzian fitting, this broad peak could be resolved into three peaks at 3068, 3077 and 3084 cm^{-1}. The broadening of the peak could be due to the strong interaction of the hydrogens with the guest molecules or stronger coupling due to Davydov splitting explained later. Fingerprint region (1000-1500 cm^{-1}) peaks can be associated with C-C or C-H bending vibrations or the ring modes. Low frequency mode at 174 cm^{-1} can be associated either to the lattice vibrations or to the metal-ligand coordinate bond while the mode at 296 cm^{-1} is assigned to ring bending mode of BPY. Heating MOF-508a results in softening in

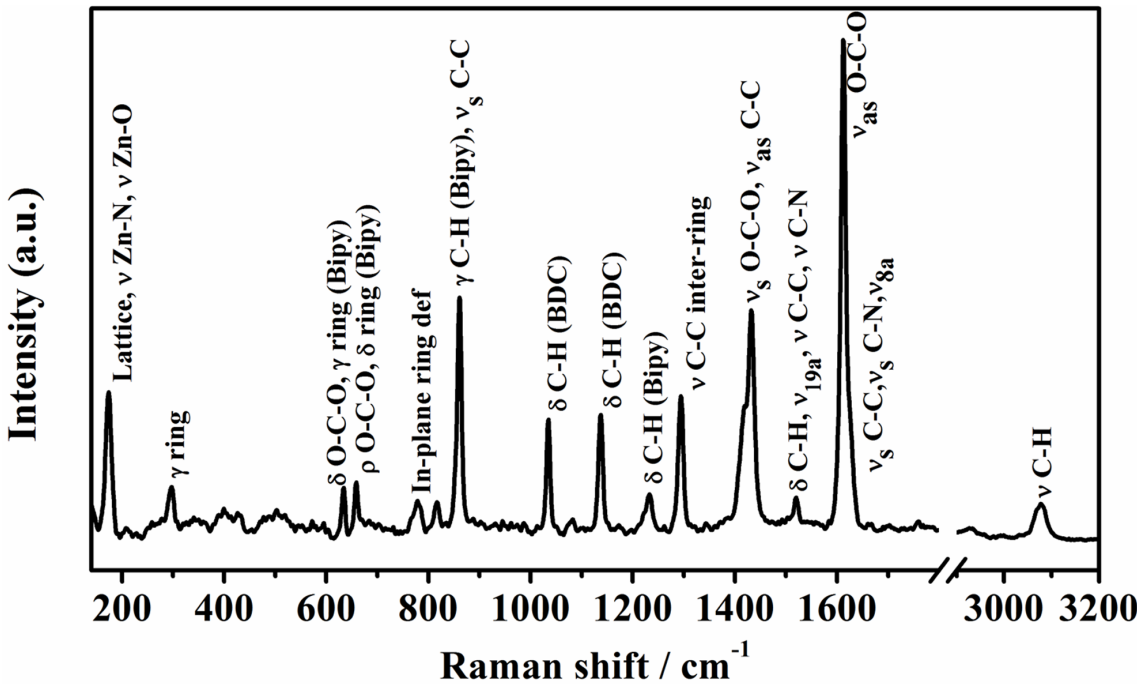

Figure 5.4: Room temperature Raman spectrum of MOF-508a.

Raman frequencies due to weakening of bond strengths as a consequence of increase in thermal fluctuations at high temperatures. Alternatively, at high temperatures, on removal of guest molecules, instead of broadened C-H stretching mode around 3080 cm^{-1}, we see well resolved and distinct peaks at 3052, 3062, 3066, 3080 and a very weak mode at 3099 cm^{-1}. This unusual splitting is similar to Davydov splitting which says that in the molecular crystals, vibrational or electronic bands splitting is observed when more than one molecule is present in unit cell and splitting results due to the coupling of the molecular dipole moments [43–45]. Depending on the coupling strength, the modes are either conjoined resulting into broad peaks observed in MOF-508a or well split as in MOF-508b. Since the two interpenetrating nets in MOF-508 are in close proximity, we believe that there could be coupling of the π-electron cloud in two nets resulting into Davydov splitting. As a result, the aromatic ring modes around 1610 cm^{-1} also shows a similar trend. In addition, a new mode at 249 cm^{-1} was also observed in the Raman spectrum of MOF-508b after activation at 120

Frequency (cm^{-1})	**Band assignment**
174	Lattice mode, ν Zn-N, ν Zn-O
296	γ ring bending
634	δ O-C-O, δ ring bending (BPY)
658	ρ O-C-O, δ ring def (BPY)
773	In plane ring def
782	In plane ring breathing
817	γ C-H (BPY)
861	γ C-H (BPY), ν_s C-C
1035	δ C-H (BDC), ring breathing, ring def
1082	δ C-H (BPY)
1137	δ C-H (BDC)
1221	δ C-H (BPY)
1232	δ C-H (BPY)
1294	ν C-C inter-ring
1417	ν_s O-C-O
1433	ν_s O-C-O, ν_{as} C-C
1520	δ C-H, ν_{19a}, ν C-C, ν C-N
1612	ν_{as} O-C-O
1626	ν_s C-C, ν_s C-N, ν_{8a}
1631	ν_s C-C, ν_s C-N, ν_{8a}
3068	ν C-H
3077	ν C-H
3084	ν C-H

* γ-out of plane bend; δ-in plane bend; ρ-rocking ;δ-bend; ν-stretch; s-symmetric; as-antisymmetric,

Table 5.1: Raman band assignment of MOF-508a [37–42].

°C (Figure 5.5, red curve). This mode was retained at room temperature and low temperatures upon cooling without the solvent molecule. Surprisingly, upon guest uptake (here DMF) this mode disappears (Figure 5.5, blue curve) and reappears upon further activation of the framework (Figure 5.5, pink curve) demonstrating structural reversibility and flexibility of the framework. In previous literatures on BPY, the mode at 262 cm^{-1} has been assigned to inter-ring out of plane bending vibration [37]. The bipyridine ring is present in two different orientations in MOF-508a and MOF-508b as revealed by the crystal structure (see Figure 5.5b) [33]. The two pyridine rings of BPY in MOF-508a are twisted with respect to the C-C inter

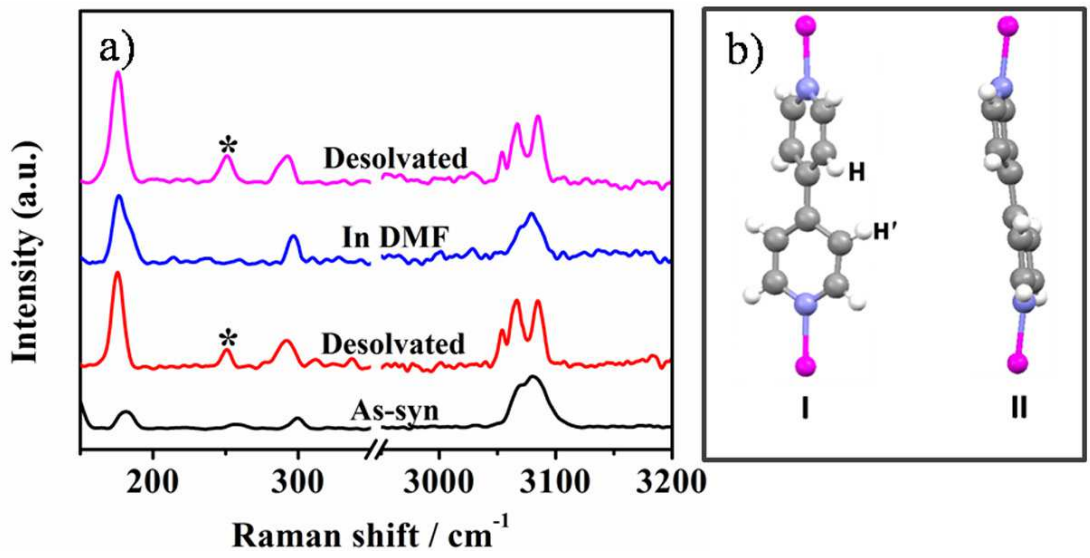

Figure 5.5: Raman spectra of MOF-508 in the low frequency and high frequency regime, a) Raman spectra of as-synthesized MOF-508a, desolvated MOF-508b, DMF sorbed MOF-508a and re-activated MOF-508b at RT (294 K) arranged from bottom to top. Star marks the appearance of new peak at 249 cm^{-1} corresponding to inter-ring out of plane bending mode of BPY, b) Con-formation of BPY in MOF-508a (I)and MOF-508b (II).

ring bond and is similar to the conformation of BPY in its ground state (Figure 5.5b, I). In MOF-508b, the two pyridine rings in BPY are nearly planar (Figure 5.5b, II) and can execute in-plane bending vibrations which can give rise to the 249 cm^{-1} mode. It must be mentioned here that the out of plane bending vibration of BPY also softens from 296 cm^{-1} in MOF-508a to 287 cm^{-1} in MOF-508b. The orientational change in BPY can be understood as a means to dispense repulsive interaction between the ortho-hydrogens, H and H′ (see Figure 5.5b) while allowing for the C-H$\cdots\pi$ and $\pi\cdots\pi$ interactions holding the framework. Besides, the conformational change induces conjugation between the two pyridine rings which compensates for the repulsive interaction between the ortho-hydrogens. Direct consequences of these interactions are observed as changes in the ring modes of BPY, and C-H stretching frequencies $\sim$3080 cm^{-1} which are found to be exceptionally sensitive to these phase transitions.

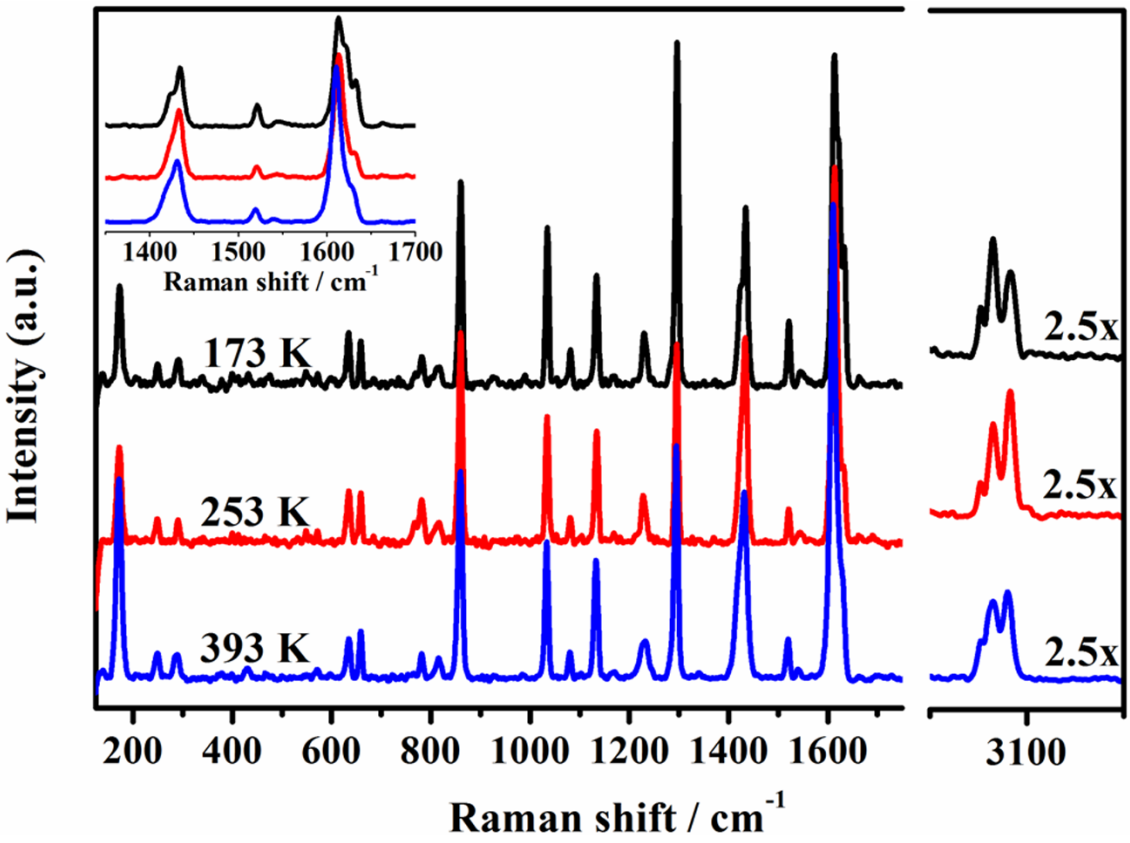

Figure 5.6: Temperature dependent Raman spectra of activated MOF-508b. Inset shows the zoomed-in spectra in the mid frequency range. High frequency regime ranging from 3000-3200 cm^{-1} is scaled by 2.5 times the original spectra to show the spectra features clearly.

5.3.2 Temperature dependent Raman studies

Raman spectra of activated MOF-508b in the temperature range 120 °C to -100 °C did not show any significant change (Figure 5.6). All the modes remained intact, however their relative intensities changed indicating slight structural re-orientation of BDC and BPY ligand with the temperature. Further, reduced full width at half maximum at low temperature results in resolution of modes at low temperature (Figure 5.6, inset). Hence, it can be concluded that the structure of MOF-508b is preserved in the low temperature regime as well.

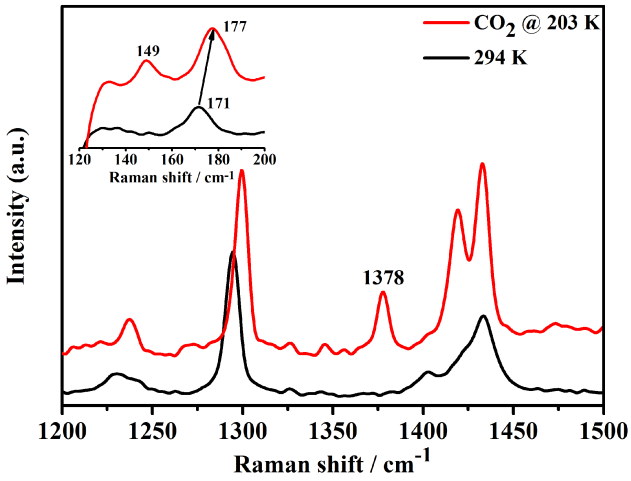

Figure 5.7: Raman spectra of MOF-508b at 294 K (black curve) and CO_2 adsorbed in MOF-508a at 203 K (red curve). Inset shows the appearance of librational mode of adsorbed carbon dioxide at 149 cm^{-1} and hardening of lattice mode of MOF-508 from 171 cm^{-1} to 177 cm^{-1}.

5.3.3 CO_2 adsorption in MOF-508b probed by Raman spectroscopy

CO_2 adsorption in MOF-508 is confirmed by the appearance of a new peak at 1378 cm^{-1} in the Raman spectrum (Figure 5.7). This mode corresponds to the ν^+ Fermi resonance mode of CO_2 which occurs at 1388 cm^{-1} for free CO_2 gaseous molecules. Softening of encaged CO_2 molecules in the framework has been attributed to strong interaction of the CO_2 molecules with the framework [46]. Further, CO_2 librational lattice mode at 149 cm^{-1} and hardening of the framework lattice mode from 171 cm^{-1} to 177 cm^{-1} (Figure 5.7, inset) was also observed. Appearance of CO_2 librational lattice mode indicates cooperative binding and has been ascribed to dispersion (quadrupole-π interaction) and electrostatic interactions between the CO_2 molecules [47]. Interestingly, on CO_2 adsorption the splitting in the C-H stretching frequencies ($\sim$3080 cm^{-1}) is reduced and the 249 cm^{-1} mode disappeared implying the transition from closed form MOF-508b to open form MOF-508a. To further

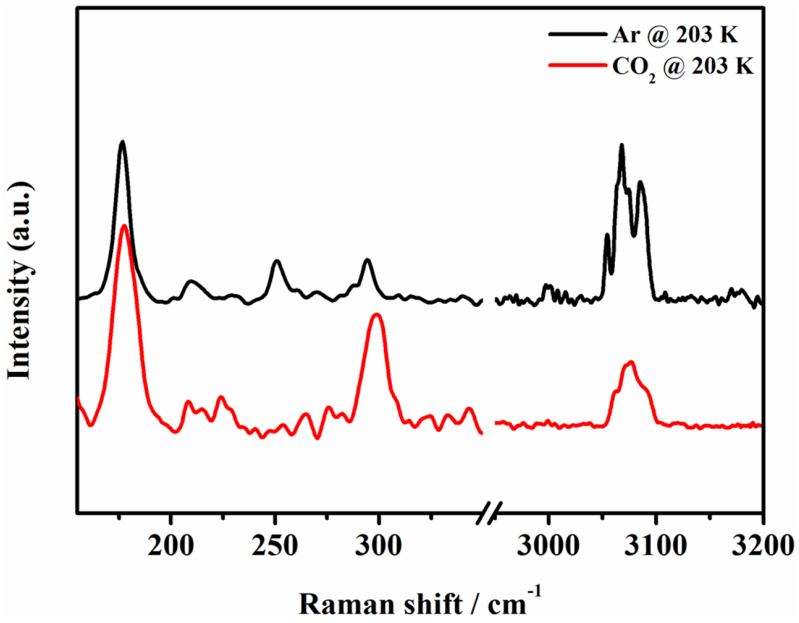

Figure 5.8: Raman spectra of MOF-508 in CO_2 (red curve) and Argon atmosphere (black curve) at 203 K.

validate the spectral changes, we have performed temperature dependent Raman studies in an inert Argon atmosphere and found that the C-H modes remained well split at -70 °C, the 249 cm^{-1} mode is retained and other modes are well preserved as shown in Figure 5.8.

5.3.4 Pressure effects on MOF-508

Pressure is a stronger and cleaner source of perturbation to probe phase transitions as compared to temperature. In pressure experiments, we only change volume. Considering the structural change from MOF-508a to MOF-508b is driven by the rearrangement of BPY rings, we expect that by applying pressure we should be able to take MOF-508b to MOF-508a similar to introducing the guest molecules. Pressure has been employed to instigate structural transitions in MOFs such as MOF-5 and ZIF-8 [48–50]. It was shown that MOF-5 amorphizes at 3.5 MPa whereas ZIF-8 can sustain pressure in the gigapascal regime. MOF-508b is an interpenetrating

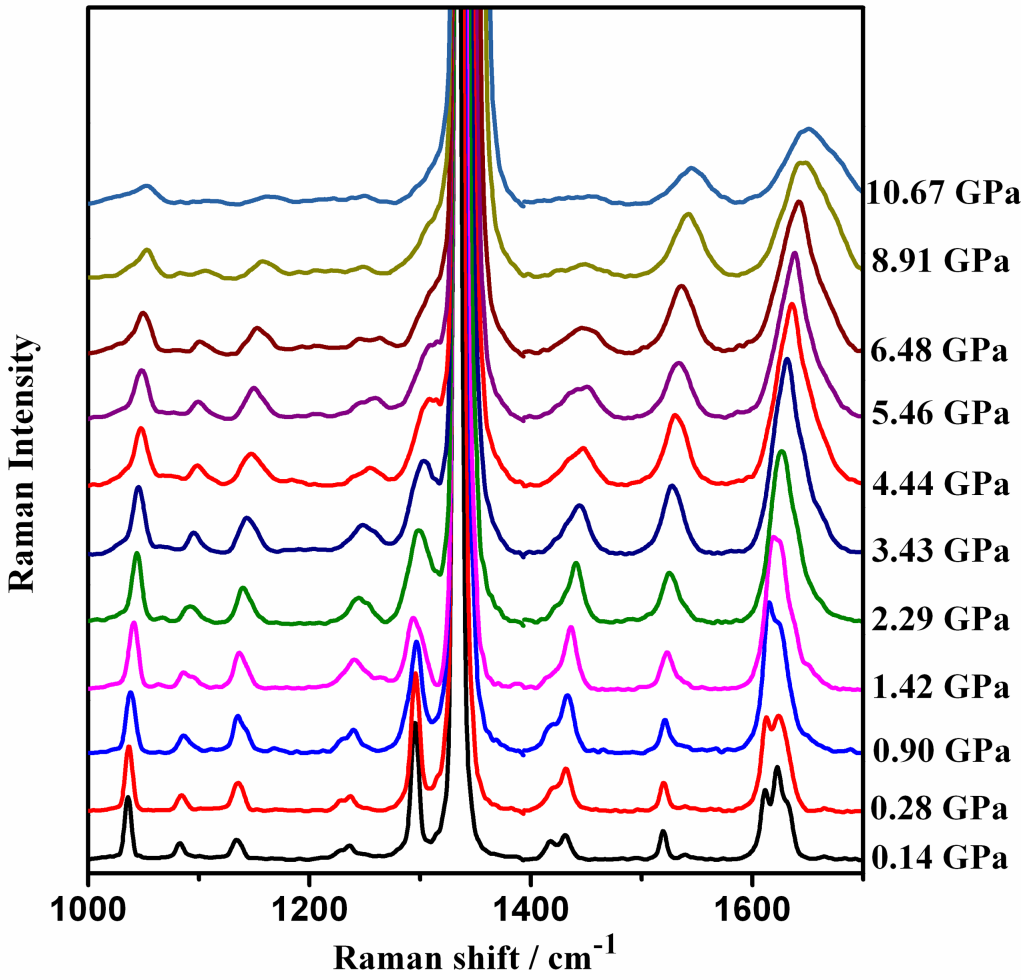

Figure 5.9: Pressure dependent Raman spectra of desolvated MOF-508b recorded at ambient temperature.

framework and has many void spaces. So, on application of pressure it can slide over each other to withstand the applied pressure. To investigate this transformation we conducted pressure dependent Raman studies on MOF-508b.

Activated MOF-508b and ruby crystals were loaded in the diamond anvil cell (DAC) along with NaCl which acts as the pressure transmitting medium. NaCl does not interact with the sample and remains hydrostatic till 7 GPa. Ruby fluorescence was used to measure pressure. Pressure dependent Raman spectra of MOF-508b is shown in Figure 5.9. The framework was stable in the DAC as revealed by its spectral signature. It is known that the orientation of linkers, nature of bonding and anharmonicity of the modes are affected on increasing pressure [51]. To quantify this change, frequency versus pressure plot has been shown in Figure 5.10. Most of the modes exhibit an abrupt frequency change in the 1.5-2 GPa pressure regime. Contrary to normal pressure behaviour, few of the modes start softening as the pressure is increased and subsequently begin to harden beyond 2 GPa (see Figure 5.10a and b). Further, we also observe a new mode at 898 cm^{-1} at 2 GPa (Figure 5.10c). This mode was present in room temperature spectra of MOF-508b but had disappeared once it was put in the DAC. Apparently, the modes undergoing sharp changes are associated with BPY ring modes and O-C-O bending mode in BDC. Assuming MOF-508b distorts under pressure to form MOF-508a implies that the angle between the a and b plane containing the BDC increases. This would relax the O-C-O bending vibration resulting in softening of modes as observed in Figure 5.10a and b. In addition, the ring modes of BPY $\sim$ 1600 cm^{-1} starts coalescing into each other as shown in Figure 5.9, resembling the peak feature of MOF-508a demonstrating that under pressure, BPY converts from structure II to structure I (Figure 5.5b) due to shear stress. This conversion would facilitate sliding of the framework to retain framework stability under pressure. Earlier reports on biphenyls and bipyridines also show that the two pyridine rings in BPY can twist around the

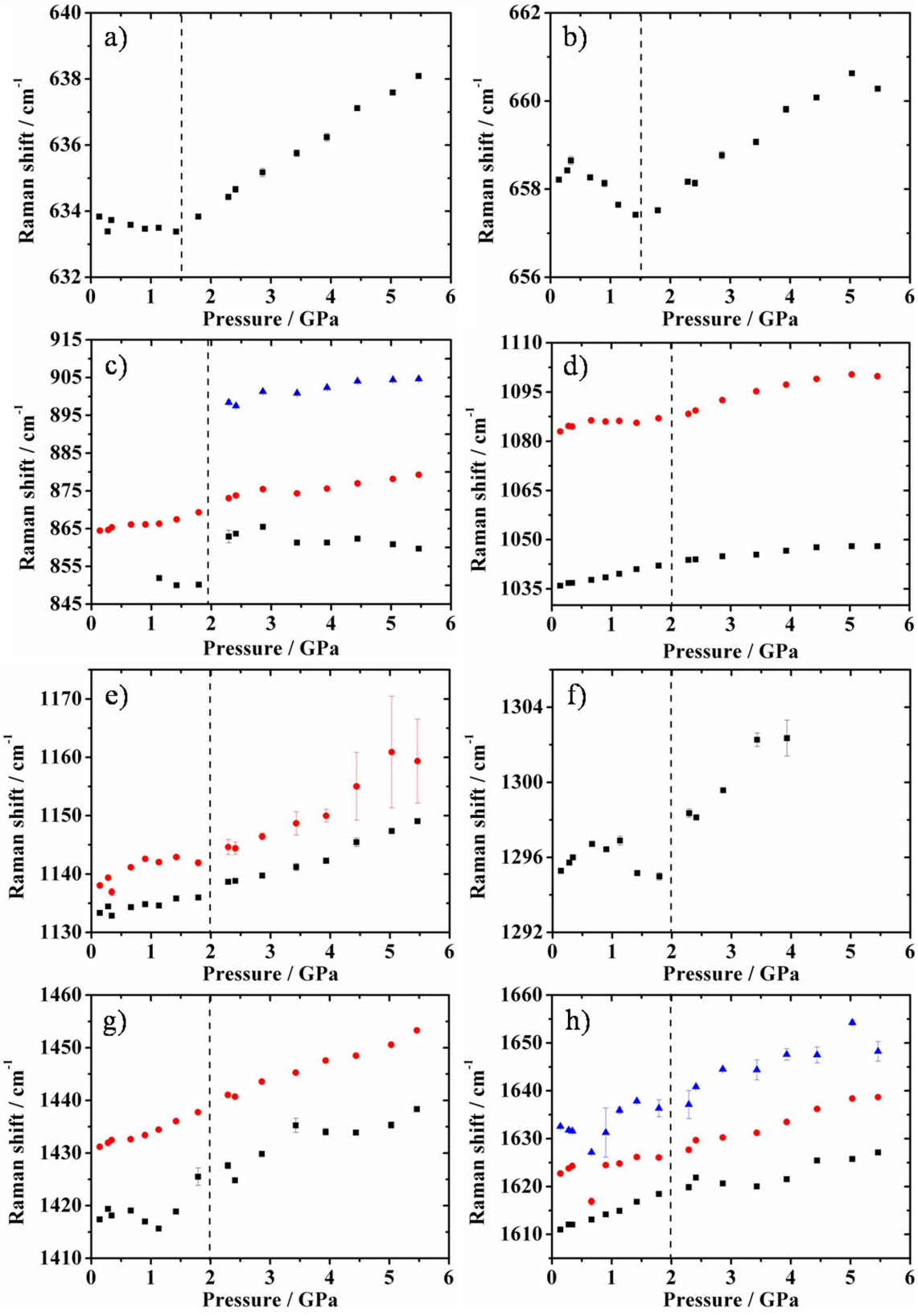

Figure 5.10: Frequency versus pressure plot of a) δ O-C-O (BDC), b) ρ O-C-O (BDC), c) γ C-H bending (BPY), d) δ C-H bending of BDC (1035 cm^{-1}) and BPY (1082 cm^{-1}), e) δ C-H bending of BDC, f) inter-ring C-C stretch of BPY, g) ν_s O-C-O, h) ν_{as} O-C-O 1612 cm^{-1}, ν_s C-C at 1626 and 1631 cm^{-1} respectively.

inter-ring C-C bond under high pressure or temperature [37, 52]. Secondly, O-C-O symmetric stretch ∼1417 and 1433 cm^{-1} in MOF-508b are merged together at atmospheric pressure whereas it splits once MOF-508b crystals are put in the pressure cell suggesting a transition in the BDC linker as well. These spectral transitions indicate that pressurizing guest free phase MOF-508b would favour a phase isomorphic to MOF-508a. This transition persists up to 1.5-2 GPa pressures. At pressures above 2GPa, the unit cell contraction occurs which result in hardening and broadening of all the modes, which is a normal pressure behaviour.

5.4 Conclusions

A comprehensive study of MOF-508 under variable conditions of temperature, pressure and gas adsorption was performed by Raman Spectroscopy. Change in the vibrational modes of the framework suggests change in conformation of 4,4′-bipyridine and 1,4-benzene dicarboxylic acid ligand with external stimuli. In particular, C-H stretching frequencies provide vital information on structural transformations in MOF-508 at low temperature, high pressure or guest uptake. Further, CO_2 uptake was confirmed by its Fermi resonance peak at 1378 cm^{-1}. Appearance of low frequency librational mode at 149 cm^{-1} at low temperature implies co-operative adsorption mechanism of CO_2 in the framework.

Pressurizing de-solvated MOF-508b in diamond anvil cell results in structural transition from MOF-508b to MOF-508a as revealed from the spectra features at 1.5 to 2 GPa. The later phase is stable at high pressures upto 6 GPa.

Bibliography

[1] J. A. Mason, M. Veenstra, and J. R. Long, *Evaluating metal–organic frameworks for natural gas storage*, Chemical Science **5**, 32 (2014).

[2] O. K. Farha *et al.*, *De novo synthesis of a metal–organic framework material featuring ultrahigh surface area and gas storage capacities*, Nature Chemistry **2**, 944 (2010).

[3] B. Li, H. Wang, and B. Chen, *Microporous Metal–Organic Frameworks for Gas Separation*, Chemistry–An Asian Journal **9**, 1474 (2014).

[4] T.-H. Bae *et al.*, *A High-Performance Gas-Separation Membrane Containing Submicrometer-Sized Metal–Organic Framework Crystals*, Angewandte Chemie International Edition **49**, 9863 (2010).

[5] D. Farrusseng, S. Aguado, and C. Pinel, *Metal–organic frameworks: opportunities for catalysis*, Angewandte Chemie International Edition **48**, 7502 (2009).

[6] F. X. L. i Xamena, A. Abad, A. Corma, and H. Garcia, *MOFs as catalysts: activity, reusability and shape-selectivity of a Pd-containing MOF*, Journal of Catalysis **250**, 294 (2007).

[7] P. G. Yot *et al.*, *Large breathing of the MOF MIL-47(V^{IV}) under mechanical pressure: a joint experimental–modelling exploration*, Chemical Science **3**, 1100 (2012).

[8] F.-X. Coudert, A. Boutin, A. H. Fuchs, and A. V. Neimark, *Adsorption deformation and structural transitions in metal–organic frameworks: From the unit cell to the crystal*, The Journal of Physical Chemistry Letters **4**, 3198 (2013).

[9] J.-R. Li, R. J. Kuppler, and H.-C. Zhou, *Selective gas adsorption and separation in metal–organic frameworks*, Chemical Society Reviews **38**, 1477 (2009).

[10] A. A. Talin *et al.*, *Tunable Electrical Conductivity in Metal-Organic Framework Thin-Film Devices*, Science **343**, 66 (2014).

[11] G.-l. Zhuang *et al.*, *Synthesis, properties, and magnetism–structure relationship of lanthanide-based metal–organic frameworks with (ethylenedithio) acetic acid*, CrystEngComm **16**, 6963 (2014).

[12] B.-Q. Song *et al.*, *A polyrotaxane-like metal-organic framework exhibiting luminescent sensing of Eu^{3+} cations and proton conductivity*, CrystEngComm **16**, 6882 (2014).

[13] R. Haldar *et al.*, *Amine-Responsive Adaptable Nanospaces: Fluorescent Porous Coordination Polymer for Molecular Recognition*, Angewandte Chemie International Edition **53**, 11772 (2014).

[14] V. M. Suresh *et al.*, *Oligo (p-phenyleneethynylene)-Derived Porous Luminescent Nanoscale Coordination Polymer of Gd^{III}: Bimodal Imaging and Nitroaromatic Sensing*, The Journal of Physical Chemistry C **118**, 12241 (2014).

[15] A. Chakraborty, R. Haldar, and T. K. Maji, *Bifunctional Co(II)–Ag(I) and Ni(II)–Ag(I) Frameworks: Modulation of Magnetic Property and CO_2 Uptake Based on Organic Pillars*, Crystal Growth & Design **13**, 4968 (2013).

[16] S. Horike, S. Shimomura, and S. Kitagawa, *Soft porous crystals*, Nature chemistry **1**, 695 (2009).

[17] S. Sanda, S. Parshamoni, and S. Konar, *Third-generation breathing metal–organic framework with selective, stepwise, reversible, and hysteretic adsorption properties*, Inorganic chemistry **52**, 12866 (2013).

[18] P. Horcajada *et al.*, *Flexible porous metal-organic frameworks for a controlled drug delivery*, Journal of the American Chemical Society **130**, 6774 (2008).

[19] Q. Ma *et al.*, *Guest-modulation of the mechanical properties of flexible porous metal–organic frameworks*, Journal of Materials Chemistry A **2**, 9691 (2014).

[20] J. Seo *et al.*, *Soft secondary building unit: dynamic bond rearrangement on multinuclear core of porous coordination polymers in gas media*, Journal of the American Chemical Society **133**, 9005 (2011).

[21] S. B. Choi *et al.*, *Reversible Interpenetration in a Metal–Organic Framework Triggered by Ligand Removal and Addition*, Angewandte Chemie International Edition **51**, 8791 (2012).

[22] G. Kumari, K. Jayaramulu, T. K. Maji, and C. Narayana, *Temperature Induced Structural Transformations and Gas Adsorption in the Zeolitic Imidazolate Framework ZIF-8: A Raman Study*, The Journal of Physical Chemistry A **117**, 11006 (2013).

[23] S. A. Moggach, T. D. Bennett, and A. K. Cheetham, *The Effect of Pressure on ZIF-8: Increasing Pore Size with Pressure and the Formation of a High-Pressure Phase at 1.47 GPa*, Angewandte Chemie International Edition **48**, 7087 (2009).

[24] P. Kanoo *et al.*, *Unusual room temperature CO_2 uptake in a fluoro-functionalized MOF: insight from Raman spectroscopy and theoretical studies*, Chemical Communications **48**, 8487 (2012).

[25] V. Bon *et al.*, *In Situ Observation of Gating Phenomena in the Flexible Porous Coordination Polymer $Zn_2(BPnDC)_2(bpy)$(SNU-9) in a Combined Diffraction and Gas Adsorption Experiment*, Inorganic chemistry **53**, 1513 (2014).

[26] C. Prestipino *et al.*, *Local structure of framework Cu(II) in HKUST-1 metallorganic framework: spectroscopic characterization upon activation and interaction with adsorbates*, Chemistry of materials **18**, 1337 (2006).

[27] F. Bonino *et al.*, *Local structure of CPO-27-Ni metallorganic framework upon dehydration and coordination of NO*, Chemistry of Materials **20**, 4957 (2008).

[28] M. Maczka, M. Ptak, and L. Macalik, *Infrared and Raman studies of phase transitions in metal–organic frameworks of $[(CH_3)_2NH_2][M(HCOO)_3]$ with M= Zn, Fe*, Vibrational Spectroscopy **71**, 98 (2014).

[29] N. Nijem *et al.*, *Understanding the preferential adsorption of CO_2 over N_2 in a flexible metal–organic framework*, Journal of the American Chemical Society **133**, 12849 (2011).

[30] N. Nijem *et al.*, *Spectroscopic characterization of van der Waals interactions in a metal organic framework with unsaturated metal centers: MOF-74–Mg*, Journal of Physics: Condensed Matter **24**, 424203 (2012).

[31] D. Y. Siberio-Pérez, A. G. Wong-Foy, O. M. Yaghi, and A. J. Matzger, *Raman spectroscopic investigation of CH_4 and N_2 adsorption in metal-organic frameworks*, Chemistry of materials **19**, 3681 (2007).

[32] B.-Q. Ma, K. L. Mulfort, and J. T. Hupp, *Microporous pillared paddle-wheel frameworks based on mixed-ligand coordination of zinc ions*, Inorganic chemistry **44**, 4912 (2005).

[33] B. Chen *et al.*, *A Microporous Metal-Organic Framework for Gas-Chromatographic Separation of Alkanes*, Angewandte Chemie International Edition **45**, 1390 (2006).

[34] T. K. Maji, R. Matsuda, and S. Kitagawa, *A flexible interpenetrating coordination framework with a bimodal porous functionality*, Nature materials **6**, 142 (2007).

[35] G. P. Kumar and C. Narayana, *Adapting a fluorescence microscope to perform surface enhanced*, Current science **93**, 778 (2007).

[36] H. Mao, P. Bell, J. t. Shaner, and D. Steinberg, *Specific volume measurements*

of Cu, Mo, Pd, and Ag and calibration of the ruby R1 fluorescence pressure gauge from 0.06 to 1 Mbar, Journal of applied physics **49**, 3276 (1978).

[37] L. Ould-Moussa *et al.*, *Ab Initio computations of the geometrical, electronic, and vibrational properties of the ground state, the anion radical, and the N,N'-dihydro cation radical of 4,4'-bipyridine compared to transient Raman spectra*, The Journal of Physical Chemistry **100**, 2072 (1996).

[38] E. Kassab and M. Castellà-Ventura, *Theoretical study of pyridine and 4,4'-bipyridine adsorption on the lewis acid sites of alumina surfaces based on ab initio and density functional cluster calculations*, The Journal of Physical Chemistry B **109**, 13716 (2005).

[39] A. Moissette, Y. Batonneau, and C. Brémard, *Conformation and protonation of 2,2'-bipyridine and 4,4'-bipyridine in acidic aqueous media and acidic ZSM-5 zeolites: A Raman scattering study*, Journal of the American Chemical Society **123**, 12325 (2001).

[40] E. Hollauer *et al.*, *Fourier transform infrared and Raman spectra, vibrational assignment and ab initio calculations of terephthalic acid and related compounds*, Spectrochimica Acta Part A: Molecular and Biomolecular Spectroscopy **57**, 993 (2001).

[41] J. M. Bello, D. L. Stokes, and V. D. Tuan, *Direct characterization of phthalic acid isomers in mixtures using surface-enhanced Raman scattering*, Analytical Chemistry **62**, 1349 (1990).

[42] B. Civalleri *et al.*, *Ab-initio prediction of materials properties with CRYSTAL: MOF-5 as a case study*, CrystEngComm **8**, 364 (2006).

[43] X. Wang *et al.*, *Topography-Correlated Confocal Raman Microscopy with Cylindrical Vector Beams for Probing Nanoscale Structural Order*, The Journal of Physical Chemistry Letters **5**, 1048 (2014).

[44] A. S. Davydov, in *Theory of molecular excitons* (Springer, , 1971).

[45] T. Breuer *et al.*, *Vibrational Davydov Splittings and Collective Mode Polarizations in Oriented Organic Semiconductor Crystals*, The Journal of Physical Chemistry C **116**, 14491 (2012).

[46] Y. Yao *et al.*, *Analyzing the frequency shift of physiadsorbed CO_2 in metal organic framework materials*, Physical Review B **85**, 064302 (2012).

[47] R. Vaidhyanathan *et al.*, *Direct observation and quantification of CO_2 binding within an amine-functionalized nanoporous solid*, Science **330**, 650 (2010).

[48] I. Beurroies *et al.*, *Using pressure to provoke the structural transition of metal–organic frameworks*, Angewandte Chemie International Edition **49**, 7526 (2010).

[49] Y. H. Hu and L. Zhang, *Amorphization of metal-organic framework MOF-5 at unusually low applied pressure*, Physical Review B **81**, 174103 (2010).

[50] Y. Hu *et al.*, *In situ high pressure study of ZIF-8 by FTIR spectroscopy*, Chem. Commun. **47**, 12694 (2011).

[51] P. Wong, *Pressure and temperature dependences of the Raman-active phonons in dichlorobis(pyridine)zinc(II) crystal*, The Journal of Chemical Physics **63**, 5108 (1975).

[52] G. Zerbi and S. Sandroni, *Fundamental frequencies and molecular configuration of biphenyl—I. Re-analysis of its vibrational spectrum*, Spectrochimica Acta Part A: Molecular Spectroscopy **24**, 483 (1968).

Part II

Surface enhanced Raman scattering and plasmonics

Chapter 6

Can We Probe Large Molecules by SERS?

6.1 Introduction

SERS is the enhancement of Raman signal of molecules present in the vicinity of intense electric field created near a plasmonic nanostructure excited by electromagnetic radiation. The enhancement is either due to increased number of photons being scattered by the molecule attributed to higher electric field in the proximity of the nanoparticles (electromagnetic enhancement) and/or due to charge transfer between the molecule and the metal nanoparticles leading to redistribution of molecular energy levels across the Fermi level (chemical enhancement) [1–4]. Since its inception, there have been numerous works on developing metal nanostructures [5–8] yielding consistently high SERS enhancement factor rendering them widely applicable for studying chemical dynamics [9], single molecule detection [10–12], single molecule dynamics [13], DNA detection [14], investigating conformational changes in protein [15, 16], glucose sensing and many more [17]. The proximity of the analyte to the nanoparticle surface plays a predominant role in all the applications. It

is believed that SERS can be effectively obtained from molecules lying within 1 nm of nanoparticle surface since the electric field intensity drops by a factor of $1/d^{12}$ with distance 'd' [18]. This would substantially affect the SERS signal from larger systems (size $>$ 1 nm) such as proteins and other macro-molecules.

Intense electric field near nanoparticles is due to the excitation of surface plasmons. Free electrons in conduction band of metal nanoparticles can be collectively excited and are confined within the nanoparticle. Once excited, the surface plasmons can decay either radiatively or non-radiatively. Theoretical modeling shows that 20 nm gold nanoparticles are weak scatterers as the surface plasmon damping is mainly governed by energy dissipation via non-radiative processes like electron-electron, electron-phonon or electron-defect scattering processes while larger gold nanoparticles are strong scatterers as plasmon damping is mainly via radiative process [19–21]. This means that smaller nanoparticles are weak SERS enhancers in comparison to the larger nanoparticles. It has been shown experimentally that the enhancement factor increases as the nanoparticle size is increased up to a certain limit and thereafter starts decreasing [22–24]. The electric dipole field decays as $1/\mathrm{d}^3$, and the plasmonic field decays even more rapidly as $1/\mathrm{d}^{12}$, meaning that there will be no SERS enhancement at large distances. The dipolar field is directly proportional to the size of the nanoparticles and the concentration of surface free electrons. Hence, to increase the electric field surrounding the nanoparticles, we can increase the size of the nanoparticle and/or increase the charge q by choosing a metal with higher surface free electrons. This implies that the size of nanoparticles plays a vital role in controlling far field enhancement. Recently, nanostructures with 1 nm interior gap have been shown to yield high SERS enhancement factors by Lim *et al.* [25]. Further, modulating inter-particle gap in hybrid nanostructures to achieve higher Raman signal have also been reported. Li *et al.* showed SERS signal decay up to a distance of 20 nm in SHINERS particles [26, 27], while Qin *et al.* showed highest

SERS signal in 30 nm gap between 120 nm nanodisks [28]. Shanthil *et al.* also showed that the enhancement was higher when the separation between 60 nm silver dimer particles are less than 15 nm [29]. While most of the distance dependent SERS studies are based on single particle size, the result cannot be extrapolated to particles of either smaller or larger sizes. Secondly, these studies were performed on film or planar substrates. The results may differ from those of colloids in the solution which are primarily employed to study bio-molecules wherein charge neutralization and nanoparticle aggregation play a crucial role.

The subject of distant SERS enhancement in colloidal metal nanoparticles of different sizes is still unexplored. In this work we have investigated the role of size of nanoparticles on distance dependence of SERS. Noble metals like copper, silver and gold are among the best SERS enhancers in the visible region known so far. Among them, silver is the most efficient material as the real part of its dielectric constant is close to -2 in near UV while its imaginary part is small making it the most competent material for surface plasmon excitation as well as SERS [30]. So, we have chosen silver nanoparticles for the present studies. Silver nanoparticles in the size regime of 20-100 nm were synthesized by seed mediated growth. This approach yields homogenous nanoparticles which are of utmost importance for this study. For distance dependent studies, each nanoparticle was coated by thin silica shell of varying thickness. Silica shell prevents direct contact between the analyte molecule and the nanoparticle, thus ensuring enhancement only by electromagnetic mechanism. This is also important when we are using silver nanoparticle for SERS as: a) silver's antibacterial properties could make it difficult for in vivo studies of biological samples when used as bare nanoparticles, and b) effect of nanoparticles on the analyte properties, namely, proteins is avoided. The challenge in such a study was preparing controlled SiO_2 coating on nanoparticles, especially, coatings of less than 5 nm for bigger nanoparticles. Finally, SERS signal of rhodamine 6G (R6G)

was used to evaluate the distance dependence of the nanoparticles.

6.2 Experimental section

Chemicals. $HAuCl_4$ (Spectrochem, India), sodium citrate (Sigma-Aldrich), silver nitrate (Sigma-Aldrich), ascorbic acid (Rankem), 3-aminopropyl-triethoxysilane (APTES, Merck), 3-aminopropyl-trimethoxysilane (APTMS, Sigma-Aldrich), ethanol (Commercial Alcohols, AR), sodium silicate (27 % in water, Sigma-Aldrich), sodium hydroxide (Merck), orthophosphoric acid (S D Fine-Chem Limited), hydrochloric acid (S D Fine-Chem Limited). For all the synthesis milli Q water was used and the glasswares were thoroughly washed before use.

Active silica [31]. 72 μL of 27 % sodium silicate was added to 3.528 mL of water in a beaker. In another beaker, 0.6 g of NaOH was added to 5 mL water. The two solutions were mixed to form active silica.

Sodium silicate solution (for Ag75) [26]. 200 μL of sodium silicate solution was added to 2 ml water. To this, 6 mL of 0.01 M HCl solution was added with rapid stirring. Further, 1.8 mL of water was added to make 0.54 % solution of sodium silicate with a pH of 10. The solution was freshly prepared before use.

Sodium silicate solution (for Ag90) [26]. 30 μL of orthophosphoric acid was added to 20 mL water in a beaker to make 22 mM solution. In another beaker 500 μL of sodium silicate was added to 5 mL water. 15 mL of 22 mM orthophosphoric acid solution was added to sodium silicate solution. The solution was freshly prepared before use.

Synthesis of gold seed by Lee-Meisel method. Gold nanoparticles of size 12 nm were prepared via Lee-Meisel method [32] Briefly, 48 mg of $HAuCl_4$ was added to 100 ml of water and brought to boiling. 10 ml of 1 % sodium citrate was added and the solution was further boiled for 1 hr.

Growth of silver over gold seed. To obtain silver nanoparticles of uniform size, seed

mediated growth approach reported for by Uzayisenga *et al.* was adopted [33]. The synthesis protocol was further optimised to obtain even bigger silver nanoparticles by varying the ratio of Au seed to silver salt. Briefly, gold nanoparticle solution was diluted with milli Q water followed by addition of sodium citrate (1 % solution in water) and ascorbic acid (10 mM) as given in the Table 6.1. The mixture was stirred for 5 min after which silver nitrate (10 mM in water) solution was added drop wise and aged at 100 °C for 2 hrs.

Milli Q water	Au seed	Sodium citrate	Ascorbic acid	Silver nitrate	Au@Ag size
80 mL	4 mL	4 mL	12 mL	1.88 mL	Ag20
80 mL	2.8 mL	4 mL	12 mL	2.8 mL	Ag30
80 mL	2 mL	4 mL	12 mL	9.6 mL	Ag45
20 mL	0.5 mL	1 mL	3 mL	5 mL	Ag75
20 mL	0.4 mL	1 mL	3 mL	10 mL	Ag90

Table 6.1: Volume and concentration of reagents for synthesis of Au@Ag nanoparticles of different sizes.

Thin silica coating. The silica coating procedures reported in literature can be categorized into two categories. First one is based on Stober's method which describes the coating using tetraethylorthosilicate (TEOS) in ethanol or propanol-water mixture. The second synthesis was developed by Liz-Marzàn and Paul Mulvaney using sodium silicate solution [31, 34]. Apparently, the Stober's method can be best applied for thick silica coating of tens of nanometeres of silica, while the second method is suitable for thin layer silica coating of few nanometers. Since, our interests lay in thin layer silica coating, we followed the approach given by Liz-Marzàn and Paul Mulvaney [31, 34]. We have used a modified protocol to coat thin layer silica on Au@Ag based on earlier reports [26, 31]. Slightly different procedures were used for different size of Au@Ag nanoparticles as described below.

Ag20@SiO$_2$: 5 mL of Ag20 was added to 5 mL water and stirred. 20 μL of 2 mM APTES (in ethanol) was added and stirred for 15 min, followed by addition of 20

μL of active silica. The solution was left undisturbed for 2 hrs after which they were centrifuged and redispersed in milli Q water. In order to get different silica coating thickness, amount of active silica and the time for silica condensation was varied (see Table 6.2).

Au@Ag np	MilliQ water	APTES	Active silica	Nanoparticle name
Ag20 (5 mL)	5 mL	20 μL	20 μL	Ag20@SiO_2_1
Ag30 (5 mL)	5 mL	10 μL	10 μL	Ag30@SiO_2_1
Ag30 (5 mL)	5 mL	10 μL	20 μL	Ag30@SiO_2_2
Ag45 (5 mL)	5 mL	20 μL	40 μL	Ag45@SiO_2_1
Ag45 (5 mL)	5 mL	40 μL	40 μL	Ag20@SiO_2_2

Table 6.2: Volume and concentration of reagents for silica coating on 20 nm, 30 nm, 45 nm Au@Ag nanoparticles.

Ag30@SiO_2: 5 mL of Ag30 was added to 5 mL of water and stirred. 10 μL of 2 mM APTES (in ethanol) was added and stirred for 15 min. Then, active silica solution was added and the solution was left undisturbed for 2 hrs. Further, the nanoparticles were centrifuged and redispersed in milli Q water. Similar procedure was followed for Ag45 nanoparticles. See Table 6.2 for experimental details.

Ag75@SiO_2 and Ag90@SiO_2: Silver nanoparticles were functionalised with 1 mM APTES solution. Then, 0.54 % sodium silicate solution was added and heated at 90 °C. After heating for specified time given in Table 6.3 and Table 6.4 the reaction was quenched by transferring the solution in 1.5 mL centrifuge tube and putting in ice bath. After 30 min, the solutions were centrifuged, washed with water once and redispersed in milli Q water. The silica coated nanoparticles were stored in fridge at 4 °C.

Finite difference time domain (FDTD) simulation details. FDTD calculations were

Au@Ag np	APTMS	Sodium silicate	Heated at 90 °C for	Nanoparticle name
Ag75 (6 mL)	80 μL	640 μL	20 min	Ag75@SiO_2_1
Ag75 (6 mL)	80 μL	640 μL	40 min	Ag75@SiO_2_2
Ag75 (6 mL)	80 μL	640 μL	60 min	Ag75@SiO_2_3

Table 6.3: Volume and concentration of reagents for silica coating on 75 nm Au@Ag nanoparticles.

Au@Ag np	Milli Q water	APTES	Sodium silicate	Heated at 90 °C for	Nanoparticle name
Ag90 (5 mL)	5 mL	160 μL	330 μL	20 min	Ag90@SiO_2_1
Ag90 (5 mL)	5 mL	160 μL	1 mL	30 min	Ag90@SiO_2_2
Ag90 (5 mL)	5 mL	160 μL	1 mL	60 min	Ag90@SiO_2_3

Table 6.4: Volume and concentration of reagents for silica coating on 90 nm Au@Ag nanoparticles.

carried out using FDTD solutions from Lumerical solutions (FDTD Solutions, Lumerical Solutions, Inc., Vancouver, Canada). The simulation was performed in the following way. A circle was drawn. The material was chosen as Palik (0-2 μ) silver. A circular ring of desired thickness was drawn around the silver circle to form the silica shell. The dimension of FDTD simulation region was selected as 800 nm $\times$ 800 nm. The dimension of simulation mesh was around four times the radius of nanoparticles. The mesh override region was set to 0.25 nm for Ag20 and Ag30 nanoparticles while it was 0.5 nm for Ag45, Ag75 and Ag90 nanoparticles. The mesh accuracy was set to 4 in order to get more accurate results. Total field scattered field (TFSF) consisting of plane waves of 532 nm wavelength was incident from y-direction on the nanoparticles. Perfectly matched layer (PML) boundary was selected as they absorb the light incident on them. A frequency domain field-profile monitor was inserted to calculate the near field intensity around the nanoparticles. The simulation was run for 400 fs. All the simulations were performed with air (n=1) as the surrounding medium.

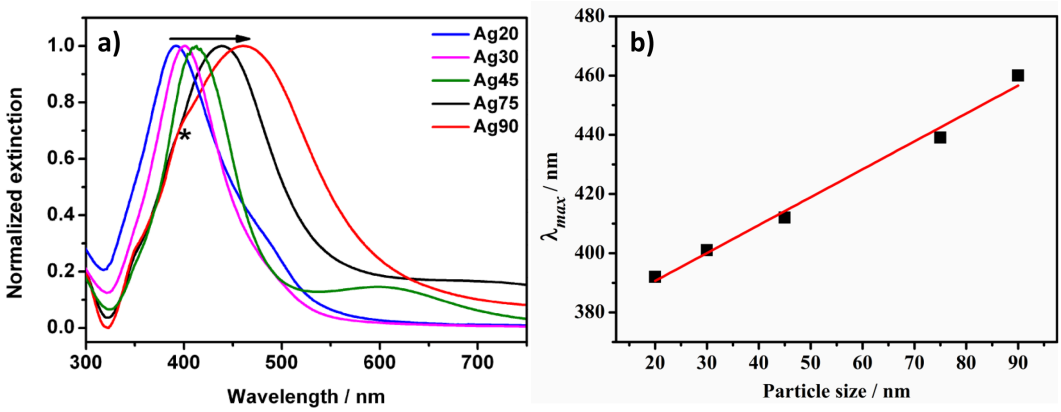

Figure 6.1: (a)Extinction spectra of silver nanoparticles of size 20 nm (blue), 30 nm (pink), 45 nm (green), 75 nm (black) and 90 nm (red), and (b) dependence of surface plasmon resonance on the particle size. Star shows the appearance of quadrupole mode in larger nanoparticles (Ag75 and Ag90).

Characterisation. The nanoparticles were characterized by UV-visible spectroscopy and transmission electron microscopy. UV-visible spectra of dilute solutions of nanoparticle were recorded in a 1 cm quartz cell using a Perkin-Elmer Lambda 900 spectrometer. For TEM measurements, JEOL 3010 with an operating voltage of 300 KeV was used. TEM samples were prepared by drop coating nanoparticle solution on a Formvar-film-covered carbon coated copper grid. Particles size distribution was calculated from TEM images through digital micrograph imaging software. Raman and SERS measurements were conducted on a custom-built Raman microscope equipped with 532 nm wavelength laser provided by solid state frequency doubled Nd-YAG laser, described elsewhere [35]. The accumulation time for each spectrum was 10 s. For SERS studies, 5 μL of nanoparticles were mixed with 5 μL of 10^{-5} M R6G solution in water. 1 μL of the mixture was drop cast on a cleaned glass slide and dried in desiccator.

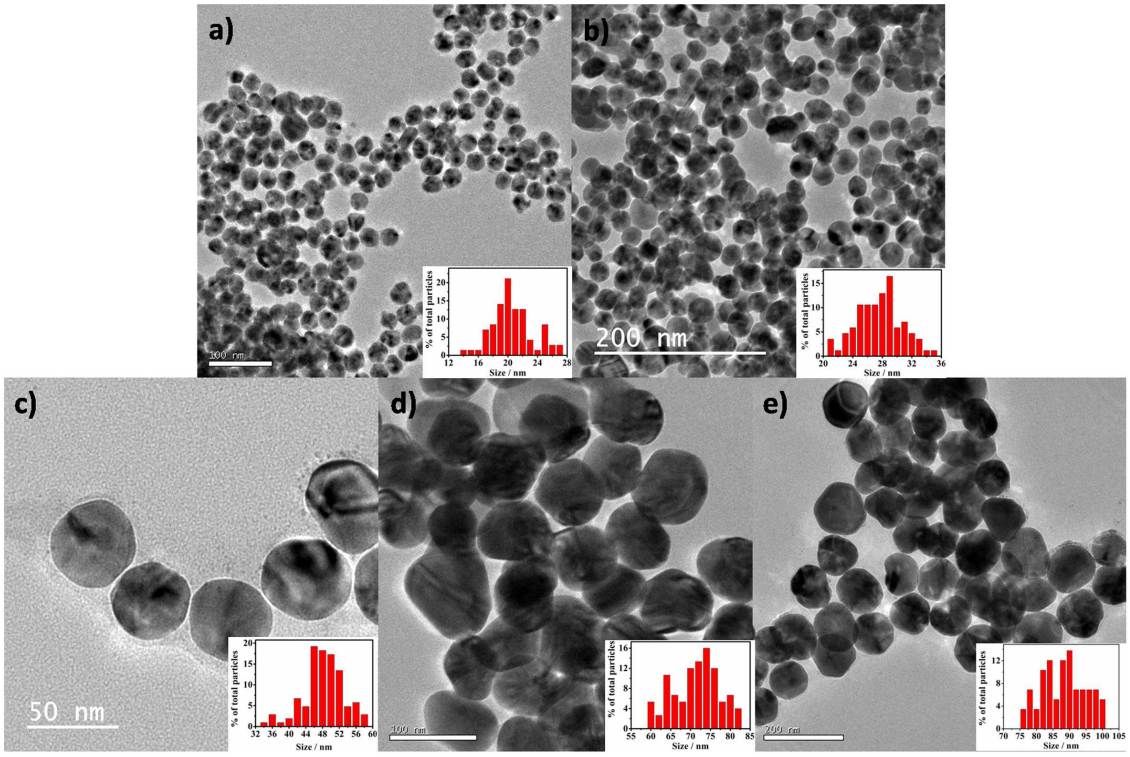

Figure 6.2: TEM images and particle size distribution calculated from TEM images using Digital Micrograph Software for Au@Ag nanoparticles of size (a) 20 nm, (b) 30 nm, (c) 45 nm, (d) 75 nm and (e) 90 nm. Scale bar is 100 nm for images (a) and (d), 200 nm for images (b) and (e), and 50 nm for image (c).

6.3 Results and Discussion

Figure 6.1a shows the extinction spectra of silver nanoparticles of size 20 nm (blue), 30 nm (pink), 45nm (green), 75nm (black) and 90 nm (red) with the surface plasmon resonances (SPR) occurring at values 392 nm, 401 nm, 412 nm, 439 nm and 460 nm respectively. Interestingly, bigger nanoparticles also show higher quadrupole modes around 390 nm (marked by star), attributable to varying electric field across the nanoparticle [21]. Since the extinction spectrum does not show any plasmon peak corresponding to the gold core, we will be referring Au@Ag nanoparticles as the silver nanoparticles. The dependence of SPR position on the nanoparticles size has been shown in Figure 6.1b. The systematic increase observed in the SPR position and the line widths with silver nanoparticle size are attributed to the retardation

Nanoparticle name	Au@Ag particle size (nm)	Silica shell thickness (nm)
Ag20@SiO_2_1	20	2.0
Ag30@SiO_2_1	30	2.6
Ag30@SiO_2_2	30	2.8
Ag45@SiO_2_1	45	2.2
Ag45@SiO_2_2	45	3.3
Ag75@SiO_2_1	75	2.4
Ag75@SiO_2_2	75	2.8
Ag75@SiO_2_3	75	4.4
Ag90@SiO_2_1	90	2.6
Ag90@SiO_2_2	90	3.4
Ag90@SiO_2_3	90	5.0

Table 6.5: Nanoparticle name and the associated core particle size as well as the silica shell thickness.

effects and increase in radiation damping respectively [19, 21] Plasmon damping is chiefly governed by non-radiative processes for smaller nanoparticles whereas for larger particles it is governed by radiative processes making them strong scatterers [20]. It is also known that as the size increases, the fraction of scattering in the extinction increases making larger nanoparticles better scatterers than smaller nanoparticles [19, 36]. Heterogeneity in size, shape and interaction with surrounding matrix is also known to contribute towards plasmon broadening [37]. Figure 6.2 shows the TEM images of silver nanoparticles along with the particle size distribution presented in the inset. It can be clearly seen that the smaller nanoparticles are homogenous in nature while it is not so in larger nanoparticles. Further, the synthesized silver nanoparticles are citrate capped and hence negatively charged at pH 7.

Distance dependent SERS studies necessitate the presence of spacer between the silver surface and the analyte molecules. Many such spacers have been employed in the past, such as double stranded DNA [38], thio-methylene spacers [39], polymer coating (polyethylene glycol or polystyrenesulfonate/ polydiallydimethylammonium-hydroxide) [40, 41], silica or alumina coating *etc.* [26, 29]. Each method has its own

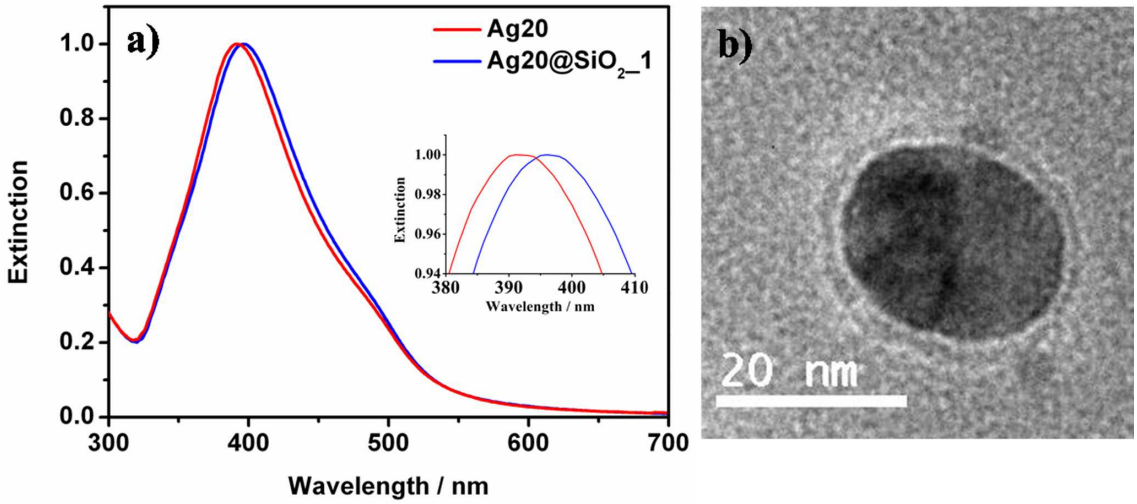

Figure 6.3: UV-visible spectra (a), and TEM image of Ag20@SiO_2_1 (b). Scale bar is 20 nm for all the figures.

limitations, like polymer coating yields strong SERS signal of polymer itself while flexibility of DNA chain spacer may yield inaccurate distances. Dielectric coating or silica coating in particular is one of the best ways to maintain distance between silver nanoparticles and analyte molecules in order to monitor the distance dependence in SERS while keeping the environment bio-compatible. Our method of thin layer silica coating on smaller nanoparticles (Ag20, Ag30 and Ag45) was primarily based on earlier report by Mulvaney *et al.* [31]. Since the procedure was not suitable for larger nanoparticles, an alternative approach based on the reports of Li *et al.* and Ung *et al.* was followed for Ag75 and Ag90 nanoparticles [26, 34]. Prior to silica coating, silver nanoparticle surface was modified with 3-aminopropyl triethoxysilane or trimethoxysilane. The silica shell was grown using a very low concentration of sodium silicate solution in water. It is known that the silica shell growth is highly dependent on the pH of the solution. At pH 12-14, thick silica shell forms while thin shell formation occurs at pH 9-10 [34]. In order to achieve thin silica coating, the pH of sodium silicate solution was reduced to pH 10 by addition of hydrochloric acid or orthophosphoric acid. In addition, silica shell growth is also a function of

aging time and temperature. The shell grows slowly at room temperature as the silica condensation reaction rate is low but the reaction rate increases many folds as the temperature is raised to 90 °C [26]. The silica shell thickness is increased by aging the solution at 90 °C. To halt the growth process, the reaction is quenched by putting the reaction mixture in an ice bath as reported in previous literature [26].

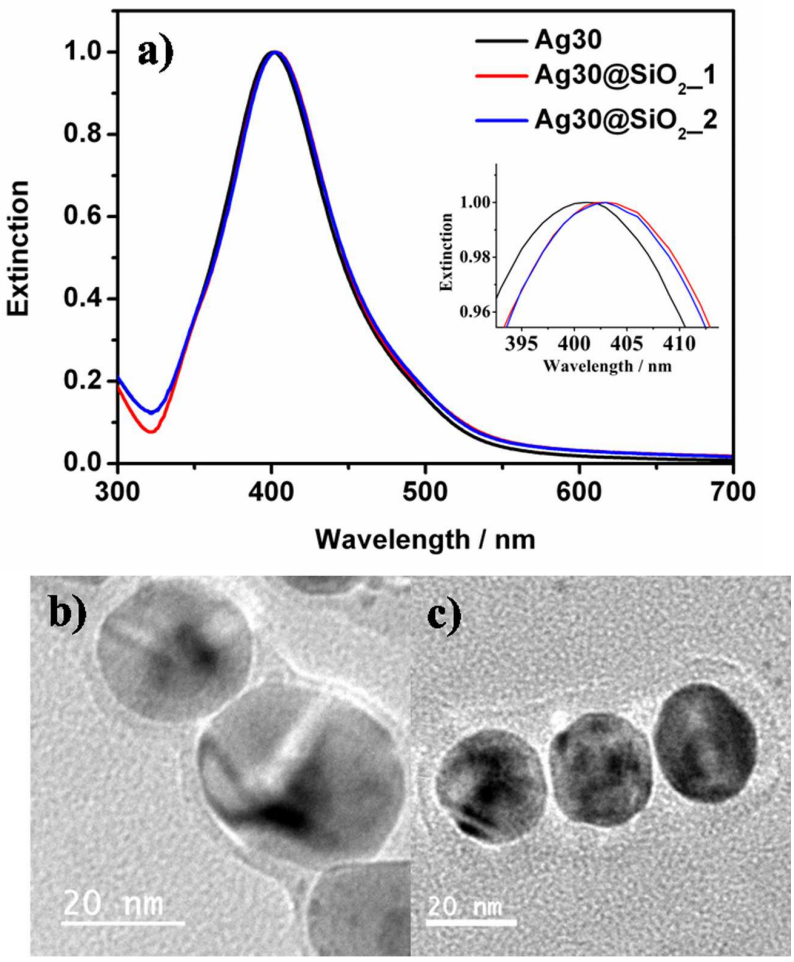

Figure 6.4: UV-visible spectra (a), and TEM images of Ag30@SiO_2_1 (b), Ag30@SiO_2_2 (c). Scale bar is 20 nm for all the figures.

Table 6.5 shows the silver nanoparticle name indicating the silver core size and silica shell thickness. Figure 6.3 to Figure 6.7 shows the extinction spectra of all the Ag@SiO_2 nanoparticles synthesized with various silica shell thickness along with their TEM images. It can be seen from the UV-visible spectra in Figures 6.3 to 6.7

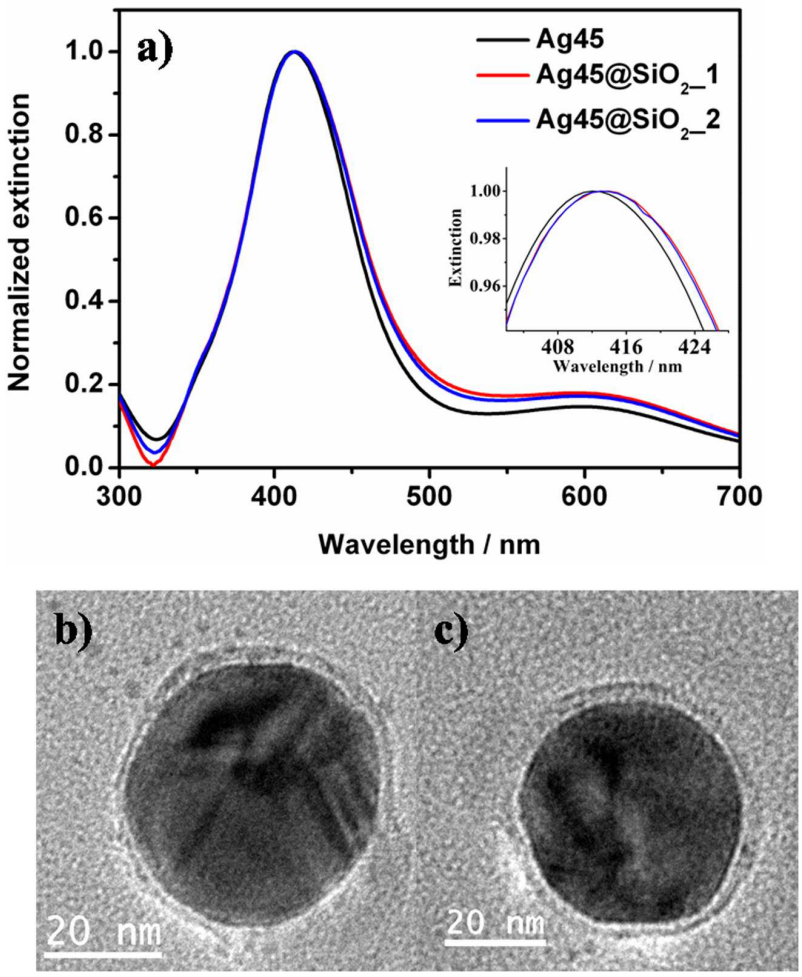

Figure 6.5: UV-visible spectra (a), and TEM images of Ag45@SiO_2_1 (b), Ag45@SiO_2_2 (c). Scale bar is 20 nm for all the figures.

that the SPR changes by a few nm (∼1 nm) on thin silica coating and is attributed to increase in refractive index of surrounding material. It has been shown that the SPR shifts by only 1 nm for thin polymer coating on metal nanoparticles, which conforms with our observation [42]. Thin silica coating on silver nanoparticles is a challenge in itself. Citrate capped silver nanoparticles are negatively charge and it is the electrostatic repulsion between the negative charges which prevents the nanoparticle from coalescing. Surface functionalization by APTES/APTMS leads to charge neutralization resulting into nanoparticle aggregation. To prevent aggregation, a minimum silica coating of 2-4 nm should occur. The synthesis method was

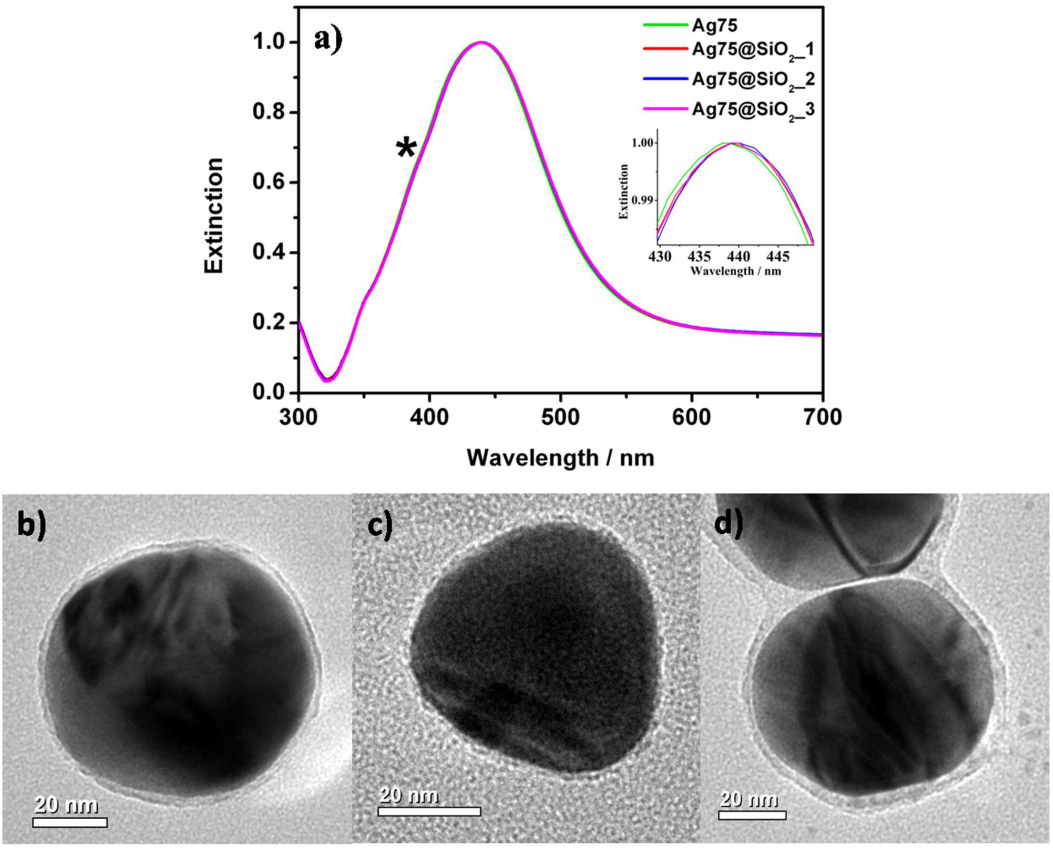

Figure 6.6: UV-visible spectra (a), and TEM images of Ag75@SiO_2_1 (b), Ag75@SiO_2_2 (c), Ag75@SiO_2_3 (d). Scale bar is 20 nm for all the figures.

optimized to get thin silica coating without aggregation of nanoparticles, nevertheless, we did observe aggregation in the smaller nanoparticles. Further, thin silica coating always yields a range of silica shell thickness. A single particle could also have a variation of ∼1 nm in shell thickness (see Figure 6.5b). Incidentally, it was also noticed that silica coating on the larger nanoparticles were more uniform and had a narrow distribution in comparison to smaller nanoparticles. TEM pictures in Figures 6.6 and 6.7 also show uniform coating on Ag75 and Ag90 nanoparticles.

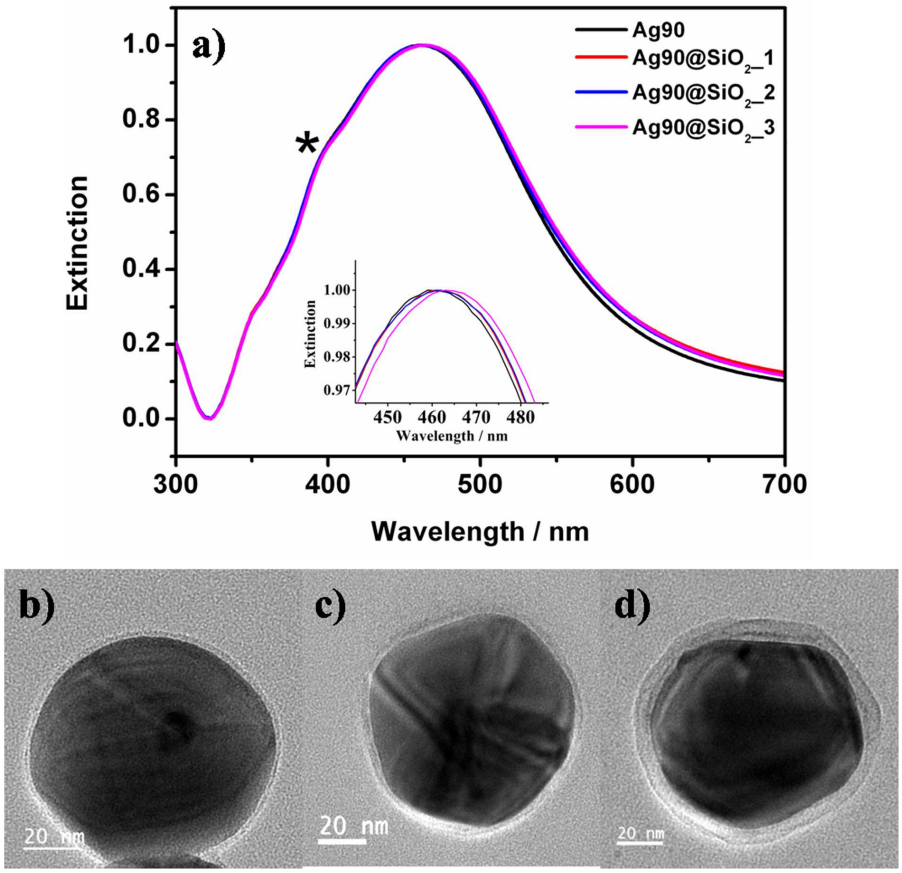

Figure 6.7: UV-visible spectra (a), and TEM images of Ag90@SiO_2_1 (b), Ag90@SiO_2_2 (c), Ag90@SiO_2_3 (d). Scale bar is 20 nm for all the figures.

6.3.1 SERS studies

It is well known that R6G shows surface enhanced resonant Raman (SERRS) on being excited by 532 nm laser. Since, resonance will not be affecting our conclusion but help in detecting signal at lower concentration, we have used R6G. The local field intensity around the nanoparticles increases as the particle size is increased. Figure 6.8 presents the SERS spectra of 10^{-5} M R6G adsorbed on citrate capped silver nanoparticles. It is observed that the SERS intensity initially increases with increase in particle size but decreases for 90 nm nanoparticles which is clearly depicted in Figure 6.8b. This decrease has also been observed previously for larger nanoparticles.

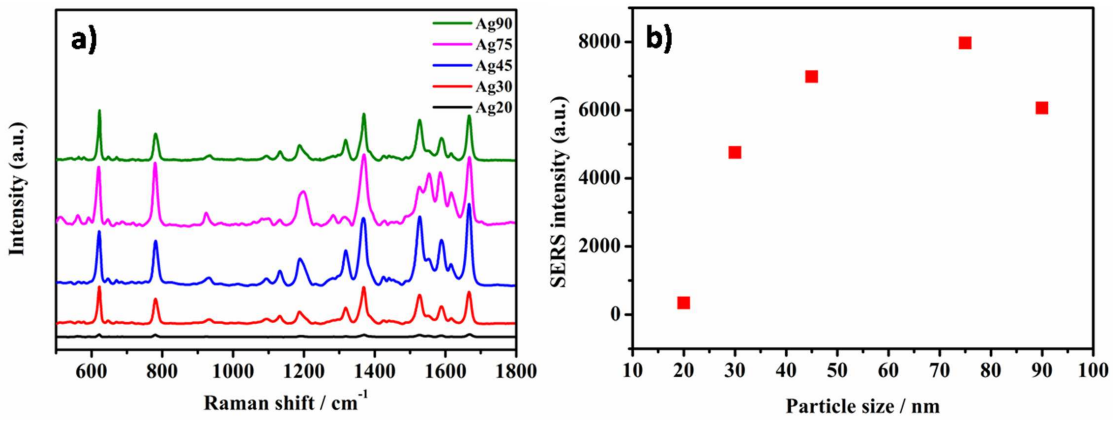

Figure 6.8: (a) SERS spectra of 10^{-5} M R6G on citrate capped silver nanoparticles of 20, 30, 45, 75 and 90 nm size, (b) SERS intensity of 611 cm^{-1} mode plotted as a function of particle size (right graph). Incident laser frequency used was 532 nm.

Shown in Figure 6.9 is the SERS spectra of 10^{-5} M R6G adsorbed on 30 nm, 45 nm, 75 nm and 90 nm silica coated silver nanoparticles. It is observed that the signal intensity decreases as the silica shell thickness increases. The intensity of C-C-C in-plane ring bending mode at 611 cm^{-1}, a signature peak with sharp feature of R6G, was chosen for determining the SERS intensity as a function of distance [43, 44]. 20 nm Ag nanoparticles having 2 nm silica shell did not show any SERS signal of R6G. Normalised SERS intensity (I_{SNP}/I_B, where I_{SNP} and I_B are the SERS intensities of R6G observed on silica coated nanoparticles and bare nanoparticles respectively) is plotted as a function of silica shell thickness in Figure 6.10. The signal decayed exponentially for 20 nm, 30 nm, 45 nm, 75 nm and 90 nm Ag nanoparticles. The decrease in SERS signal with the increase in distance from the nanoparticle also indicates the non-porous nature of silica shell.

For a monolayer of molecule on the nanoparticle surface, SERS intensity decays as $(1 + \frac{r}{d})^{10}$, where r is the radius of curvature of roughness and d is the distance of molecule from the surface [45]. For 10^{-5} M concentration of R6G chosen in the present work, there is a possibility of multilayer formation on the nanoparticle surface. Hence, the intensity decay does not fit into the above equation. Secondly,

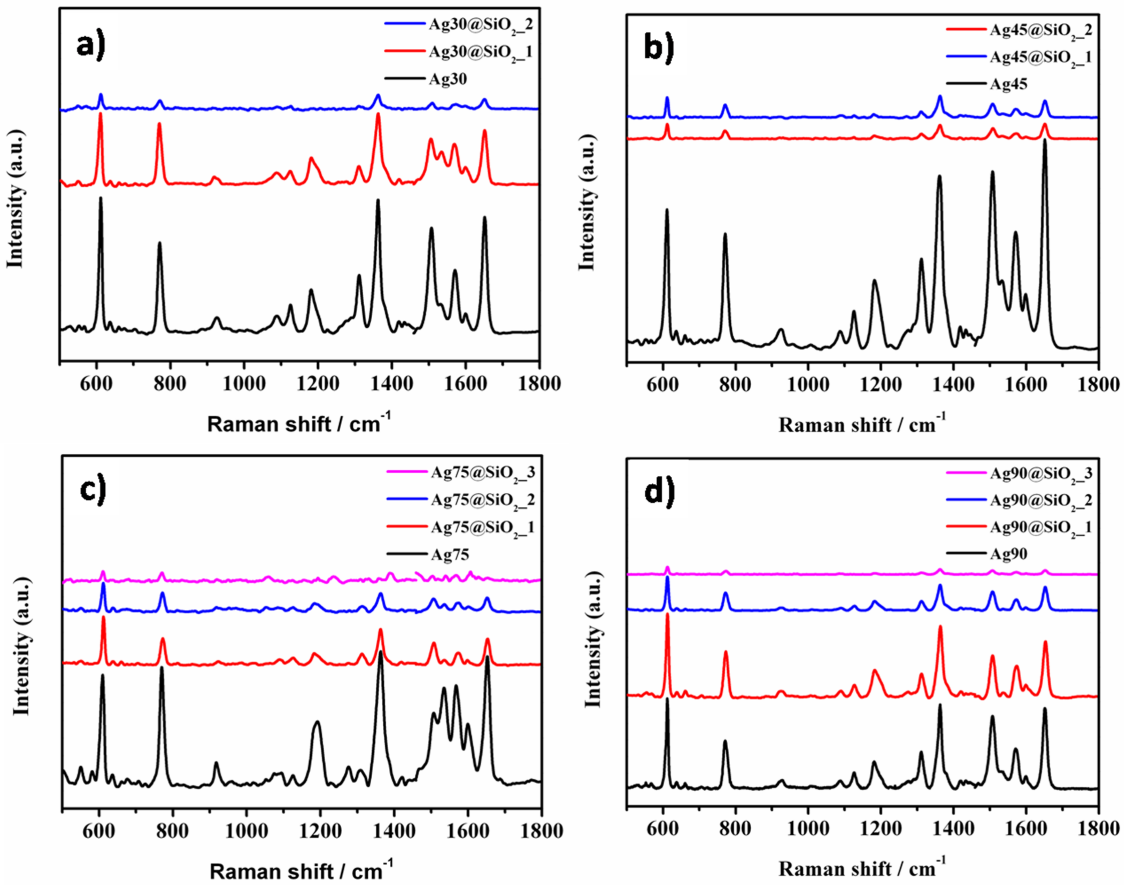

Figure 6.9: SERS spectra of 10^{-5} M R6G on a) Ag30, b) Ag45, c) Ag75 and Ag90 nanoparticles having different silica shell thickness.

due to the experimental limitation on precisely controlling the silica thickness in the aqueous medium, we could not have many data points to fit into this equation. Empirically, the decay in the SERS intensity is much sharper than what has been reported previously [45].

To demonstrate that the **accessible distance** *i.e.* the distance d from the nanoparticle surface up to which SERS can be observed is a function of nanoparticle size, we have plotted the distance d which is nothing but the maximum silica shell thickness for which SERS was observed (from Figure 6.10), against silver nanoparticle size in Figure 6.11. It is noticed that for 30 nm nanoparticle, SERS was observed up to a distance of 2.8 nm, while for 45 nm particles, SERS could be recorded as far as 3.2 nm. Surprisingly, for 75 nm particles, SERS intensity was obtained up to 4.4 nm and

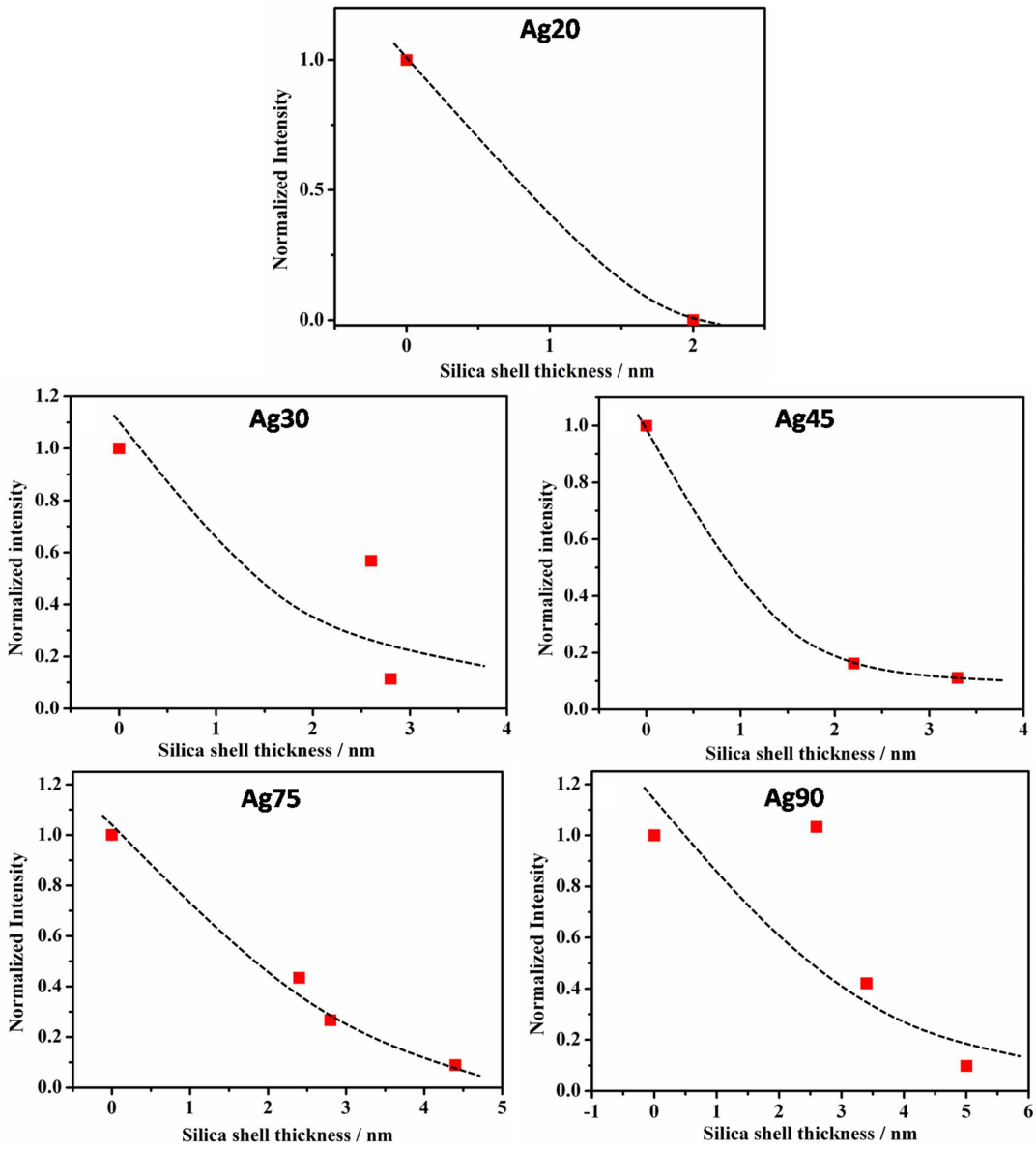

Figure 6.10: Normalised (I_{SNP}/I_B) SERS intensity of 611 cm^{-1} peak of R6G (10^{-5} M) as a function of silica shell thickness for 20nm, 30 nm, 45 nm, 75 nm and 90 nm silver nanoparticles showing that the distance up to which SERS is obtained increases as the nanoparticle size is increased. Black dotted line is the guide to the eye.

for 90 nm Ag nanoparticles, SERS was observed up to 5 nm from the nanoparticle surface. Certainly, increased accessible distance for larger nanoparticles do not result from more number molecules adsorbed on such particles or incident laser being closer to the SPR, because if that would have been the reason, we would have seen its effect on SERS of R6G on bare 90 nm silver nanoparticles whose intensity intensity

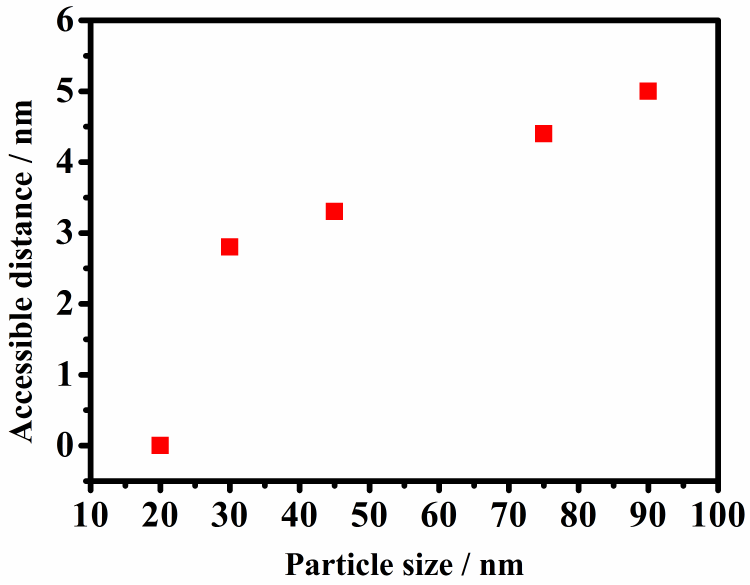

Figure 6.11: SERS accessible distance as a function of Ag nanoparticles size.

was found to be lesser than that observed on 75 nm nanoparticles. Hence, we believe that its only larger dipole size and more number of dipoles in Ag90 nanoparticles which are responsible for larger accessible distance. Here, it must be noted that the accessible distance will not continue to rise with the particle size but would start decreasing after ∼100 nm because nanoparticles larger than 100 nm are not efficient SERS enhancers [22].

6.3.2 FDTD simulations

To further explain the experimental observation, near field intensity of silica coated silver nanoparticles was calculated using finite difference time domain method (FDTD). The electromagnetic wave of wavelength 532 nm polarized along x-direction was incident from y-direction onto the nanoparticles. In order to accurately calculate the electric field, smaller mesh size of 0.25 nm was chosen for Ag20, and relatively larger grid size of 0.5 nm was chosen for Ag90 nanoparticles. PML boundaries were chosen as they absorb the light entering them. The electric field intensity at

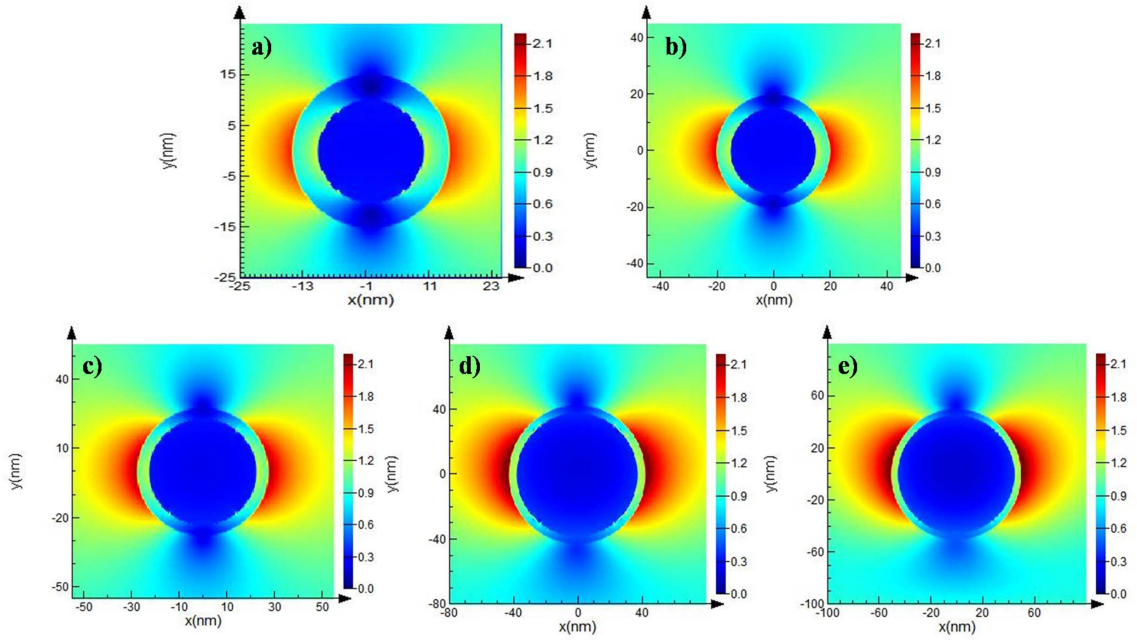

Figure 6.12: FDTD analysis showing normalised electric field intensity distribution on a) Ag20, b) Ag30, c) Ag45, d) Ag75 and e) Ag90 nanoparticles each having 5 nm silica shell thickness.

a distance of 5 nm from all the nanoparticle sizes was calculated by making silica shell thickness of 5 nm and is presented in Figure 6.12. It can be clearly seen that the field intensity shows a gradual increase with the size of nanoparticle and is highest for Ag90 nanoparticles, thus conforming with our experimental observation. Further, the field at 2 nm from Ag20 nanoparticles is only ∼2 times the incident field intensity while the field at a distance of even 5 nm in Ag90 nanoparticles is 2.3 times the incident field. Another feature to be noticed from Figure 6.12 is the distorted electric field lobe for Ag90 nanoparticles. This is attributed to the presence of varying electric field across larger nanoparticle giving rise to quadrupole mode.

6.4 Conclusions

We have shown that the accessible distance up to which SERS is observed is strongly dependent on the size of the nanoparticle. This inference was arrived

at based on systematic study on Au@Ag@SiO_2 nanoparticles of different Au@Ag core size and silica shell thickness. We could illustrate that the Raman signal can be enhanced even at a distance of 5 nm from the colloidal nanoparticles of 90 nm size, hitherto never demonstrated. Hence, by tuning the Au@Ag nanoparticle size, not only surface modes but other modes of molecules which are not in proximity of nanoparticle can also be obtained. Thus, the statement that SERS occurs for molecule at 1 nm from the nanoparticle surface is true only for smaller and isolated nanoparticles bearing a monolayer of molecule. Since most bio-molecular studies are conducted in aqueous medium where it is difficult to have control on monolayer formation and nanoparticle aggregation, we need to critically choose the size of nanoparticle which can give the best information. This result will be helpful in selecting the nanoparticle size depending on the size of analyte system. For instance, SERS studies of macromolecules, polymers or proteins using larger nanoparticles (90 nm) can give better information in comparison to that obtained using smaller nanoparticles, as the vibrational modes buried deep inside proteins will also be electromagnetically enhanced and may appear in SERS spectrum except when it is forbidden due to the selection rules.

Bibliography

[1] M. Moskovits, *Surface-enhanced spectroscopy*, Reviews of modern physics **57**, 783 (1985).

[2] P. L. Stiles, J. A. Dieringer, N. C. Shah, and R. P. Van Duyne, *Surface-enhanced Raman spectroscopy*, Annu. Rev. Anal. Chem. **1**, 601 (2008).

[3] J. Creighton, *Surface Raman electromagnetic enhancement factors for molecules at the surface of small isolated metal spheres: The determination*

of adsorbate orientation from SERS relative intensities, Surface Science **124**, 209 (1983).

[4] N. Valley, N. Greeneltch, R. P. Van Duyne, and G. C. Schatz, *A look at the origin and magnitude of the chemical contribution to the enhancement mechanism of surface-enhanced Raman spectroscopy (SERS): Theory and experiment*, The Journal of Physical Chemistry Letters **4**, 2599 (2013).

[5] L. Vigderman and E. R. Zubarev, *Starfruit-shaped gold nanorods and nanowires: synthesis and SERS characterization*, Langmuir **28**, 9034 (2012).

[6] G. Kumari and C. Narayana, *New nano architecture for SERS applications*, The Journal of Physical Chemistry Letters **3**, 1130 (2012).

[7] W. J. Cho, Y. Kim, and J. K. Kim, *Ultrahigh-density array of silver nanoclusters for SERS substrate with high sensitivity and excellent reproducibility*, ACS nano **6**, 249 (2012).

[8] J.-H. Lee *et al.*, *Tuning and maximizing the single-molecule surface-enhanced Raman scattering from DNA-tethered nanodumbbells*, ACS nano **6**, 9574 (2012).

[9] W. Xie, B. Walkenfort, and S. Schlücker, *Label-free SERS monitoring of chemical reactions catalyzed by small gold nanoparticles using 3D plasmonic superstructures*, Journal of the American Chemical Society **135**, 1657 (2013).

[10] E. C. Le Ru and P. G. Etchegoin, *Single-molecule surface-enhanced Raman spectroscopy*, Annual review of physical chemistry **63**, 65 (2012).

[11] R. Zhang *et al.*, *Chemical mapping of a single molecule by plasmon-enhanced Raman scattering*, Nature **498**, 82 (2013).

[12] X.-M. Qian and S. Nie, *Single-molecule and single-nanoparticle SERS: from*

fundamental mechanisms to biomedical applications, Chemical Society Reviews **37**, 912 (2008).

[13] T. Konishi *et al.*, *Single molecule dynamics at a mechanically controllable break junction in solution at room temperature*, Journal of the American Chemical Society **135**, 1009 (2012).

[14] K. Kneipp *et al.*, *Detection and identification of a single DNA base molecule using surface-enhanced Raman scattering (SERS)*, Physical Review E **57**, R6281 (1998).

[15] D. Karthigeyan *et al.*, *SERS and MD simulation studies of a kinase inhibitor demonstrate the emergence of a potential drug discovery tool*, Proceedings of the National Academy of Sciences **111**, 10416 (2014).

[16] P. P. Kundu *et al.*, *Allosteric Transition Induced by Mg^{2+} Ion in a Transactivator Monitored by SERS*, The Journal of Physical Chemistry B **118**, 5322 (2014).

[17] S. Schlücker, *Surface-Enhanced Raman Spectroscopy: Concepts and Chemical Applications*, Angewandte Chemie International Edition **53**, 4756 (2014).

[18] A. Campion and P. Kambhampati, *Surface-enhanced Raman scattering*, Chem. Soc. Rev. **27**, 241 (1998).

[19] U. Kreibig and M. Vollmer, in *Optical properties of metal clusters* (Springer Berlin, , 1995), Vol. 25.

[20] K. Kolwas and A. Derkachova, *Plasmonic abilities of gold and silver spherical nanoantennas in terms of size dependent multipolar resonance frequencies and plasmon damping rates*, Opto-Electronics Review **18**, 429 (2010).

[21] C. Sönnichsen *et al.*, *Plasmon resonances in large noble-metal clusters*, New Journal of Physics **4**, 93 (2002).

[22] K. G. Stamplecoskie, J. C. Scaiano, V. S. Tiwari, and H. Anis, *Optimal size of silver nanoparticles for surface-enhanced Raman spectroscopy*, The Journal of Physical Chemistry C **115**, 1403 (2011).

[23] W.-C. Lin *et al.*, *Size dependence of nanoparticle-SERS enhancement from silver film over nanosphere (AgFON) substrate*, Plasmonics **6**, 201 (2011).

[24] P.-P. Fang *et al.*, *Optimization of SERS activities of gold nanoparticles and gold-core–palladium-shell nanoparticles by controlling size and shell thickness*, Journal of Raman Spectroscopy **39**, 1679 (2008).

[25] D.-K. Lim *et al.*, *Highly uniform and reproducible surface-enhanced Raman scattering from DNA-tailorable nanoparticles with 1-nm interior gap*, Nature nanotechnology **6**, 452 (2011).

[26] J. F. Li *et al.*, *Surface analysis using shell-isolated nanoparticle-enhanced Raman spectroscopy*, nature protocols **8**, 52 (2013).

[27] J. F. Li *et al.*, *Shell-isolated nanoparticle-enhanced Raman spectroscopy*, Nature **464**, 392 (2010).

[28] L. Qin *et al.*, *Designing, fabricating, and imaging Raman hot spots*, Proceedings of the National Academy of Sciences **103**, 13300 (2006).

[29] M. Shanthil, R. Thomas, R. Swathi, and K. George Thomas, *$Ag@SiO_2$ Core–Shell Nanostructures: Distance-Dependent Plasmon Coupling and SERS Investigation*, The Journal of Physical Chemistry Letters **3**, 1459 (2012).

[30] P. B. Johnson and R.-W. Christy, *Optical constants of the noble metals*, Physical Review B **6**, 4370 (1972).

[31] S. P. Mulvaney, M. D. Musick, C. D. Keating, and M. J. Natan, *Glass-coated, analyte-tagged nanoparticles: a new tagging system based on detection with surface-enhanced Raman scattering*, Langmuir **19**, 4784 (2003).

[32] P. Lee and D. Meisel, *Adsorption and surface-enhanced Raman of dyes on silver and gold sols*, The Journal of Physical Chemistry **86**, 3391 (1982).

[33] V. Uzayisenga *et al.*, *Synthesis, characterization, and 3D-FDTD simulation of Ag@SiO_2 nanoparticles for shell-isolated nanoparticle-enhanced Raman spectroscopy*, Langmuir **28**, 9140 (2012).

[34] T. Ung, L. M. Liz-Marzán, and P. Mulvaney, *Controlled method for silica coating of silver colloids. Influence of coating on the rate of chemical reactions*, Langmuir **14**, 3740 (1998).

[35] G. V. P. Kumar and C. Narayana, *Adapting a fluorescence microscope to perform surface enhanced*, Current science **93**, 778 (2007).

[36] P. K. Jain, K. S. Lee, I. H. El-Sayed, and M. A. El-Sayed, *Calculated absorption and scattering properties of gold nanoparticles of different size, shape, and composition: applications in biological imaging and biomedicine*, The Journal of Physical Chemistry B **110**, 7238 (2006).

[37] H. Hövel *et al.*, *Width of cluster plasmon resonances: bulk dielectric functions and chemical interface damping*, Physical Review B **48**, 18178 (1993).

[38] A. K. Singh *et al.*, *Development of a long-range surface-enhanced Raman spectroscopy ruler*, Journal of the American Chemical Society **134**, 8662 (2012).

[39] B. Kennedy, S. Spaeth, M. Dickey, and K. Carron, *Determination of the distance dependence and experimental effects for modified SERS substrates based on self-assembled monolayers formed using alkanethiols*, The Journal of Physical Chemistry B **103**, 3640 (1999).

[40] D. Radziuk and H. Moehwald, *Highly effective hot spots for SERS signatures of live fibroblasts*, Nanoscale **6**, 6115 (2014).

[41] D. I. Gittins and F. Caruso, *Tailoring the polyelectrolyte coating of metal nanoparticles*, The Journal of Physical Chemistry B **105**, 6846 (2001).

[42] Y. Kobayashi *et al.*, *Silica coating of silver nanoparticles using a modified Stöber method*, Journal of colloid and interface science **283**, 392 (2005).

[43] P. Hildebrandt and M. Stockburger, *Surface-enhanced resonance Raman spectroscopy of Rhodamine 6G adsorbed on colloidal silver*, The Journal of Physical Chemistry **88**, 5935 (1984).

[44] A. Kudelski, *Raman studies of rhodamine 6G and crystal violet sub-monolayers on electrochemically roughened silver substrates: Do dye molecules adsorb preferentially on highly SERS-active sites?*, Chemical physics letters **414**, 271 (2005).

[45] J. A. Dieringer *et al.*, *Surface enhanced Raman spectroscopy: new materials, concepts, characterization tools, and applications*, Faraday discussions **132**, 9 (2006).

Chapter 7

New Nanoarchitecture for SERS Applications

7.1 Introduction

Metal nanoparticles support localized surface plasmon resonance (LSPR) owing to the presence of conduction electrons. The presence of LSPR gives rise to fascinating properties and make them promising materials in physcial sciences and biological sciences. These properties are a function of nanoparticle size [1–3], shape [4–6], composition [7, 8], dielectric constant of material and surrounding medium which are manifested as change in SPR position [9, 10]. Silver, gold and copper, owing to their dielectric properties and chemical stability at ambient conditions are ideal materials for SPR applications. When the nanoparticle is composed of more than one metal, than its optical properties are determined by the dielectric properties of all the constituent metals. There have been many reports on the bimetallic

Reprinted(adapted) with permission from "New Nano Architecture for SERS Applications" *J. Phys. Chem. Lett.* **2012**, *3*, 1130-1135. Copyright 2012, American Chemical Society. `http://pubs.acs.org/doi/abs/10.1021/jz3001344`

nanoparticles formed by the successive reduction of metal atoms [11, 12]. Silver and gold is particularly interesting because of their similar lattice constants (Au: 4.078 Å; Ag: 4.086 Å). As early as 1964, Morris and Collins reported the synthesis of silver-gold multilayer colloid [13]. However, numerous literatures on metal nanoparticles started appearing only a couple of decades back. Halas and colleagues have shown various plasmonic nanostructures of silver and gold which find application in surface enhanced Raman scattering (SERS) [14–18]. There is an inherent complexity associated with bimetallic nanoparticles resulting into intermetallic interactions such as oxidation of one metal by other. To circumvent this problem, Schierhorn and Liz-Marzan used silica layer between gold and silver [19]. Further, Kim *et al.* also reported a method to prepare silver nanostructures on silica spheres for SERS [20].

As discussed in the previous chapter, SERS is the enhancement of Raman signal of a molecule present in the vicinity of metal nanoparticles. This enhancement is due to a) electromagnetic enhancement, which occurs when a molecule is present in the vicinity of intense electric field resulting from excitation of surface plasmon resonances at the metal-dielectric interface and, b) chemical enhancement, which occurs when the molecule forms a charge transfer complex with metal nanoparticles [21–23]. The total enhancement produced from a nanoparticle is quantified by a term called enhancement factor. This enhancement factor is inversely proportional to the distance d from nanoparticles and dies off at a rate of $1/d^{12}$ [21, 24]. Thus, most of the enhancement occurs near the surface of nanoparticle.

There have been numerous efforts to increase the SERS enhancment factor in order to achieve higher and higher limit of detection. Lian C.T. Shoute *et al.* showed an increase in Raman signal intensity when the analyte is adsorbed on a planar reflecting substrate made from silicon-silica-silver trilayer, owing to the constructive interference of incident light and refracted light from the silicon layer [25, 26]. For

most biological applications, colloidal particles are favored to planar substrates attributed to their ability to get dispersed in a solvent. This motivated us to design colloidal nanoparticles having architecture similar to that proposed by Shoute. Due to the inert nature of gold toward biomolecules, gold was chosen to form the outermost island surface. The core is made from silver coated with silica. The silica shell thickness was optimized to get maximum enhancement. The enhancement factor calculation has been carried out using thiophenol. The additional enhancement due to reflection from silver core is demonstrated by synthesizing silica core gold island shell nanoparticles without silver core.

7.2 Experimental details

7.2.1 Synthesis of sandwich nanoparticles

Synthesis of Silver Core.The silver core-silica shell nanoparticle ($Ag@SiO_2$) was prepared by the method given by Chaorong Li *et al* [27]. 100 mL of absolute ethanol (Commercial Alcohols, AR) and 50 mL of milli-Q water was vigorously stirred at 80 °C. 10 mL of a 0.05 M aqueous solution of silver nitrate (Sigma Aldrich) was added to the water-alcohol mixture and stirred for 5 min, while heating continuously. Then, 20 mL of 2.5 mM poly-N-vinyl pyrrolidone, PVP (Loba Chemie) was added in aliquots of 1 mL in 5 min. After the mixture was stirred for 20 min at 80 °C, 5 mL of 0.1 M NaOH (Merck) was added to the solution. The solution was cooled, and the stirring was continued for 2 h, after which silver nanoparticles were obtained.

Silica shell coating. For the silica coating, 50 mL of absolute ethanol, 5 mL of ammonia solution (28-33 %, Merck), and 1 mL of tetraethyl orthosilicate, TEOS (Merck) in aliquots of 200 μL were added to the PVP-capped silver nanoparticles. This solution was stirred overnight (12 h) at room temperature. The $Ag@SiO_2$

nanoparticles formed were washed with a 1:1 solution of ethanol and water. The bare silica nanoparticles formed in the process were removed by centrifuging the core-shell nanoparticles at 8000 rpm. The supernatant was thrown. The nanoparticles were dried at 100 °C before gold coating.

To obtain different silica shell thicknesses, the volume of TEOS was varied. 600 μL, 1 mL, 2 mL and 4mL of TEOS was added to obtain silica shells of 25, 40, 50 and 60 nm respectively.

Formation of Gold island on silica shell. Gold coating over Ag@SiO_2 nanoparticles was carried out by using a modified approach for gold coating on silica given by Christina Graf *et al.* [28] wherein primarily, gold clusters were attached to the silica shell followed by growth of gold islands on the seed. 50 mg of the above synthesized Ag@SiO_2 nanoparticles was suspended in 10 mL of a 2% solution of APTES (Sigma Aldrich) in ethanol and sonicated for 1 h. This was then washed with ethanol and redispersed in 50 mL of ethanol. Gold nanoclusters (2 nm) were prepared by adopting the method given by Duff *et al* [29]. Briefly, 45.5 mL of water was put in a 100 mL round-bottom (RB) flask. To this, 1.5 mL of 0.2 M NaOH was added while stirring, and 120 μL of an 80% aqueous solution of tetrakis(hydroxymethyl)phosphonium chloride, THPC (Sigma-Aldrich), was diluted with water to make a total volume of 10 mL. Then, 1 mL of the diluted THPC solution was added to the RB. Next, 2 mL of a 25 mM dark aged solution of aurochloric acid, $HAuCl_4$ (Spectrochem), was added to the above mixture, resulting in the formation of orange-brown hydrosols of gold. An interval of 2 min was maintained between the addition of $HAuCl_4$ and THPC. It is advisible to use a freshly prepared solution of gold cluster as they are unstable and have a tendency to grow.

The APS-modified Ag@SiO_2 nanoparticles (50 mL) were added dropwise to the gold nanoparticle solution in 10 min. The solution was stirred for 12 h. Free gold

nanoparticles were removed by centrifuging at 8000 rpm and decanting the supernatant. The washed nanoparticles were re-dispersed in 100 mL of water, stirred for 1 h to form a uniform colloidal solution, and kept for aging in a refrigerator at 4 °C for a week.

A 0.22 mM $HAuCl_4$ solution (20 mL) and 10 mL of a 1.8 mM hydroxylamine hydrochloride (Fluka) solution in water were added simultaneously dropwise to 10 mL of precursor Ag@SiO_2@Au-seeded nanoparticles while stirring. Stirring was further continued for 1 h after the final addition. The color of the nanoparticles changed from black to reddish-brown as the gold island grew in size.

For different densities of gold islands on the silica shell, the APTES concentration in ethanol was changed, and the concentration of $HAuCl_4$ was varied from 0.11 to 0.44 mM in the gold island growth solution.

Synthesis of silica core gold island shell nanoparticles. 5 mL of ammonia solution was added to 50 mL of absolute ethanol. 1 mL of TEOS in aliqouts of 200μL was added every 10 min. The solution was stirred for 1 h resulting into the formation of silica spheres. The solution was then dried. 50 mg of silica spheres were added to 10 mL of 2% APTES in ethanol and sonicated for 1 h. This was centrifuged at 8000 rpm and redispersed in 50 mL ethanol. This solution was added to 50 mL of 2 nm gold cluster solution dropwise and stirred for 2 h. The solution was centrifuged at 8000 rpm, redispersed in 100 mL water and stirred for 45 min after which it was kept undisturbed at 10 °C to age for a week. Then, 20 mL of 0.22 mM $HAuCl_4$ solution and 10 mL of a 1.8 mM hydroxylamine hydrochloride solution in water were added simultaneously dropwise to the 10 mL of SiO_2@Au-seeded nanoparticles while stirring. Stirring was further continued for 1 h to complete the growth process.

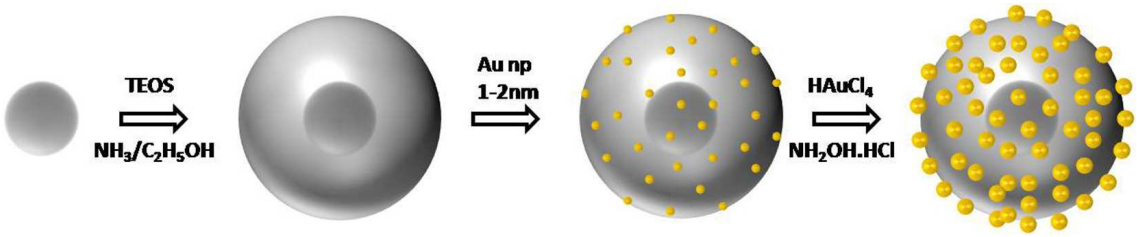

Scheme 7.1: Step-wise synthesis of sandwich nanoparticles

7.2.2 Characterization

UV−visible extinction spectra of the colloids were recorded from the dilute solutions in a 1 cm quartz cell using a Perkin-Elmer Lambda 900 spectrometer. TEM measurements were performed using a JEOL 3010 with an operating voltage of 300 KeV. Samples for TEM were prepared by drop coating on a Formvar-film-covered carbon coated copper grid. The powder XRD pattern was recorded with Cu−Kα radiation (Bruker D8 discover; 40 kV, 30 mA). Raman and SERS measurements were performed by a custom-built Raman microscope with a He−Ne laser of 632.8 nm wavelength, described elsewhere [30].

SERS measurements. For SERS measurements, 1 mL of Ag@SiO_2@Au was centrifuged and redispersed in 200 μL of water. Then, the analyte thiophenol was mixed with the nanoparticles, and 1 μL of the mixture was dropped and dried on a glass slide. SERS of the dried sample was recorded.

7.3 Results and Discussions

Scheme 7.1 shows the stepwise synthesis of sandwich Ag@SiO_2 nanoparticles. PVP capped 40 nm silver nanoparticles formed the core of sandwich nanostructure. Figure 7.1a shows the extinction spectrum of silver nanoparticles having a peak at 424 nm. Modified Stober's method was followed to form silica shell over silver nanoparticles wherein TEOS presursor in ethanolic solution of ammonia was used [31]. Ammonia catalyzes the formation of silica shell by hydrolyzing TEOS to form

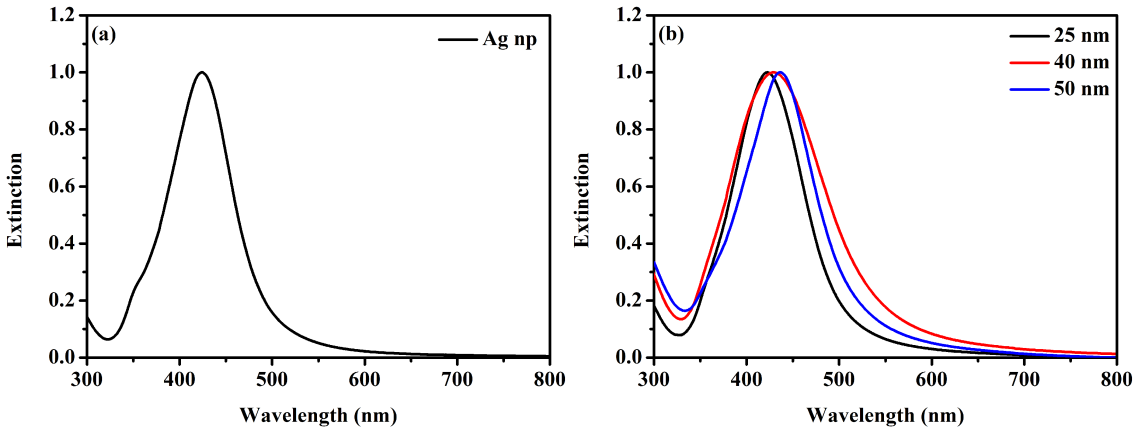

Figure 7.1: Extinction spectrum of (a) 40 nm silver nanoparticles, and (b) silver-silica core shell nanoparticles having 25 nm (black curve), 40 nm (red curve) and 50 nm (blue curve) silica shell thickness.

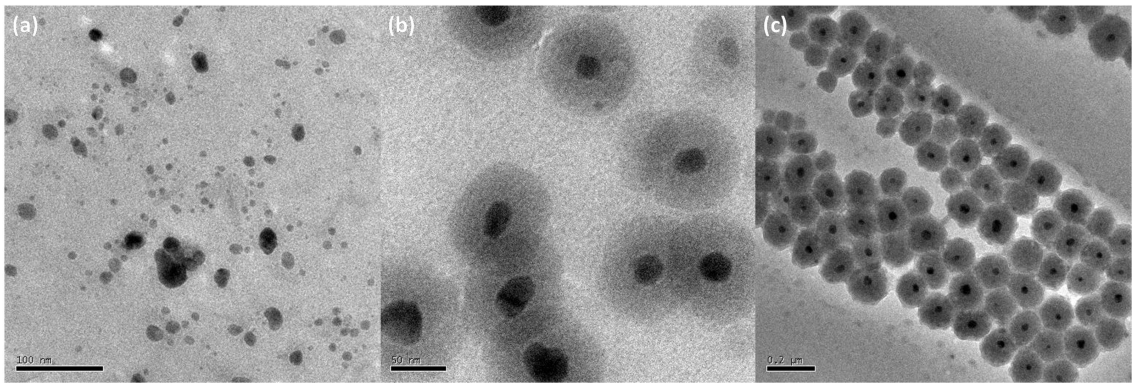

Figure 7.2: TEM images of (a) silver nanoparticles, (b)silver-silica core shell nanoparticle with 40 nm, and (c) 50 nm silica shell thickness. Scale bar is 100 nm for (a), 50 nm for (b) and 0.2 μm for (c) image.

$Si(OH)_4$ which condenses over time to form silica shell. The volume of TEOS was varied to obtain silica shells of 25, 40, 50 and 60 nm respectively. Silica coating causes a red shift in the plasmon resonance peak due to the increase in refractive index of the surrounding medium. As the shell thickens further, the SPR position shifts towards red too as shown in Figure 7.1b. Figure 7.2 shows the TEM images of silver nanoparticles and silver-silica core shell nanoparticles having different silica shell thickness.

For incident light to penetrate the silica layer, the gold coating must be in the form of islands or perforated. Gaps or crevices in the gold layer would facilitate light to

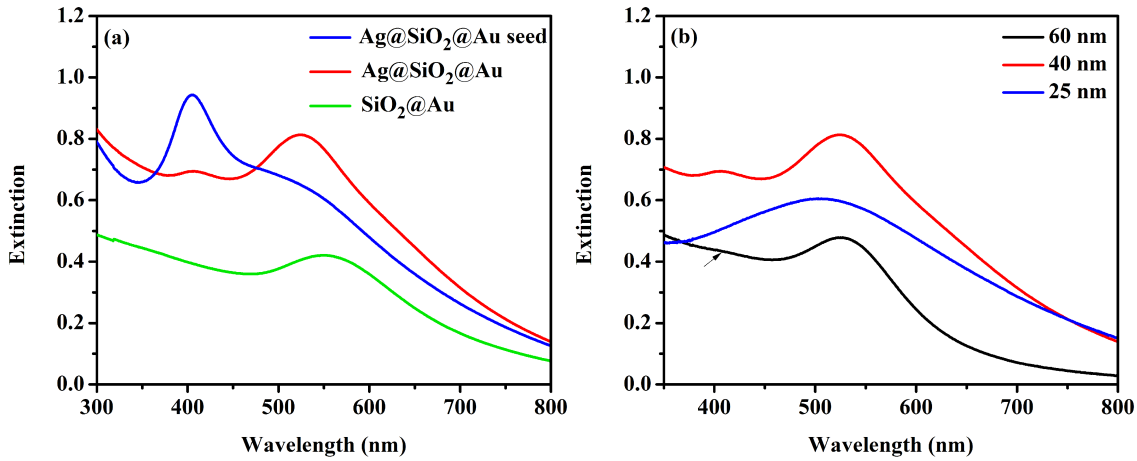

Figure 7.3: Extinction spectrum of (a) silver-silica-gold seed (blue curve), fully grown silver-silica-gold sandwich nanoparticles (red curve), silica core-gold island nanoparticles (green curve); and (b) silver-silica-gold sandwich nanoparticles with 25 nm (blue curve), 40 nm (red curve) and 60 nm (black curve) silica shell thickness. Arrow in the Figure (b) shows hidden silver peak.

pass through it. The best way to create this is to have gold nanoparticles on the silica surface. It was initially shown by Oldenburg *et al.* that gold shells on silica sphere can be formed by growth of gold clusters by reducing aurochloric acid with sodium borohydride [32–35]. However, Graf *et al.* observed that strong reducing agents although reduces gold on gold clusters, it inadvertently also results into formation of gold nucleates in solution [28]. To prevents formation of such nucleates, Theissen *et al.* suggested hydroxylamine-hydrochloride which reduces Au^{3+} on gold nuclei already existing in the solution [36]. Duff *et al.* further modified this method in order to grow clusters by seeding process [29]. Later these methods were used by Graf to grow gold shell on silica sphere [28].

We moderately modified Graf's method of gold coating to synthesize silver-silica-gold sandwich nanoparticles. Primarily, orange-brown gold clusters of size 2 nm were synthesized. In order to adhere gold clusters on silica surface, silver-silica core shell nanoparticles were functionalized with 3-aminopropyl triethoxy silane (APTES). On the attachment of gold clusters on silica shell, a hump around 523 nm is observed (Figure 7.3a, blue curve). It is also noticed that the SPR of silver shifts from 429 nm

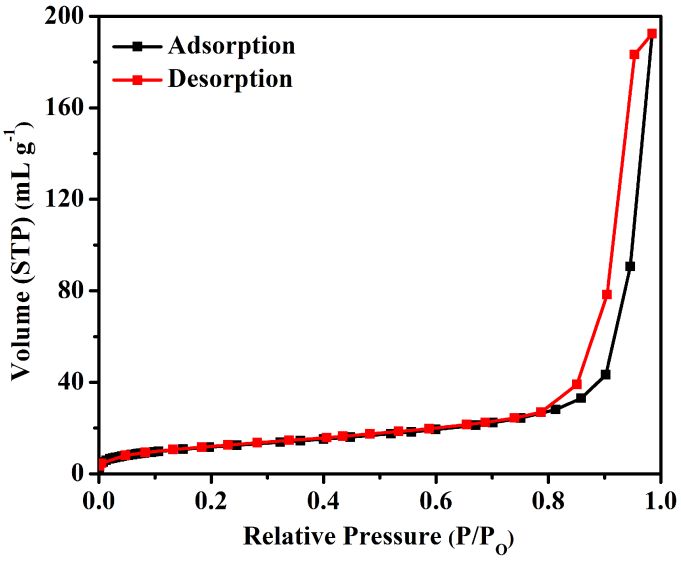

Figure 7.4: BET nitrogen adsorption-desorption isotherm of silver core silica shell nanoparticles.

(for 40 nm silica shell) to 405 nm for the seeded nanoparticles implying the reduction in size of silver core. Gold has higher positive reduction potential (+1.5 V) than silver (+0.8 V). So, on addition of core shell solution to the gold cluster solution, few Au^{3+} permeates the silica shell and oxidizes the silver core thus reducing its size. Total oxidation of silver core is prevented due to the practically non-porous nature of silica shell as observed from the BET measurements (Figure 7.4). However, during the growth of gold island Au^{3+} ions are added which might oxidize silver. To arrest the oxidation of silver, (a) an optimal concentration of aurochloric acid was chosen and (b) the gold precursor solution and the reducing agent (hydroxylamine hydrochloride) were added simultaneously and dropwise. Concentration of gold solution was optimised to obtain desired gold island size. It must be mentioned here that, potassium carbonate aids the oxidation of silver and must not be added in the gold growth solution as opposed to what was reported in the previous literature. Figure 7.3a (red curve) shows the extinction spectra of silver-silica gold sandwich nanoparticles with two prominent peaks at 407 nm and 524 nm corresponding to

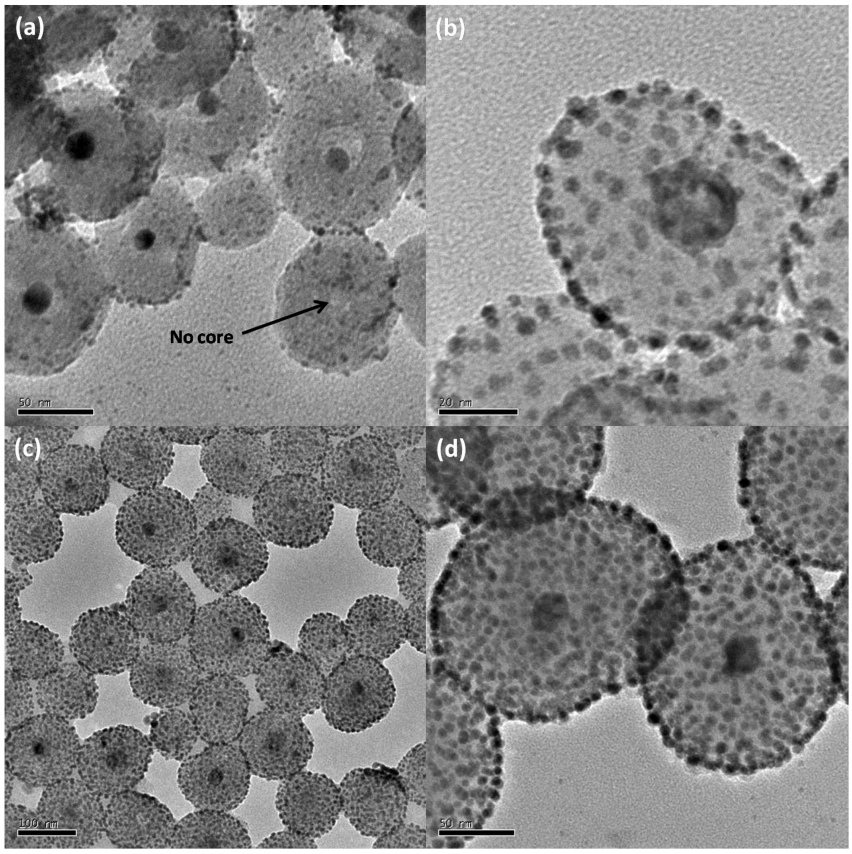

Figure 7.5: TEM images of (a) silver-silica-gold seed; fully grown silver-silica-gold sandwich nanoparticles having (b) 25 nm, (c) 40 nm, and (d) 60 nm silica shell thickness. Scale bar is 50 nm (a) and (d), 20 nm for (b) and 100 nm image (c) image. Arrow in Figure (a) points to the completely oxidized core.

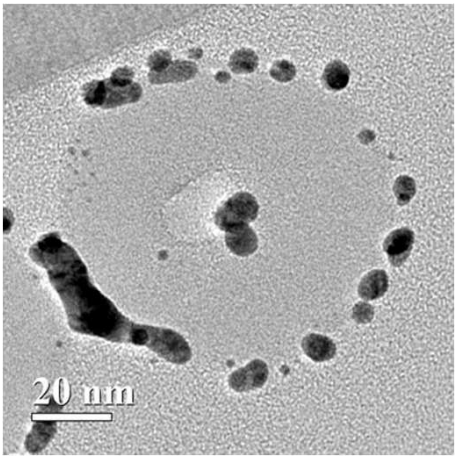

Figure 7.6: Cross-sectional TEM image of silver-silica-gold sandwich nanostructure.

the silver core and 8-10 nm sized gold islands respectively. Here, the silica shell is 40 nm in size. Increase in surface coverage of silica shell hinders light penetration through the silica layer resulting into decrease in intensity of silver core. The rise in gold peak intensity is attributable to the larger size and higher density of gold islands on silica surface. Further, sandwich nanoparticles with varying silica shell thickness were also prepared whose extinction spectra is shown in Figure 7.3b.

Figure 7.5 presents the TEM image of silver-silica-gold seed particle and fully grown silver-silica-gold sandwich nanoparticles with varying silica shell thickness. As discussed above, we see that few of the silver core have completely vanished (arrow in Figure 7.5a) while others have reduced in size due to their oxidation by gold ions. However, it must be mentioned here that most of the sandwich particles had core intact in them. Cross sectional TEM (Figure 7.6) shows the silver core and the gold islands adhered to the silica surface suggesting that gold is not embedded in the silica matrix but attached on the surface.

In further experiments, we also varied the size and density of gold islands. It is seen from extinction spectra shown in Figure 7.7 that with increasing size and density of gold island SN1 $<$ SN2 $<$ SN3, the SPR position changes from 524 nm to 530 nm to 541 nm. The TEM image shown in Figure 7.8 show images of sandwich nanoparticles with different size and density of islands.

Field emission scanning electron microscopy (FESEM) image of sandwich nanoparticles having 40 nm silver core, 40 nm silica layer thickness and 8 nm gold island shown in Figure 7.9 clearly indicates the monodispersity of sandwich nanoparticles. The XRD pattern (Figure 7.10) shows four characteristic peaks of face centered cubic structure of metals, marked by indices (111), (200), (220) and (311) [37]. The peaks of gold and silver are too broad and indistinguishable. A broad hump in the 2θ region of 22-25° is the signature of silica in sandwich nanoparticle [37].

To demonstrate the efficacy of sandwich nanoparticles as SERS substrate, we

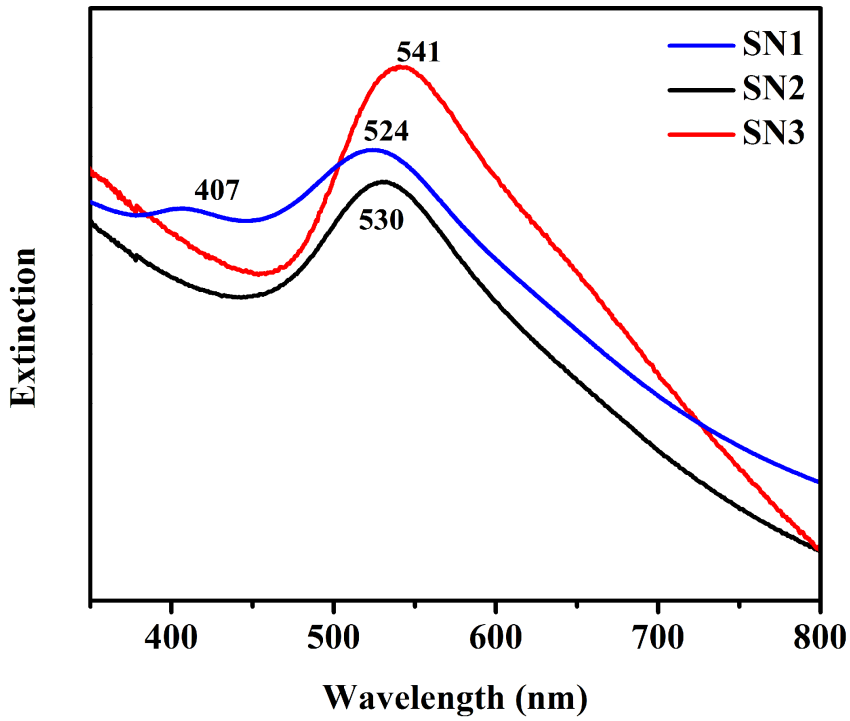

Figure 7.7: Extinction spectra of sandwich nanoparticles with different size and densities of gold islands: SN1(blue curve),SN2 (black curve) and SN3 (red curve).

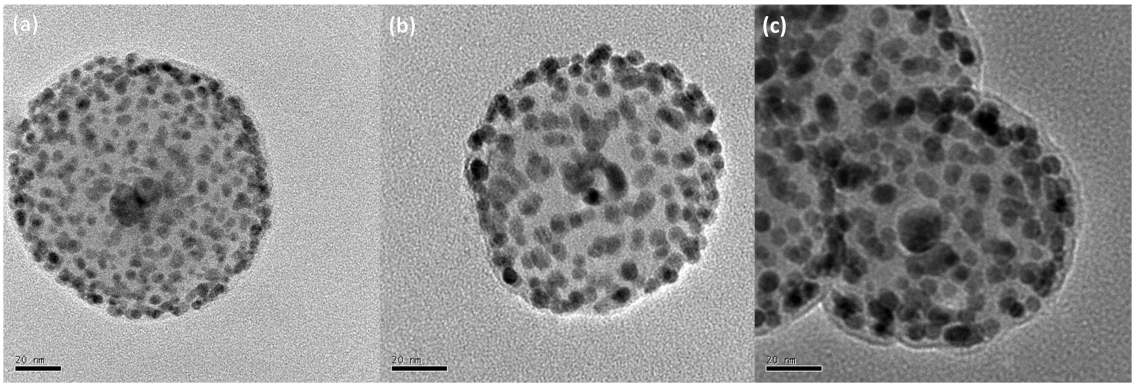

Figure 7.8: TEM image of sandwich nanoparticles with different size and densities of gold islands. (a) SN1, (b) SN2, (c) SN3. Scale bar is 20 nm for all images.

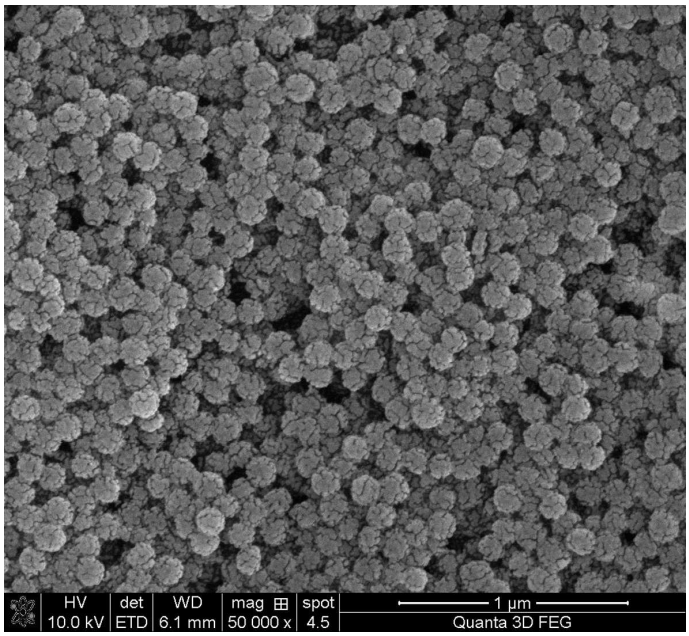

Figure 7.9: FESEM picture of silver-silica-gold sandwich nanoparticles.

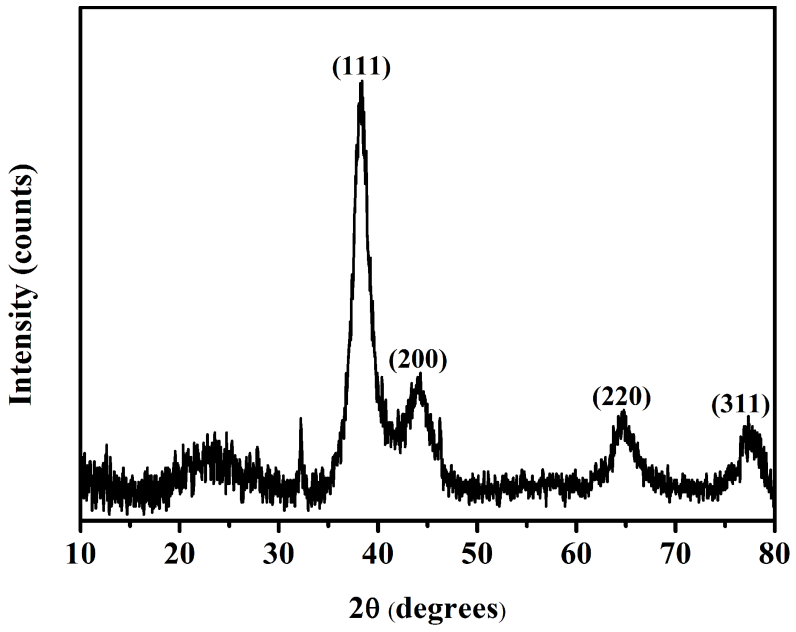

Figure 7.10: XRD pattern of silver-silica-gold sandwich nanoparticles.

recorded the SERS spectra of thiophenol at various concentrations. Thiophenol and nanoparticles were mixed in equal volume and dried on a cleaned glass slide before recording the spectra. SERS spectra of different concentrations of thiophenol adsorbed on sandwich nanoparticles is shown in Figure 7.11. The signature peaks of thiophenol at 996, 1021, 1074 and 1571 cm^{-1} corresponding to the out-of-plane ring deformation, in-plane ring deformation and C-C symmetric stretch, C-C asymmetric stretch and C-S stretch, and C-C symmetric bending mode are observed [38, 39]. The enhancement factor G was calculated using the following formula [8],

$$G = \frac{C_R}{C_S} \times \frac{I_S}{I_R} \tag{7.1}$$

where, I_R and I_S are normal Raman and SERS intensities of the peak at 996 cm^{-1} respectively. C_R and C_S represent the respective concentrations of thiophenol in the Raman and SERS measurements. The analytical enhancement factor was found to be 10^6 for sandwich nanoparticle having 40 nm silica shell thickness. SERS enhancement factor was found to decrease if the silica thickness was 60 nm or 25 nm (Figure 7.12a), or when the densities of gold islands were too high which would not allow light to penetrate to or emerge from sandwich nanoparticles thus reducing the enhancement factor (Figure 7.12b).

To illustrate that core is playing a vital role in enhancing the Raman signal, silica core gold island shell nanoparticles with no silver core was synthesized. The nanoparticle was characterized by UV-visible spectroscopy (Figure 7.3a, green curve) and TEM (Figure 7.13). Figure 7.14a and 7.14b respectively show the SERS spectra of 10^{-5} M and 10^{-7} M thiophenol on $Ag@SiO_2@Au$ and $SiO_2@Au$ nanostructures. It was found that enhancement factor of $Ag@SiO_2@Au$ was six times higher than that of $SiO_2@Au$ nanoparticle (Figure 7.14a). The detection limit which is the concentration detected by SERS is two orders of magnitude higher in $Ag@SiO_2@Au$ than in $SiO_2@Au$ (Figure 7.14b). To explain the greater enhancement in $Ag@SiO_2@Au$

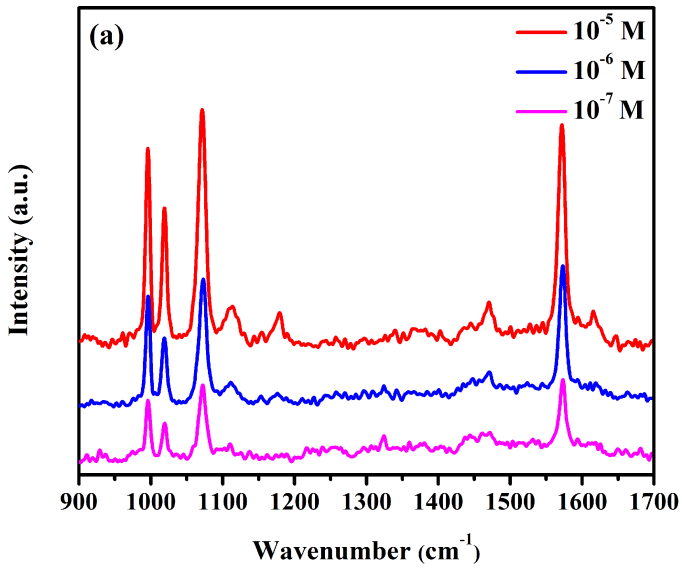

Figure 7.11: SERS spectra of thiophenol at different concentrations on Ag@SiO_2@Au sandwich nanoparticles.

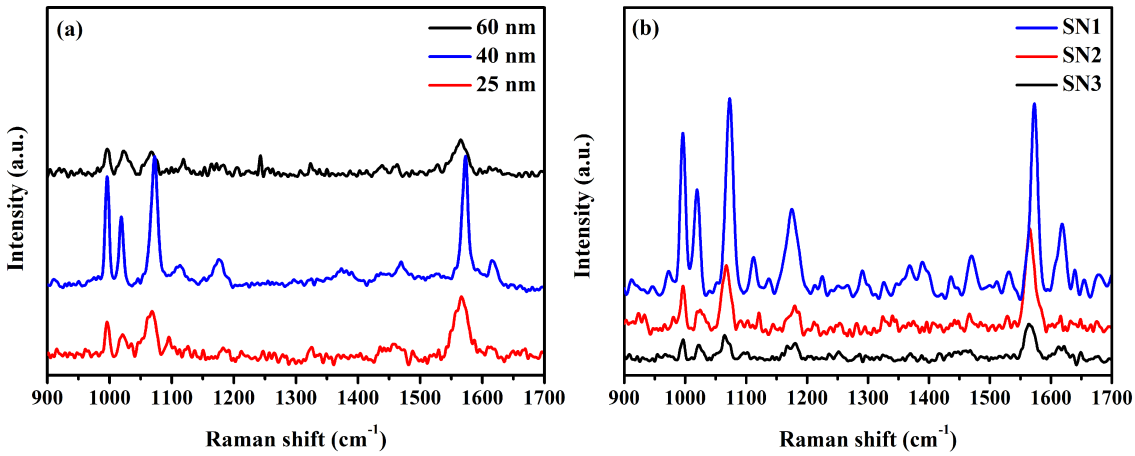

Figure 7.12: (a) SERS spectra of thiophenol at 10^{-4} M on sandwich nanoparticles having 40 nm (blue curve) and 60 nm (black curve) silica shell and 1 mM on sandwich nanoparticles having 25 nm silica shell (red curve), (b) SERS spectra of 1 mM thiophenol on SN1, SN2 and SN3 sandwich nanoparticles.

sandwich nanostructures, we propose that the light incident (i1) on the sandwich structure in the crevices of gold islands is partially reflected (r1) and partially transmitted (t1) through the silica layer wherein it is reflected (r2) by the silver core (see Figure 7.15). The transmitted light can undergo multiple reflections before emerging from the gap between the islands. The regions of constructive interference of incident light (i2) and refracted light (r3) (satisfying Bragg's condition) will be the zones of high field intensity. Analyte if present in such regions will experience enhanced electric field, resulting into high Raman intensity. Further more, plasmon coupling of the gold islands on the silica surface will also generate regions of high field intensity further contributing to enhanced SERS signal. Similar observation has been made by Basca *et al.* on Raman signal of C_{60} monolayer deposited on silica-on-aluminium substrate due to interference of light [40].

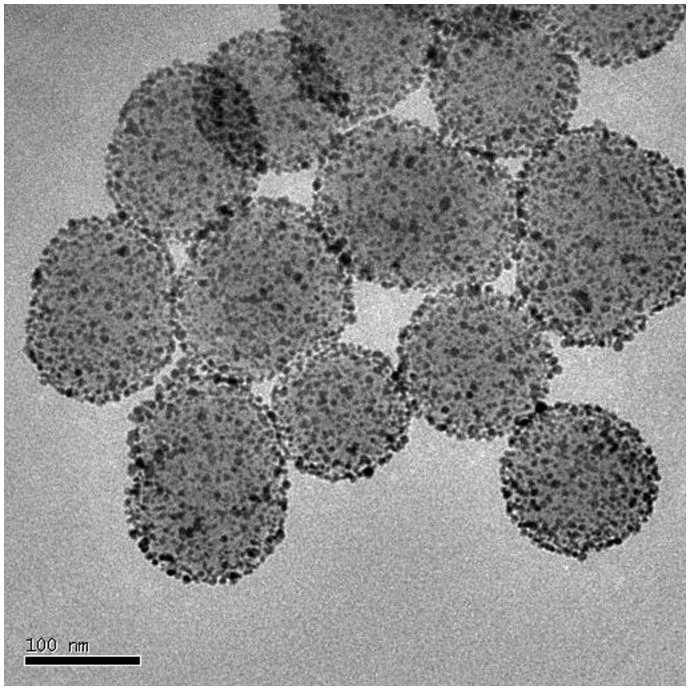

Figure 7.13: TEM image of silica core gold island nanoparticles. Scale bar is 100 nm.

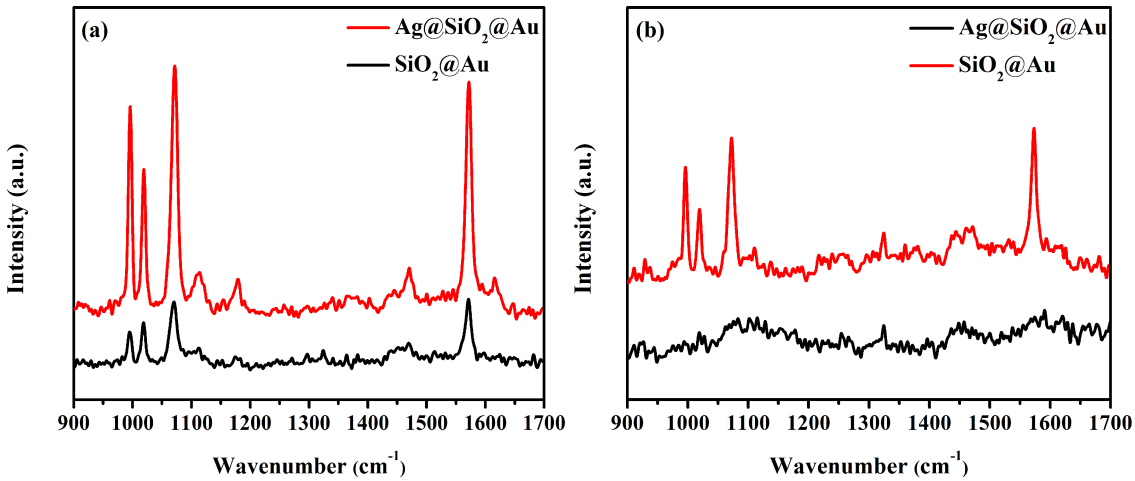

Figure 7.14: (a) SERS spectra of 10^{-5} M thiophenol on Ag@SiO_2@Au and SiO_2@Au nanostructures. (b) SERS spectra of 10^{-7} M thiophenol on Ag@SiO_2@Au and SiO_2@Au nanostructures.

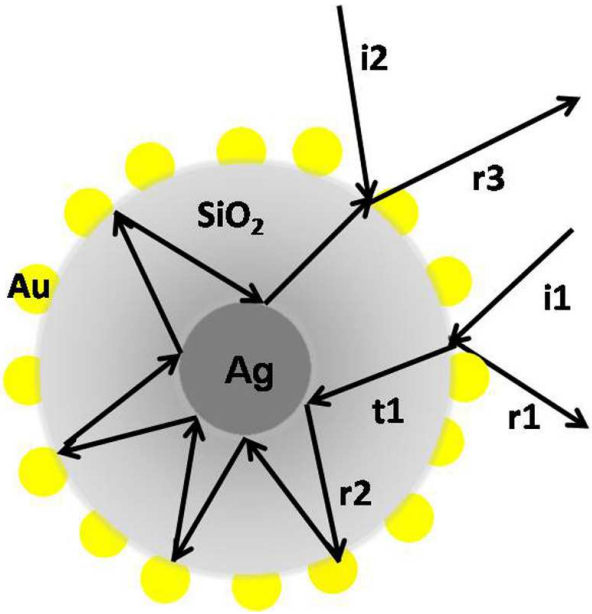

Figure 7.15: Schematic of path of light through silver-silica-gold sandwich nanoparticles showing multiple reflections within the nanostructure.

7.4 Conclusions

In this work, we have demonstrated a facile method to synthesize an effective SERS substrate silver-silica-gold sandwich nanoparticle. Presence of two metals results in two plasmon dipole modes at 407 nm and 524 nm corresponding to silver core and gold island respectively. We have optimised the silica shell thickness and density of gold islands to achieve maximum SERS enhancement in sandwich nanostructures. The optimal silica shell thickness was 40 nm for which an enhancement factor of 10^6 was observed. We believe that constructive interference of the incident beam and multiple reflections from the silver core generates regions of high electric field. This was also proved by a control experiment using silica core-gold island shell nanostructure with no silver core which showed a lower enhancement factor (by sixth time) and reduced detection limit. Additionally, plasmon coupling between the gold islands could also lead to enhanced Raman signal. Further, sandwich nanostructure could be prospective SERS substrate for bio-detection due to the presence of bio-compatible gold islands on silica surface.

Bibliography

[1] P. K. Jain, K. S. Lee, I. H. El-Sayed, and M. A. El-Sayed, *Calculated absorption and scattering properties of gold nanoparticles of different size, shape, and composition: applications in biological imaging and biomedicine*, The Journal of Physical Chemistry B **110**, 7238 (2006).

[2] Y.-Y. Yu, S.-S. Chang, C.-L. Lee, and C. C. Wang, *Gold nanorods: electrochemical synthesis and optical properties*, The Journal of Physical Chemistry B **101**, 6661 (1997).

[3] R. Jin *et al.*, *Controlling anisotropic nanoparticle growth through plasmon excitation*, Nature **425**, 487 (2003).

[4] U. Kreibig and L. Genzel, *Optical absorption of small metallic particles*, Surface Science **156**, 678 (1985).

[5] M. J. Mulvihill, X. Y. Ling, J. Henzie, and P. Yang, *Anisotropic etching of silver nanoparticles for plasmonic structures capable of single-particle SERS*, Journal of the American Chemical Society **132**, 268 (2009).

[6] Y. Sun and Y. Xia, *Shape-controlled synthesis of gold and silver nanoparticles*, Science **298**, 2176 (2002).

[7] P. N. Njoki *et al.*, *Layer-by-Layer Processing and Optical Properties of Core/Alloy Nanostructures*, Journal of the American Chemical Society **133**, 5224 (2011).

[8] L. Rivas, S. Sanchez-Cortes, J. Garcia-Ramos, and G. Morcillo, *Mixed silver/gold colloids: a study of their formation, morphology, and surface-enhanced Raman activity*, Langmuir **16**, 9722 (2000).

[9] P. Stoller, V. Jacobsen, and V. Sandoghdar, *Measurement of the complex dielectric constant of a single gold nanoparticle*, Optics letters **31**, 2474 (2006).

[10] S. Underwood and P. Mulvaney, *Effect of the solution refractive index on the color of gold colloids*, Langmuir **10**, 3427 (1994).

[11] M. P. Mallin and C. J. Murphy, *Solution-phase synthesis of sub-10 nm Au-Ag alloy nanoparticles*, Nano Letters **2**, 1235 (2002).

[12] N. Toshima, M. Harada, Y. Yamazaki, and K. Asakura, *Catalytic activity and*

structural analysis of polymer-protected gold-palladium bimetallic clusters prepared by the simultaneous reduction of hydrogen tetrachloroaurate and palladium dichloride, The Journal of Physical Chemistry **96**, 9927 (1992).

[13] R. Morriss and L. Collins, *Optical properties of multilayer colloids*, The Journal of Chemical Physics **41**, 3357 (1964).

[14] H. Wang and N. J. Halas, *Mesoscopic Au "meatball" particles*, Advanced Materials **20**, 820 (2008).

[15] C. E. Talley *et al.*, *Surface-enhanced Raman scattering from individual Au nanoparticles and nanoparticle dimer substrates*, Nano Letters **5**, 1569 (2005).

[16] J. Jackson *et al.*, *Controlling the surface enhanced Raman effect via the nanoshell geometry*, Applied Physics Letters **82**, 257 (2003).

[17] J. B. Jackson and N. J. Halas, *Surface-enhanced Raman scattering on tunable plasmonic nanoparticle substrates*, Proceedings of the National Academy of Sciences **101**, 17930 (2004).

[18] R. Bardhan *et al.*, *Nanosphere-in-a-nanoshell: a simple nanomatryushka*, The Journal of Physical Chemistry C **114**, 7378 (2009).

[19] M. Schierhorn and L. M. Liz-Marzan, *Synthesis of bimetallic colloids with tailored intermetallic separation*, Nano Letters **2**, 13 (2002).

[20] K. Kim, H. S. Kim, and H. K. Park, *Facile method to prepare surface-enhanced-Raman-scattering-active Ag nanostructures on silica spheres*, Langmuir **22**, 8083 (2006).

[21] A. Campion and P. Kambhampati, *Surface-enhanced Raman scattering*, Chem. Soc. Rev. **27**, 241 (1998).

[22] L. Tong, T. Zhu, and Z. Liu, *Approaching the electromagnetic mechanism of surface-enhanced Raman scattering: from self-assembled arrays to individual gold nanoparticles*, Chemical Society Reviews **40**, 1296 (2011).

[23] A. Campion, J. Ivanecky III, C. Child, and M. Foster, *On the mechanism of chemical enhancement in surface-enhanced Raman scattering*, Journal of the American Chemical Society **117**, 11807 (1995).

[24] R. Aroca, in *Surface-enhanced vibrational spectroscopy* (John Wiley & Sons, , 2006).

[25] L. C. Shoute *et al.*, *Optical interference effects in the design of substrates for surface-enhanced Raman spectroscopy*, Applied spectroscopy **63**, 133 (2009).

[26] L. C. Shoute, *Multilayer Substrate-Mediated Tuning Resonance of Plasmon and SERS EF of Nanostructured Silver*, ChemPhysChem **11**, 2539 (2010).

[27] C. Li *et al.*, *One-pot synthesis of $Ag@SiO_2@Ag$ sandwich nanostructures*, Nanotechnology **21**, 245602 (2010).

[28] C. Graf and A. van Blaaderen, *Metallodielectric colloidal core-shell particles for photonic applications*, Langmuir **18**, 524 (2002).

[29] D. G. Duff, A. Baiker, and P. P. Edwards, *A new hydrosol of gold clusters. 1. Formation and particle size variation*, Langmuir **9**, 2301 (1993).

[30] G. P. Kumar and C. Narayana, *Adapting a fluorescence microscope to perform surface enhanced*, Current science **93**, 778 (2007).

[31] W. Stöber, A. Fink, and E. Bohn, *Controlled growth of monodisperse silica spheres in the micron size range*, Journal of colloid and interface science **26**, 62 (1968).

[32] S. Oldenburg, R. Averitt, S. Westcott, and N. Halas, *Nanoengineering of optical resonances*, Chemical Physics Letters **288**, 243 (1998).

[33] S. Oldenburg, G. Hale, J. Jackson, and N. Halas, *Light scattering from dipole and quadrupole nanoshell antennas*, Applied Physics Letters **75**, 1063 (1999).

[34] S. J. Oldenburg, J. B. Jackson, S. L. Westcott, and N. Halas, *Infrared extinction properties of gold nanoshells*, Applied Physics Letters **75**, 2897 (1999).

[35] S. J. Oldenburg, S. L. Westcott, R. D. Averitt, and N. J. Halas, *Surface enhanced Raman scattering in the near infrared using metal nanoshell substrates*, The Journal of chemical physics **111**, 4729 (1999).

[36] P. Theissen, *Goldhydrosole abgestufter Teilchengrößen ohne Zuführung von Keimen*, Kolloidchemische Beihefte **29**, 122 (1929).

[37] V. Pol, A. Gedanken, and J. Calderon-Moreno, *Deposition of gold nanoparticles on silica spheres: a sonochemical approach*, Chemistry of materials **15**, 1111 (2003).

[38] M. A. Bryant, S. L. Joa, and J. E. Pemberton, *Raman scattering from monolayer films of thiophenol and 4-mercaptopyridine at platinum surfaces*, Langmuir **8**, 753 (1992).

[39] S. Li, D. Wu, X. Xu, and R. Gu, *Theoretical and experimental studies on the adsorption behavior of thiophenol on gold nanoparticles*, Journal of Raman Spectroscopy **38**, 1436 (2007).

[40] W. Bacsa and J. Lannin, *Bilayer interference enhanced Raman spectroscopy*, Applied physics letters **61**, 19 (1992).

Summary and Future Prospects

The relevance of Raman spectroscopy in deducing structural transformation as a consequence of external stimuli such as temperature, pressure and gas adsorption has been elucidated in first part of thesis on metal organic frameworks and zeolitic imidazolate frameworks.

Metal organic frameworks are soft porous materials known for their fascinating structures which result in interesting properties such as gas adsorption, catalysis, luminescent and magnetism. Very often, one can see the consequence but does not understand the phenonema at the fundamental level and hence cannot make the approriate changes which can further improve the desired property. Although X-ray diffraction is inevitable for structure deduction, it is incapable to pin-point the positions of lighter atoms such as hydrogen atoms whose slight change in position can alter the properties. Probing such minute changes mandates the use of a local probe.

Raman spectroscopy is a local probe and its role amplifies when other techniques fail to capture such local transformations which are responsible for change in macro properties of the material. In the first part on metal organic frameworks, Raman spectroscopy has been employed to investigate the structural transitions which could not be understood with the help of X-ray diffraction or other techniques. Raman spectroscopy is most often used only as a characteristic tool. However, the information obtained on careful analysis of the Raman spectrum is unprecedented,

which has resulted in the extensive use of the technique. In many of the recent literature on MOFs, the technique is being employed to prove the gas adsorption as their modes appear when they are encapsulated in a small pore or when they interact with the framework. As a consequence of this, the bond strength of host as well as guest modes changes which is reflected as softening or hardening of the modes. It must be emphasized here that Raman spectroscopy precisely captures such alterations or modifications in the structure.

The second part of the thesis is focussed on the phenomenon of surface enhanced Raman spectroscopy, more specifically its distance dependence and synthesis of nanostructures for SERS applications. The advantage of SERS lies in its ability to probe molecules at very low concentrations. Although, the technique has been employed for diverse applications, it is limited by distance. SERS intensity decays exponentially with distance and hence it can not effectively probe larger molecules or polymers such as proteins, or an analyte sitting at a farther distance. Our experiments suggest that SERS intensity decay with distance is a function of nanoparticle size. The decay is faster and hence intense electric field is experienced only in a short range from smaller nanoparticles while distant SERS (upto 5 nm from nanoparticle surface) could be obtained using larger nanoparticles of size 90 nm.

Design and fabrication of cost effective SERS substrates for various applications is desired. In this direction, we have synthesized sandwich nanoarchitecture showing an enhancement factor of the order of 10^6. Various nanostructures have been reported in literature, yet their analytical applications are yet to be carried out. One of the major hurdle is the reproducibility of the SERS spectrum which must be addressed in future.

Hence, I conclude this thesis on an affirmative note that Raman spectroscopy has huge potential in investigating materials properties. The progress in application of Raman and SERS in past few years are very promising yet a comprehensive

understanding of the mechanism of SERS is necessary to make further advances in this field.

List of Publications

1. *New Nano Architecture for SERS Applications*

   Gayatri Kumari and Chandrabhas Narayana

   Journal of Physical Chemistry Letters 3, 1130-1135 (2012). **(Chapter 7)**

2. *Unusual room temperature CO2 uptake in a fluorofunctionalized MOF: insight from Raman spectroscopy and theoretical studies*

   Prakash Kanoo, Sandeep K. Reddy, **Gayatri Kumari**, Ritesh Haldar, Chandrabhas Narayana, Sundaram Balasubramanian, Tapas K. Maji

   Chemical Communications 48, 8487-8489 (2012). **(Chapter 4)**

3. *Temperature Induced Structural Transformations and Gas Adsorption in ZIF-8: A Raman Study*

   Gayatri Kumari, Kolleboyina Jayaramulu, Tapas K. Maji and Chandrabhas Narayana

   Journal of Physical Chemistry A 117, 11006-11012 (2013). **(Chapter 3)**

4. *Understanding guest and pressure induced porosity through structural transition in flexible interpenetrated MOF by Raman Spectroscopy*

   Gayatri Kumari, N. R. Patil, Venkata S. Bhadram, Ritesh Haldar, Tapas K. Maji and Chandrabhas Narayana

   Journal of Raman Spectroscopy (2015), accepted. **(Chapter 5)**

5. *How far can we probe by SERS?*

Gayatri Kumari, Jyothirmayee Kandula and Chandrabhas Narayana
Journal of Physical Chemistry c (2015), accepted. **(Chapter 6)**

Miscellaneous publications

1. *Honeycomb Porous Framework of Zinc(II): Effective Host for Palladium Nanoparticles for Efficient Three-Component (A3) Coupling and Selective Gas Storage*
   Kolleboyina Jayaramulu, Kasibhatta K. R. Datta, Mothika V. Suresh, **Gayatri Kumari**, Ranjan Datta, Chandrabhas Narayana, Muthusamy Eswaramoorthy and Tapas K. Maji1 , Jyothirmayee Kandula and Chandrabhas Narayana
   ChemPlusChem 77, 743-747 (2012)

2. *Conformational Change in a Urea Catalyst Induced by Sodium Cation and its Effect on Enantioselectivity of a Friedel-Crafts Reaction*
   Arjun K. Chittoory, **Gayatri Kumari**, Sudip Mohapatra, Partha P. Kundu, Tapas K. Maji, Chandrabhas Narayana and Sridhar Rajaram
   Tetrahedron 70, 3459-3465 (2014)

3. *Raman, IR and DFT studies of mechanism of Sodium binding to urea catalyst*
   Partha P. Kundu, **Gayatri Kumari**, Arjun K. Chittoory, Sridhar Rajaram and Chandrabhas Narayana
   Journal of Molecular Structure Under Revision

4. *Morphology dependent enhancement of SERS detection in a Ag/GaN nanowall network*
   S. Sharvani, **Gayatri Kumari**, K. Upadhayaya, Chandrabhas Narayana and S.M. Shivaprasad
   Submitted

5. *Raman spectroscopic study of structural transition and gas adsorption in ZIF-4 and ZIF-7*

Gayatri Kumari, Ashlin M. Raj, Pinky A. Daniel and Chandrabhas Narayana

Manuscript Under preparation